

Final Progress Report

Prepared for:
U.S. Army Research Office
Research Triangle Park, NC

A Physical Multidimensional Acoustics Convection Upstream Resolution Algorithm for the 3-D Euler and Navier-Stokes Equations

Joe Iannelli

Project No. DAAH04-96-1-0095

MAES-2000-4-1.0-CFDL

April 2000

Tel.: (423) 974 - 6009

Fax.: (423) 974 - 7663

e-mail: jiannell@utk.edu

**The University of Tennessee
Mechanical & Aerospace Engineering
and Engineering Science Department
315 Perkins Hall
Knoxville, TN 37996-2030, USA**



REPORT DOCUMENTATION PAGE

Form Approved
OMB NO. 0704-0188

Public reporting burden for this collection of information is estimated to average 1 hour per response, including the time for reviewing instructions, searching existing data sources, gathering and maintaining the data needed, and completing and reviewing the collection of information. Send comment regarding this burden estimate or any other aspect of this collection of information, including suggestions for reducing this burden, to Washington Headquarters Services, Directorate for Information Operations and Reports, 1215 Jefferson Davis Highway, Suite 1204, Arlington, VA 22202-4302, and to the Office of Management and Budget, Paperwork Reduction Project (0704-0188), Washington, DC 20503.

1. AGENCY USE ONLY (Leave blank)	2. REPORT DATE	3. REPORT TYPE AND DATES COVERED
	03-30-2000	Final, 7-1-96, 6-30-1999
4. TITLE AND SUBTITLE A Physical Multidimensional Acoustics-Convection Upstream Resolution Algorithm for the 3-D Euler and Navier-Stokes Equations		5. FUNDING NUMBERS DAAH04-96-1-0095
6. AUTHOR(S) Joe Iannelli		
7. PERFORMING ORGANIZATION NAMES(S) AND ADDRESS(ES) The University of Tennessee - Office of Research 404 Andy Holt Tower Knoxville, TN 37996 - 0140		8. PERFORMING ORGANIZATION REPORT NUMBER MAES-2000-4-1.0-CFDL
9. SPONSORING / MONITORING AGENCY NAME(S) AND ADDRESS(ES) U.S. Army Research Office P.O. Box 12211 Research Triangle Park, NC 27709-2211		10. SPONSORING / MONITORING AGENCY REPORT NUMBER ARO 35055.2-EG
11. SUPPLEMENTARY NOTES The views, opinions and/or findings contained in this report are those of the author(s) and should not be construed as an official Department of the Army position, policy or decision, unless so designated by other documentation.		
12a. DISTRIBUTION / AVAILABILITY STATEMENT Approved for public release; distribution unlimited.		12 b. DISTRIBUTION CODE
13. ABSTRACT (Maximum 200 words) This project has synthesized an innovative implicit finite element CFD algorithm to advance the computational simulation of inviscid and viscous compressible flows. This report details for the 3-D Euler and Navier-Stokes equations an intrinsically infinite directional upstream formulation that rests on the mathematics and physics of multi-dimensional acoustics and convection. Based upon characteristic velocities, this formulation introduces the upstream bias directly at the differential equation level, before the spatial discretization, within a characteristics-bias governing system. A conventional centered discretization of this system on given grids directly yields an optimal discretely conservative and multi-dimensional upstream approximation for the Euler and Navier-Stokes equations. The induced dissipation is non-linearly minimized by way of a solution-dependent controller. Through a decomposition of the Euler flux divergence into multidimensional acoustics and convection acoustics components, the formulation induces consistent upstream bias along all directions of spatial wave propagation, with anisotropic variable-strength upstreaming that correlates with the spatial distribution of characteristic velocities.		
14. SUBJECT TERMS CFD, Euler, Navier-Stokes, Upwind, Acoustics, Convection, Finite Elements, Artificial Diffusion, Implicit, Runge-Kutta		15. NUMBER OF PAGES 103
16. PRICE CODE		
17. SECURITY CLASSIFICATION OR REPORT UNCLASSIFIED	18. SECURITY CLASSIFICATION OF THIS PAGE UNCLASSIFIED	19. SECURITY CLASSIFICATION OF ABSTRACT UNCLASSIFIED
		20. LIMITATION OF ABSTRACT UL

Overview

This project has received support from ARO to advance the state of the art in the CFD solution of the Euler and Navier Stokes equations, with the specific objective of increasing accuracy in the computational prediction of compressible flows of Army interest. To reach this objective, this project has developed an innovative implicit finite element CFD algorithm that relies on multi-dimensional characteristics theory. By firmly resting on the physics and mathematics and acoustics and convection, the wave propagation mechanisms within fluid flows, the algorithm is designed to generate accurate solutions and minimize induced artificial diffusion.

During this project, a 40-page paper detailing project results and entitled: "A CFD Euler Solver from a Physical Acoustics-Convection Flux Jacobian Decomposition" has been published in the International Journal for Numerical Methods in Fluids. This paper is included as Appendix G of this report. Furthermore, the principal investigator has signed a publishing contract with John Wiley & Sons to write an advanced CFD book that will feature the results obtained in this project.

Contents

1	Introduction	3
2	Governing Equations	5
2.1	Navier-Stokes System	5
2.2	Constitutive Relations	6
2.3	Equations of State and Speed of Sound	6
3	Non-Discrete Characteristics-Bias Approximation	7
3.1	Flux Jacobian Decomposition and Upstream-Bias Integral Average	9
3.2	Characteristics-Bias Flux	9
3.2.1	van Leer's Formulation and Flux Vector Splitting	10
3.2.2	Roe's Formulation and Flux Difference Splitting	11
4	Characteristics Analysis	12
4.1	Non-linear Wave-Like Solutions	12
4.2	Characteristic Velocity Components	12
4.3	Polar Variation of Characteristic Speeds	14
4.4	Regions of Supersonic and Subsonic Wave Propagation	15
4.5	Physical Multi-dimensional Upstream Bias	16
5	Acoustics-Convection Flux Jacobian Components	17
5.1	Convection and Pressure-Gradient Components	17
5.2	Acoustic Equations	19
5.3	Acoustic Components	21
5.3.1	Streamline and Crossflow Components	22
5.3.2	Absolute Acoustics Matrices	24
6	Acoustics-Convection Flux Divergence Decomposition	25
6.1	Equivalent Decompositions	26
6.2	Multidimensional Characteristics Euler Flux	27
7	Infinite Directional Upstream Bias	28
7.1	Conditions on Upstream-Bias Functions and Eigenvalues	29
7.2	Streamline Eigenvalue λ_4	29
7.3	Streamline Eigenvalue λ_1	30
7.4	Upstream-Bias Functions a , a^{N1} , a^{N2} , α , δ and α^N	30
7.5	Streamline Upstream-Bias Eigenvalues	32
7.6	Polar Variation of Upstream-Bias	33
8	Finite Element Weak Statement	35
8.1	Elimination of Spurious Upstream Boundary Dissipation	36
8.2	Galerkin Finite Element Equations	36
8.3	Discrete Conservation	38
9	Discrete Upstream-Bias Controller ψ^h	39
10	Implicit Runge Kutta Time Integration	43
11	Concluding Remarks	44

A Solutions in Non-linear Wave-Like Form	47
B Wave-Propagation and Characteristic Surfaces	49
B.1 Wave-Propagation Surfaces	49
B.2 Characteristic Surfaces	50
B.3 Characteristic Cones	51
C Acoustics Matrices	55
D Upstream-Bias Stability Condition	56
E Crossflow Upstream Function α^N	57
F Discrete Conservation	58

A Physical Multi-Dimensional Acoustics-Convection Upstream Resolution Algorithm for the 3-D Euler and Navier-Stokes Equations

JOE IANNELLI*

Department of Mechanical & Aerospace Engineering and Engineering Science
The University of Tennessee, 315 Perkins Hall, Knoxville, TN 37996-2030, U.S.A.

SUMMARY

This report details for the 3-D Euler and Navier-Stokes equations an intrinsically infinite directional upstream formulation that rests on the mathematics and physics of multi-dimensional acoustics and convection. Based upon characteristic velocities, this formulation introduces the upstream bias directly at the differential equation level, before the spatial discretization, within a characteristics-bias governing system. A conventional centered discretization of this system on given grids directly yields an optimal discretely conservative and multi-dimensional upstream approximation for the Euler equations. Through a decomposition of the Euler flux divergence into multidimensional acoustics and convection acoustics components, the formulation induces consistent upstream bias along all directions of spatial wave propagation, with anisotropic variable-strength upstreaming that correlates with the spatial distribution of characteristic velocities. With the objective of minimizing induced artificial diffusion, the formulation non-linearly induces upstream-bias essentially locally in regions of solution discontinuities, whereas it decreases the upstream-bias in regions of solution smoothness. The discrete equations originate from a finite element discretization of the characteristic-bias system and are integrated in time within a compact block tri-diagonal matrix statement by way of an implicit non-linearly stable Runge-Kutta algorithm for stiff systems.

KEY WORDS: CFD; characteristics; multi-dimensional upwind; implicit; finite elements;

1 Introduction

The CFD community is still eagerly pursuing a multi-dimensional Euler solver for computing realistic flows on arbitrary grids. Many finite element, difference and volume algorithms have remained somewhat independent from the physics of acoustics and convection, the wave propagation mechanisms within gas dynamic flows. The dissipation mechanisms, or upwind schemes, within these algorithms have been developed at the discrete level, in connection with a specific grid or pattern of computational cells.

Several finite element solvers have either utilized modifications of the test space or introduced Taylor's series based dissipation terms, e.g. TWS,¹ to generate stable algorithms. The mathematical developments in these fundamental contributions have remained independent of characteristics theory. Upwind finite element methods for scalar equations have also been developed,² including the Streamline Upwind Petrov-Galerkin (SUPG) formulation³⁻⁷ for also known as the Streamline Diffusion (SD) method. Extensions to systems are recognized to remain heuristic,⁸ the induced upwinding is not necessarily in the streamline direction, and additional "shock capturing" terms are needed for computing essentially non-oscillatory shocked flows.

Intense research is also focused on multi-dimensional finite-volume upwind schemes that induce upwinding along a few significant directions. An early effort⁹ generated a grid-independent upwind scheme based on directional upwinding along possible shock wave directions. This approach later

* Associate Professor, jiannell@utk.edu. Joe Iannelli, Dept. of Mechanical & Aerospace Engineering and Engineering Science, The University of Tennessee, 315 Perkins Hall, Knoxville, TN 37996-2030, U.S.A.

enjoyed addition of local Riemann solutions¹⁰ along several upwind directions including the flow velocity, speed gradient and pressure gradient directions. An alternative second order rotated upwind scheme used flux-difference splitting along two orthogonal directions¹¹ determined on the basis of the pressure gradient. Other approaches involved approximate multi-dimensional Riemann solvers and local wave decompositions, with wave modeling.¹²⁻¹⁵ In these formulations, some wave directions and strengths must still be fixed a-priori to generate a viable CFD algorithm.

Difficulties exist in these methods in assessing the magnitude of the induced multi-dimensional upwind diffusion. It is also difficult to determine whether consistent upwinding exists not only over the selected directions, but along all flow-field wave-propagation directions. Additional data filtering or upwind-direction freezing may also be required for convergence and essential monotonicity. More fundamentally, current multi-dimensional upwind schemes are recognized¹⁶ to rest upon much less theoretical support than their one-dimensional counterparts.

This report expounds the multi-dimensional formulation of the one-dimensional acoustics-convection upstream resolution algorithm.¹⁷ Developed for the 2-D and 3-D Euler and Navier-Stokes equations with general equilibrium equations of state, this formulation develops the upstream-bias approximation directly at the differential equation level, before any discretization, and it encompasses, unifies and generalizes upwind algorithms, including Flux Vector Splitting and Flux Difference Splitting developments. The formulation results in a "companion" characteristics-bias system that is associated with the Navier-Stokes equations and rests on a decomposition of the multidimensional Euler jacobian into acoustics and convection components. Heed in particular that no single decomposition of the Euler flux components themselves can contain separate components that respectively correspond to the physics of multi-dimensional acoustics and convection.

This formulation induces the upstream bias along all flow-field directions of wave propagation and enjoys a consistent theoretical support that rests upon the mathematics and physics of multi-dimensional characteristic wave propagation. The formulation, moreover, reduces to a consistent upstream approximation of the acoustics equations, for vanishing Mach number, which addresses the challenging problem of calculating low-Mach-number flows. The formulation, furthermore, supplies a stable and intrinsically infinite directional upstream-bias that induces minimal diffusion, for crisp oblique-shock capturing and accurate resolution of vortical structures, naturally incorporates a finite element discretization with implicit time integration because it is straightforward to determine the required jacobian matrices.

A traditional centered discretization on arbitrary grids of the characteristics-bias system automatically and directly generates a consistent, discretely conservative and genuinely multi-dimensional upstream-bias approximation of the Euler and Navier-Stokes equations. The associated discrete multi-directional upstream-bias remains independent of the direction of the coordinate axes as well as orientation of each computational-cell side, which obviates the need for rotated stencils. This approximation requires data only from the computational cells shared by each grid node and also reduces to a consistent upstream approximation of the acoustics equations, for vanishing Mach number, which addresses the challenging problem of calculating low-Mach-number flows. Finite difference, volume, or element procedures can be used to discretize the characteristics-bias system. The algorithm in this paper has used a finite element discretization,

For any Mach number, the characteristics-bias system induces consistent upwinding along all wave-propagation directions radiating from any flow-field point. The upstream directions can be continuously updated and high-rate convergence to machine zero achieved without additional shock-capturing terms, data filtering or loss of essential monotonicity.

The formulation induces an anisotropic variable-strength upstream bias that directly correlates with the multi-dimensional spatial distribution of characteristic velocities. The magnitudes of the associated streamwise and crossflow dissipations remain different from and independent of each other, with crossflow dissipation that decreases for increasing Mach number. In this manner the

developed formulation will not generate for increasing Mach number as much crosswind dissipation as induced by an isotropic or direction-split formulation. The magnitude of the induced upstream bias, furthermore, depends on local solution smoothness. Only at solution discontinuities, e.g. a shock wave, is the induced upstreaming commensurate with a fully upwind formulation. In regions of solution continuity, the upwind-bias reduces to a minimum, which corresponds to minimal induced dissipation.

The operation count for this algorithm is comparable to that of a simple flux vector splitting algorithm. The developments in this study have employed basic four-noded cells. To determine the ultimate accuracy of bi-linear approximations of fluxes within four-noded cells, for a computationally efficient implementation, this study employs no MUSCL-type local extrapolation of dependent variables.

This report is organized in 11 sections and 7 appendices. After the introductory remarks in Section 1, Section 2 presents the governing equations and Sections 3 introduces the multi-dimensional non-discrete upstream-bias formulation. A multi-dimensional characteristics analysis for general equations of state is the subject of Section 4, followed in Section 5 by the determination of the multi-dimensional acoustics and convection components within the Euler flux jacobian. Section 6 presents the acoustics-convection characteristics Euler flux and Section 7 shows that this formulation is genuinely multi-dimensional. Section 8 presents the finite element discretization of the characteristics-bias system and Section 9 details the controller of induced upstream dissipation. Section 10 delineates a non-linearly stable implicit Runge-Kutta algorithm, with concluding remarks presented in Section 11. Appendices A-F delineate several ancillary mathematical developments and Appendix G contains a copy of an article on the 1-D version of this procedure, as published in the International Journal for Numerical Methods in Fluids.

2 Governing Equations

2.1 Navier-Stokes System

With respect to an inertial Cartesian reference frame and implied summation on repeated subscript indices, the Navier-Stokes conservation law system¹⁸ is

$$\frac{\partial q}{\partial t} + \frac{\partial f_j(q)}{\partial x_j} - \frac{\partial f_j^v(q)}{\partial x_j} = 0 \quad (1)$$

which consists of the continuity, momentum and total-energy equations. For 3-D flows, subscript j varies in the range $1 \leq j \leq 3$; with \mathcal{R} denoting the real-number field, the independent variable $(x, t) \equiv (x_1, x_2, x_3, t)$ in (1) varies in the domain $D \equiv \Omega \times [t_o, T]$, $[t_o, T] \in \mathcal{R}^+$, $\Omega \subset \mathcal{R}^3$. The dependent-variable array $q = q(x, t)$ and viscous and inviscid flux “vector” components $f_j^v = f_j^v(q)$ and $f_j = f_j(q)$ are then defined as

$$q \equiv \begin{Bmatrix} \rho \\ m_1 \\ m_2 \\ m_3 \\ E \end{Bmatrix}, \quad f_j^v(q) \equiv \begin{Bmatrix} 0 \\ \tau_{1j} \\ \tau_{2j} \\ \tau_{3j} \\ \frac{m_i}{\rho} \tau_{ij} - q_j^F \end{Bmatrix} \quad (2)$$

$$f_1(q) \equiv \begin{Bmatrix} m_1 \\ \frac{m_1}{\rho}m_1 + p \\ \frac{m_1}{\rho}m_2 \\ \frac{m_1}{\rho}m_3 \\ \frac{m_1}{\rho}(E + p) \end{Bmatrix}, \quad f_2(q) \equiv \begin{Bmatrix} m_2 \\ \frac{m_2}{\rho}m_1 \\ \frac{m_2}{\rho}m_2 + p \\ \frac{m_2}{\rho}m_3 \\ \frac{m_2}{\rho}(E + p) \end{Bmatrix}, \quad f_3(q) \equiv \begin{Bmatrix} m_3 \\ \frac{m_3}{\rho}m_1 \\ \frac{m_3}{\rho}m_2 \\ \frac{m_3}{\rho}m_3 + p \\ \frac{m_3}{\rho}(E + p) \end{Bmatrix} \quad (3)$$

In the array q , the variables ρ , m_1 , m_2 , m_3 , and E , respectively denote static density and volume-specific linear momentum components and total energy. Concerning the viscous and inviscid fluxes, the variables τ_{ij} , q_j^F and p respectively indicate the deviatoric stress-tensor components, the Fourier heat conduction flux component and static pressure. The eulerian flow velocity u , with cartesian components u_j , $1 \leq j \leq 3$, is then defined as $u \equiv m/\rho$.

2.2 Constitutive Relations

The components τ_{ij} of the deviatoric stress tensor are expressed as

$$\tau_{ij} = \mu \left(\frac{\partial u_i}{\partial x_j} + \frac{\partial u_j}{\partial x_i} \right) + \lambda \frac{\partial u_\ell}{\partial x_\ell} \delta_{ij}, \quad \lambda = -\frac{2}{3}\mu + \eta_B \quad (4)$$

where μ and λ respectively denote the first and second coefficient of viscosity, and η_B indicates bulk viscosity. For monoatomic gases η_B vanishes, while for other fluids, like air, Stokes' hypothesis $\lambda = -\frac{2}{3}\mu$ constitutes a reliable approximation.

The components q_j^F of the Fourier heat flux vector are expressed as

$$q_i = -k \frac{\partial T}{\partial x_i} \quad (5)$$

where T indicates static temperature and k denotes the coefficient of thermal conductivity.

2.3 Equations of State and Speed of Sound

For any homogeneous equilibrium gas, pressure can be expressed as a function of two other thermodynamic variables.¹⁹ They are density ρ and mass-specific internal energy ϵ , in this case, since they are readily available from the Euler system (1): ρ directly from the continuity equation in the system, and ϵ from q as

$$\epsilon \equiv \frac{E}{\rho} - \frac{1}{2\rho^2} (m_1^2 + m_2^2 + m_3^2) \quad (6)$$

The pressure equation of state thus becomes

$$p = p(\rho, \epsilon) = p \left(\rho, \frac{E}{\rho} - \frac{1}{2\rho^2} (m_1^2 + m_2^2 + m_3^2) \right) \quad (7)$$

According to this expression, the jacobian derivatives of p with respect to q , for the jacobian $\partial f_j / \partial q$ of $f_j(q)$, are not all independent of one another. The jacobian derivatives of (7) with respect to m_1 , m_2 , m_3 and E in fact satisfy the constraints

$$\frac{\partial p}{\partial m_1} = -\frac{m_1}{\rho} \frac{\partial p}{\partial E}, \quad \frac{\partial p}{\partial m_2} = -\frac{m_2}{\rho} \frac{\partial p}{\partial E}, \quad \frac{\partial p}{\partial m_3} = -\frac{m_3}{\rho} \frac{\partial p}{\partial E} \quad (8)$$

as obtained by expressing the derivatives of p with respect to m_1 , m_2 , m_3 and E in terms of the thermodynamic derivative of p with respect to ϵ , from the first expression in (7). In the following sections, for simplicity, the abridged notation

$$p_\rho \equiv \frac{\partial p}{\partial \rho} , \quad p_{m_1} \equiv \frac{\partial p}{\partial m_1} , \quad p_{m_2} \equiv \frac{\partial p}{\partial m_2} , \quad p_{m_3} \equiv \frac{\partial p}{\partial m_3} , \quad p_E \equiv \frac{\partial p}{\partial E} \quad (9)$$

will denote the jacobian derivatives of pressure. In terms of these derivatives, the square of the speed of sound c for general equations of state can be expressed¹⁷ as

$$c^2 \equiv \frac{\partial p}{\partial \rho} \Big|_S = p_\rho + p_E \left(\frac{E + p}{\rho} - \frac{1}{\rho^2} (m_1^2 + m_2^2 + m_3^2) \right) \quad (10)$$

This result, in particular, allows expressing the mass-specific total enthalpy H as

$$H = \frac{E + p}{\rho} = \frac{c^2 (1 + p_E M^2) - p_\rho}{p_E} \quad (11)$$

where $M \equiv \|u\|/c$ denotes the Mach number.

The specific perfect-gas expressions for (6) and (7) follow from the internal energy and equation of state

$$\epsilon = c_v T = \frac{R}{\gamma - 1} T , \quad p = \rho R T \quad (12)$$

for this type of gas, where c_v , T , R and γ respectively denote the constant-volume specific heat, static temperature, gas constant and specific-heat ratio. The elimination of T from these two expressions, along with (6), leads to the following familiar expressions for the equation of state for p in terms of q

$$p = (\gamma - 1) \rho \epsilon = (\gamma - 1) \left(E - \frac{1}{2\rho} (m_1^2 + m_2^2 + m_3^2) \right) \quad (13)$$

With this equation of state, the corresponding jacobian derivatives of pressure become

$$p_\rho = (\gamma - 1) \frac{m_1^2 + m_2^2 + m_3^2}{2\rho^2} , \quad p_{m_i} = -(\gamma - 1) \frac{m_i}{\rho} , \quad p_E = (\gamma - 1) \quad (14)$$

which satisfy (8). From (10), the perfect-gas speed of sound can be expressed as

$$c^2 = (\gamma - 1) \left[\frac{E + p}{\rho} - \frac{m_1^2 + m_2^2 + m_3^2}{2\rho^2} \right] \quad (15)$$

directly in terms of the dependent variables.

3 Non-Discrete Characteristics-Bias Approximation

The non-discrete, i.e. continuum or before discretization, characteristics-bias approximation of the Navier-Stokes equations is a system of equations that encompasses the Navier-Stokes equations (1) and also induces an authentically multi-dimensional solution-dependent upstream dissipation along not just select directions but all characteristic directions. This upstream dissipation originates from a multidimensional differential parabolic perturbation within the characteristics-bias system; this parabolic perturbation, in turn, emerges from a decomposition of the jacobian matrix of the multi-dimensional Euler flux f_j .

The development of a characteristics-bias approximation at the differential equation level, prior to the discretization in space, possesses distinctive advantages. For instance, the directions of this multi-dimensional upstream bias remain independent of any grid-line direction, and correlate with characteristic directions; furthermore a straightforward centered approximation of the characteristics-bias system automatically generates a genuinely multi-dimensional consistent upstream-bias approximation of the original Navier-Stokes equations, without any need for additional numerical dissipation terms. This formulation, therefore, induces but a minimal amount of upstream dissipation, that amount that leads to practically non-oscillatory accurate solutions.

Traditional discrete approximations of (1) originate from the integral statement

$$\int_{\hat{\Omega}} \hat{w} \left(\frac{\partial q}{\partial t} + \frac{\partial f_j(q)}{\partial x_j} - \frac{\partial f_j^v(q)}{\partial x_j} \right) d\Omega = 0 \quad (16)$$

which is equivalent to the governing system (1) for arbitrary subdomains $\hat{\Omega} \subset \Omega$ and arbitrary integrable test functions \hat{w} with compact support in $\hat{\Omega}$. For finite volume and element formulations, some upstream-bias approximations can emerge from this statement through numerical flux formulae for f_j and select choices for the test functions.

The characteristics-bias formulation rests on the characteristics-bias system

$$\frac{\partial q}{\partial t} + \frac{\partial f_j^C(q)}{\partial x_j} - \frac{\partial f_j^v(q)}{\partial x_j} = 0 \quad (17)$$

where f_j^C corresponds to a characteristics flux that automatically induces a multi-dimensional and infinite directional upstream-bias approximation for the Euler flux divergence $\frac{\partial f_j}{\partial x_j}$. The associated characteristic-bias integral is then defined as

$$\int_{\hat{\Omega}} \hat{w} \left(\frac{\partial q}{\partial t} + \frac{\partial f_j^C}{\partial x_j} - \frac{\partial f_j^v(q)}{\partial x_j} \right) d\Omega = 0 \quad (18)$$

Since the characteristics flux is developed independently and before any discretization, a genuinely multi-dimensional upstream-bias approximation for the Navier-Stokes equations (1) on arbitrary grids directly results from a straightforward centered discretization of this integral statement on any given grid. For finite element formulations, a multi-dimensional upstream-bias approximation of the Navier-Stokes equations emerges from the most basic Galerkin approximation of (18).

The following sections show that the divergence of the characteristics flux f_j^C naturally derives from an upstream-bias integral average as

$$\frac{\partial f_j^C}{\partial x_j} = \frac{\partial f_j}{\partial x_j} - \frac{\partial}{\partial x_i} \left(\varepsilon \psi \sum_{\ell=1}^L a_{i\ell} \alpha_\ell A_{\ell j} \frac{\partial q}{\partial x_j} \right) \quad (19)$$

In this expression, $A_{\ell j}$ corresponds to a matrix component of the Euler flux jacobian, such that the matrix $A_{\ell j} n_j$ has uniform-sign eigenvalues, where n_j denotes the j^{th} component of a unit vector along an arbitrary wave-propagation direction within conical regions within the flow field. The coefficients α_ℓ denote linear-combination functions, possibly depending upon q . The term $a_{i\ell}$ indicates the i^{th} direction cosine of a unit vector a_ℓ along the principal wave-propagation direction of wave “ ℓ ”, a convection or acoustic wave for instance. The positive ψ in (22), $0 < \psi < 1$, stands for a new “upstream-bias” controller, detailed in Section 9, which controls the amount of induced upstream-bias dissipation. This controller adjusts this dissipation depending on local solution non-smoothness. In regions of discontinuous solution slopes, this controller increases, to preserve numerical stability and capture shocks crisply; in regions of smooth solutions, the controller approaches

its minimum, to reduce upstream dissipation. In this manner, the characteristics-bias formulation generates minimal-upstream-dissipation solutions. The positive ε denotes a local length scale to ensure consistency of the characteristics-bias formulation. It is well known that any discrete approximate solution of the Navier-Stokes equations exactly solves not the Navier-Stokes equations, but an associate system of equations, also called the modified equations; as a maximum grid spacing within the discrete approximation approaches nought, the modified equations approach the Navier-Stokes equations and the discrete solution is expected to approach the exact solution of these equations. Within each cluster of nodes of a discretization grid, therefore, ε in (18) is set equal to a local grid spacing so that the discrete solution of (18) is expected to approach a solution of the Navier-Stokes equations as ε approaches nought.

The characteristics flux f_j^C depends on physical characteristic directions. Section 4, therefore, details a multi-dimensional characteristics analysis, which clarifies the interaction between acoustic and convection waves for all Mach numbers. Section 5 determines the acoustics and convection components within the jacobian matrices of the Euler flux. Section 6 then presents the acoustics-convection form of the characteristics flux divergence (19).

3.1 Flux Jacobian Decomposition and Upstream-Bias Integral Average

To develop the flux f_j^C , consider first the flux jacobian decomposition (FJD) into L contributions

$$\frac{\partial f_j}{\partial q} = \sum_{\ell=1}^L \alpha_\ell A_{\ell j} \quad \Rightarrow \quad \frac{\partial f_j}{\partial x_j} = \sum_{\ell=1}^L \alpha_\ell A_{\ell j} \frac{\partial q}{\partial x} \quad (20)$$

where α_ℓ denotes a linear-combination function, possibly depending upon q , $A_{\ell j}$ corresponds to a flux-jacobian matrix component such that the matrix $A_{\ell j} n_j$ has uniform-sign eigenvalues within a conical region spanned by n_j , within the flow domain.

An integral average of the Euler flux divergence $\frac{\partial f_j}{\partial x_j}$ as expressed through decomposition (20) becomes

$$\int_{\widehat{\Omega}} \widehat{w} \frac{\partial f_j}{\partial x_j} d\Omega = \int_{\widehat{\Omega}} \sum_{\ell=1}^L \widehat{w} \alpha_\ell A_{\ell j} \frac{\partial q}{\partial x_j} d\Omega \quad (21)$$

The flux f_j^C is therefore defined by way of an upstream-bias integral average as

$$\int_{\widehat{\Omega}} \widehat{w} \frac{\partial f_j^C}{\partial x_j} d\Omega = \int_{\widehat{\Omega}} \sum_{\ell=1}^L (\widehat{w} + \psi \delta_\ell \widehat{w}) \alpha_\ell A_{\ell j} \frac{\partial q}{\partial x_j} d\Omega \quad (22)$$

where the rhs integral provides an upstream bias for each matrix component within the FJD in (20).

The positive ψ in (22), $0 < \psi < 1$, stands for a new “upstream-bias” controller, which automatically adjusts the amount of induced upstream-bias diffusion, depending on local solution non-smoothness. The expression $\delta_\ell \widehat{w}$ denotes a directional variation of the test function \widehat{w} along the axis of a conical region within the flow domain. This variation induces the appropriate upstream-bias for the test function \widehat{w} for each “ ℓ ” component within (22). Depending on the physical significance, magnitude and algebraic sign of the eigenvalues of $A_{\ell j} n_j$, the variation $\delta_\ell \widehat{w}$ can vanish or become algebraically positive or negative, which corresponds to an upstream bias respectively in the negative or positive sense of the axis of each conical region.

3.2 Characteristics-Bias Flux

The directional variation $\delta_\ell \widehat{w}$ in (22) becomes

$$\delta_\ell \widehat{w} = \frac{\partial \widehat{w}}{\partial x_i} \delta_\ell x_i = \frac{\partial \widehat{w}}{\partial x_i} a_{i\ell} \varepsilon, \quad \delta_\ell x_i = a_{i\ell} \varepsilon \quad (23)$$

where ε denotes a local positive length scale and $a_{i\ell}$ indicates the i^{th} direction cosine of a unit vector \mathbf{a}_ℓ along the principal wave-propagation direction of wave “ ℓ ”.

With these specifications, the upstream-bias integral average (22) becomes

$$\int_{\hat{\Omega}} \hat{w} \frac{\partial f_j^C}{\partial x_j} d\Omega = \int_{\hat{\Omega}} \hat{w} \frac{\partial f_j}{\partial x_j} d\Omega + \int_{\hat{\Omega}} \varepsilon \psi \frac{\partial \hat{w}}{\partial x_i} \sum_{\ell=1}^L a_{i\ell} \alpha_\ell A_{\ell j} \frac{\partial q}{\partial x_j} d\Omega \quad (24)$$

Considering that \hat{w} has compact support in $\hat{\Omega}$, it vanishes on the boundary $\partial\hat{\Omega}$ of $\hat{\Omega}$. As a result, integrating (24) by parts generates

$$\int_{\hat{\Omega}} \hat{w} \left[\frac{\partial f_j^C}{\partial x_j} - \frac{\partial f_j}{\partial x_j} + \frac{\partial}{\partial x_i} \left(\varepsilon \psi \sum_{\ell=1}^L a_{i\ell} \alpha_\ell A_{\ell j} \frac{\partial q}{\partial x_j} \right) \right] d\Omega = 0 \quad (25)$$

which contains no boundary integrals. Since this integral must vanish for arbitrary test functions \hat{w} and domains $\hat{\Omega}$, its integrand must identically equal zero, which generates the following expression for the divergence of the characteristics flux f_j^C

$$\frac{\partial f_j^C}{\partial x_j} = \frac{\partial f_j}{\partial x_j} - \frac{\partial}{\partial x_i} \left(\varepsilon \psi \sum_{\ell=1}^L a_{i\ell} \alpha_\ell A_{\ell j} \frac{\partial q}{\partial x_j} \right) \quad (26)$$

This expression exhibits an upstream-bias artificial diffusion, in the form of a second-order differential expression with associated upstream-bias matrix

$$\mathcal{A} \equiv n_i \left(\sum_{\ell=1}^L a_{i\ell} \alpha_\ell A_{\ell j} \right) n_j \quad (27)$$

where n_i indicates the i^{th} direction cosine of a unit vector \mathbf{n} along an arbitrary wave-propagation direction. Appendix D shows that for physical consistency of the upstream bias in (22), (19) and associated mathematical stability of the corresponding second-order differential expression, all the eigenvalues of this upstream-bias matrix must be positive at every flow-field point and for any wave-propagation direction \mathbf{n} . This requirement implies a correct upstream along all directions radiating from any flow field point and thus becomes a fundamental upstream-bias stability condition.

From (19), an expression for the i^{th} component of the characteristics flux is

$$f_i^C = f_i - \varepsilon \psi \sum_{\ell=1}^L a_{i\ell} \alpha_\ell A_{\ell j} \frac{\partial q}{\partial x_j} \quad (28)$$

As a multi-dimensional expression, each cartesian component f_i^C also depends on the derivatives of the solution q along all cartesian coordinate directions. The continuum expression (19), or (28), thus constitutes a non-discrete generalization of the various numerical-flux formulae employed in several CFD upwind schemes. It encompasses, generalizes, and unifies flux-vector and flux-difference schemes as shown by the following representative 1-D examples.

3.2.1 van Leer's Formulation and Flux Vector Splitting

Consider the van Leer's formulation as a representative Flux Vector Splitting (FVS). In this formulation, the inviscid flux f is “split” as

$$f = f^{VL+} + f^{VL-} \quad (29)$$

where the jacobian matrices of f^{VL+} and f^{VL-} respectively possess non-negative and non-positive eigenvalues.

The FJD expression (20) encompasses (29) with $L = 2$ as

$$\sum_{\ell=1}^L \alpha_{\ell} A_{\ell} = \frac{\partial f^{VL+}}{\partial q} + \frac{\partial f^{VL-}}{\partial q} , \quad \alpha_1 = 1 , \quad \alpha_2 = 1 \quad (30)$$

The corresponding characteristics-bias flux divergence for van Leer's FVS accrues from (19) with $\psi = 1$, $a_1 = 1$, $a_2 = -1$ as

$$\frac{\partial f^C}{\partial x} = \frac{\partial f}{\partial x} - \frac{\partial}{\partial x} \left(\varepsilon \left(\frac{\partial f^{VL+}}{\partial q} - \frac{\partial f^{VL-}}{\partial q} \right) \frac{\partial q}{\partial x} \right) = \frac{\partial f}{\partial x} - \frac{\partial}{\partial x} \left(\varepsilon \left(\frac{\partial f^{VL+}}{\partial x} - \frac{\partial f^{VL-}}{\partial x} \right) \right) \quad (31)$$

which generalizes in the continuum the traditional numerical flux formulae for FVS constructions.

The associated upstream matrix \mathcal{A} is

$$\mathcal{A} = \frac{\partial f^{VL+}}{\partial q} - \frac{\partial f^{VL-}}{\partial q} \quad (32)$$

The upstream-bias stability condition, however, is not automatically satisfied, even though each of the two matrices $\left(\frac{\partial f^{VL+}}{\partial q} \right)$ and $\left(-\frac{\partial f^{VL-}}{\partial q} \right)$ has positive eigenvalues. This stability condition is not unconditionally satisfied because the sum of two positive-eigenvalue matrices does not necessarily yield a matrix with positive eigenvalues. As an example consider the following matrix sum of two positive-eigenvalue matrices

$$\begin{pmatrix} 2 & \sigma \\ 3 & 6 \end{pmatrix} = \begin{pmatrix} 1 & 0 \\ 3 & 2 \end{pmatrix} + \begin{pmatrix} 1 & \sigma \\ 0 & 4 \end{pmatrix} \quad (33)$$

where σ is a real number. One of the eigenvalues of this matrix sum is negative for $\sigma > 4$. For instance, for $\sigma = 7$ the eigenvalues are $+9$ and -1 .

Most likely, however, (32) satisfies the upstream-bias stability condition for most of the flow conditions considered in the technical literature, in view of the stable results reported. For subsonic flows, each of the two flux vector components in (29) remains unrelated to the physics of acoustics or convection. On the other hand, (29) is computationally advantageous, for it calls for the discretization of simple flux-vector components.

3.2.2 Roe's Formulation and Flux Difference Splitting

Consider next Roe's formulation as a representative Flux Difference Splitting (FDS) development. In this formulation, the inviscid flux jacobian of f is "split" as

$$\frac{\partial f}{\partial q} = X \Lambda^+ X^{-1} + X \Lambda^- X^{-1} \quad (34)$$

where X and $\Lambda = \Lambda^+ + \Lambda^-$ denote the right eigenvector matrix and eigenvalue diagonal matrix of the jacobian, all evaluated at special average values of q , with Λ^+ and Λ^- respectively containing non-negative and non-positive eigenvalues. The matrices at the rhs of (34), therefore, will respectively possess non-negative and non-positive eigenvalues.

The FJD expression (20) encompasses (34) with $L = 2$ as

$$\sum_{\ell=1}^L \alpha_{\ell} A_{\ell} = X \Lambda^+ X^{-1} + X \Lambda^- X^{-1} , \quad \alpha_1 = 1 , \quad \alpha_2 = 1 \quad (35)$$

The corresponding characteristics-bias divergence for Roe's formulation accrues from (19) with $\psi = 1$, $a_1 = 1$, $a_2 = -1$ as

$$\frac{\partial f^C}{\partial x} = \frac{\partial f}{\partial x} - \frac{\partial}{\partial x} \left(\varepsilon \left(X \Lambda^+ X^{-1} - X \Lambda^- X^{-1} \right) \frac{\partial q}{\partial x} \right) = \frac{\partial f}{\partial x} - \frac{\partial}{\partial x} \left(\varepsilon X (\Lambda^+ - \Lambda^-) X^{-1} \frac{\partial q}{\partial x} \right) \quad (36)$$

which generalizes in the continuum the traditional numerical flux formulae for FDS constructions.

The associated upstream matrix \mathcal{A} is

$$\mathcal{A} = X (\Lambda^+ - \Lambda^-) X^{-1} \quad (37)$$

which has non-negative eigenvalues and therefore automatically satisfies the upstream-bias stability condition for any flow state for which no eigenvalue vanishes. The discretization of (36) calls for more computational operations than (31), while each of the two rhs components in (34) lumps into one matrix the matrices representative of the distinct acoustics and convection wave propagation mechanisms. On the other hand, numerous numerical results bear out the accuracy of an FDS formulation.

4 Characteristics Analysis

Within a flow field, acoustic and convection waves propagate in infinitely many directions, and along each direction the associated propagation velocity also depends on the Mach number. This section introduces a new intrinsically multi-dimensional characteristics analysis based on a non-linear wave-like form of the solutions of the Euler equations. This analysis leads to the spatial distribution of multi-dimensional propagation velocities and shows that among all propagation directions the streamline and crossflow directions are principal propagation directions. This line of inquiry yields specific conditions for a physically coherent upstream bias formulation that remains consistent with multi-dimensional acoustic and convection wave propagation. Several details are presented in Appendix B, which also delineates a characteristic-surface analysis and indicates that the streamline and crossflow directions are principal directions of wave propagation in the time-space continuum.

4.1 Non-linear Wave-Like Solutions

With implied summation on repeated indices, the non-linear wave-like form of solutions q of the Euler equations is expressed as

$$q = q(\eta_1) \quad , \quad \eta_1 = \mathbf{x} \cdot \mathbf{n} - \lambda(q)t = x_j n_j - \lambda(q)t \quad (38)$$

where \mathbf{n} denotes a space-domain propagation-direction unit vector, independent of (\mathbf{x}, t) , and $\lambda = \lambda(q)$ indicates a wave-propagation velocity component along the \mathbf{n} direction. Appendix A delineates many important properties of non-linear wave-like solutions.

4.2 Characteristic Velocity Components

The solution-dependent velocity component $\lambda = \lambda(q)$ is determined by enforcing the condition that q as expressed in (38) satisfies the Euler equations. Appendix A shows that this condition yields the eigenvalue problem

$$\left(-\lambda(q)I + \frac{\partial f_j}{\partial q} n_j \right) \frac{\partial q}{\partial \eta_1} = 0 \quad (39)$$

For non-trivial solutions $\frac{\partial q}{\partial \eta_1}$, hence $q = q(\eta_1)$, the characteristic velocity components λ are thus the eigenvalues of the linear combination of flux vector jacobians

$$\frac{\partial f_j(q)}{\partial q} n_j = \quad (40)$$

$$\begin{pmatrix} 0 & & & & & & & 0 \\ -u_1 u_j n_j + p_\rho n_1 & , & u_1 n_1 + u_j n_j + p_{m_1} n_1 & , & u_1 n_2 + p_{m_2} n_1 & , & u_1 n_3 + p_{m_3} n_1 & , & p_E n_1 \\ -u_2 u_j n_j + p_\rho n_2 & , & u_2 n_1 + p_{m_1} n_2 & , & u_2 n_2 + u_j n_j + p_{m_2} n_2 & , & u_2 n_3 + p_{m_3} n_2 & , & p_E n_2 \\ -u_3 u_j n_j + p_\rho n_3 & , & u_3 n_1 + p_{m_1} n_3 & , & u_3 n_2 + p_{m_2} n_3 & , & u_3 n_3 + u_j n_j + p_{m_3} n_3 & , & p_E n_3 \\ u_j n_j (p_\rho - H) & , & H n_1 + u_j n_j p_{m_1} & , & H n_2 + u_j n_j p_{m_2} & , & H n_3 + u_j n_j p_{m_3} & , & u_j n_j (1 + p_E) \end{pmatrix}$$

For general equations of state, these eigenvalues have been exactly determined in closed form as

$$\lambda_{0,2}^{d_E} = u_j n_j \quad , \quad \lambda_{3,4}^{d_E} = u_j n_j \pm (p_\rho + p_E (H - u_j u_j))^{1/2} \quad (41)$$

where superscript d_E signifies dimensional Euler eigenvalues. Of interest, eigenvalues $\lambda_{3,4}^{d_E}$ directly incorporate a sound speed expression that coincides with the isentropic partial derivative of pressure (10). Through (10), therefore, these equilibrium-gas eigenvalues become

$$\lambda_{0,2}^{d_E} = u_j n_j \quad , \quad \lambda_{3,4}^{d_E} = u_j n_j \pm c \quad (42)$$

which have the same familiar form as the perfect-gas eigenvalues. The non-dimensional form of (42) follows from division by c , which supplies the Mach-number dependent expressions

$$\lambda_{0,2}^E = v_j n_j M \quad , \quad \lambda_{3,4}^E = v_j n_j M \pm 1 \quad (43)$$

where v_1 , v_2 and v_3 denote the components of a unit vector \mathbf{v} in the velocity \mathbf{u} direction.

As the inner product of the two unit vectors \mathbf{n} and \mathbf{v} , the contraction $v_j n_j$ supplies the cosine of the angle $(\theta - \theta_v)$ between \mathbf{n} and \mathbf{v} , where θ and θ_v respectively denotes the angle between \mathbf{n} and the x_1 axis and the angle between \mathbf{v} and the x_1 axis on any plane Π that contains the velocity vector. The eigenvalues (43) thus become

$$\lambda_{0,2}^E = \cos(\theta - \theta_v) M \quad , \quad \lambda_{3,4}^E = \cos(\theta - \theta_v) M \pm 1 \quad (44)$$

These expressions, in particular, imply that the Euler eigenvalues achieve their extrema for $\theta = \theta_v$, hence when \mathbf{n} points in the streamline direction, whereas for \mathbf{n} pointing in the crossflow direction, hence $\theta = 90^\circ + \theta_v$, these eigenvalues no longer depend upon M .

The convection eigenvalues $\lambda_{0,2}^E$ vanish when $\cos(\theta - \theta_v) = 0$, hence for \mathbf{n} perpendicular to the streamline direction, or, equivalently, pointing in the crossflow direction. Since $\|\cos(\theta - \theta_v)\| \leq 1$, the acoustic-convection eigenvalues $\lambda_{3,4}^E$ can only vanish for $M \geq 1$, hence for supersonic flows. For these flows, $\lambda_{3,4}^E = 0$ for

$$\mp \cos(\theta - \theta_v) = \pm \sin((\theta - 90^\circ) - \theta_v) = \frac{1}{M} \quad (45)$$

hence for \mathbf{n} perpendicular to the Mach lines, because $\pm((\theta - 90^\circ) - \theta_v)$ corresponds to the angle between a Mach line and the streamline, from the well known¹⁸ second expression in (45). The lines that are perpendicular to the Mach lines will be called “conjugate” lines.

The lines that are perpendicular to \mathbf{n} for vanishing eigenvalues $\lambda_{0,2}^E$ and $\lambda_{3,4}^E$ thus respectively become the streamline and Mach lines. This result is not coincidental, for vanishing eigenvalues $\lambda_{1,4}^E$ correspond to wave-like solutions of the steady Euler equations, for which the streamline and Mach lines are characteristic-wave propagation lines.

4.3 Polar Variation of Characteristic Speeds

Figure 1 presents the polar variation of the absolute values of eigenvalues (43) for subsonic, sonic and supersonic Mach numbers, in a neighborhood of a flow field point P on any plane Π that contains the velocity vector at P .

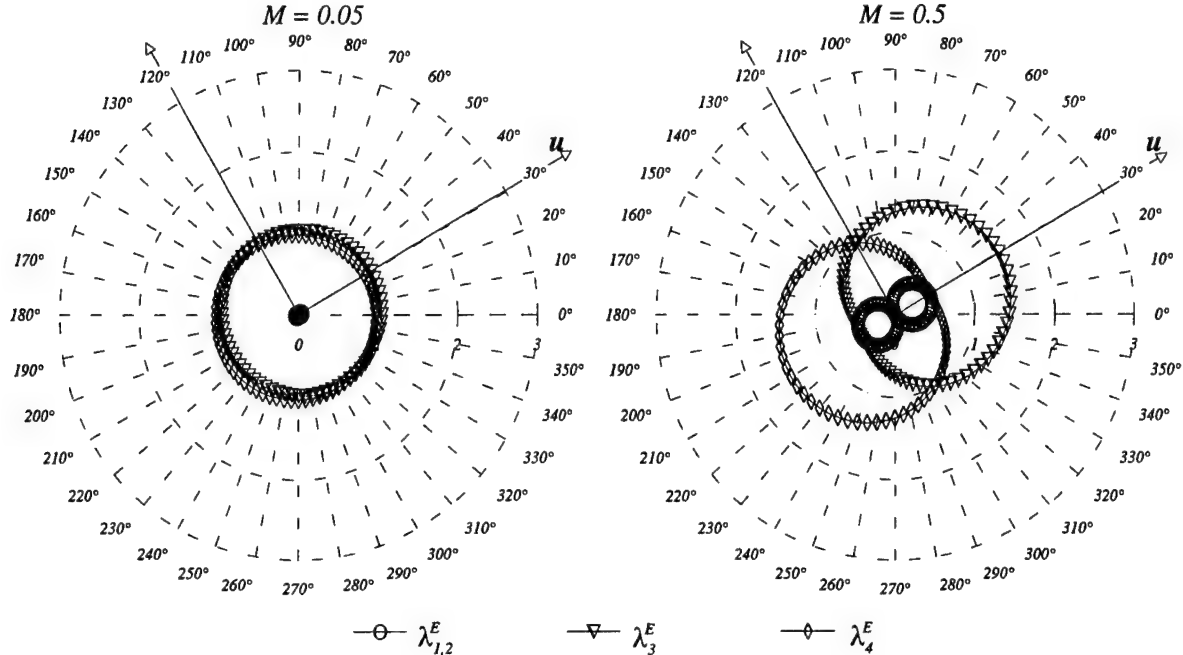


Figure 1: Polar Variation of Subsonic Wave Speeds

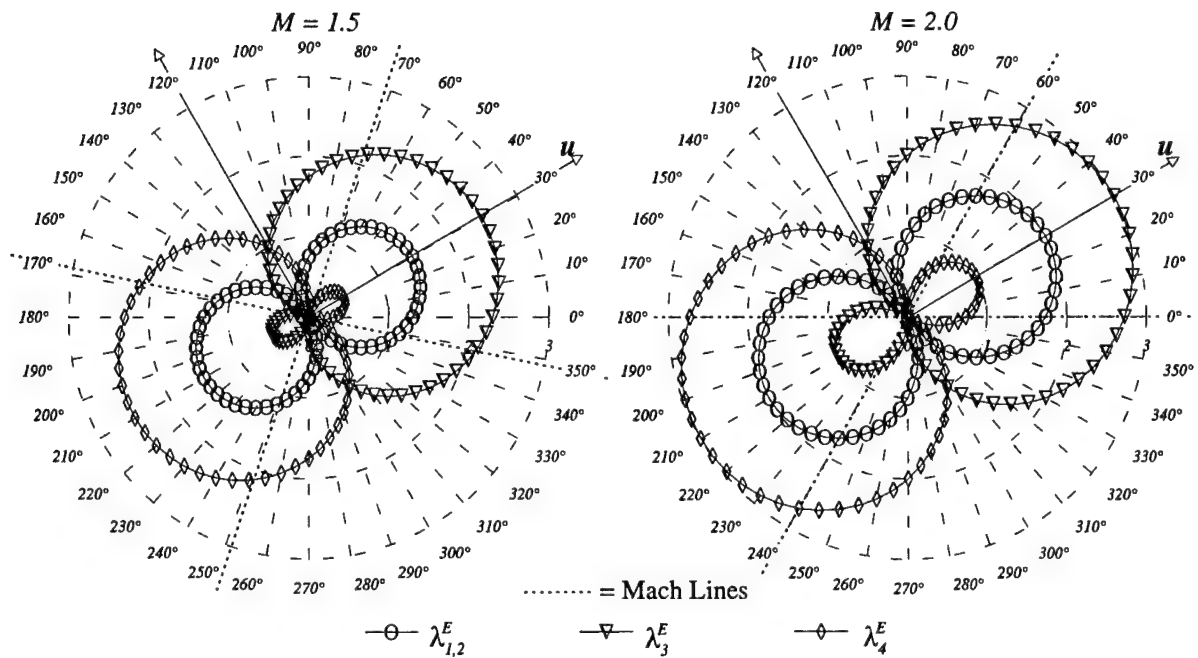


Figure 2: Polar Variation of Supersonic Wave Speeds

These variations are obtained for a variable unit vector $\mathbf{n} \equiv (\cos \theta, \sin \theta)$ and fixed unit vector \mathbf{v} , in this representative case inclined by $+30^\circ$ with respect to a reference x_1 axis on Π . A collective inspection of all these diagrams reveals three shared features for all Mach numbers. The maximum characteristic speeds occur in the velocity direction, i.e. along a streamline, as noted before. Secondly, all the characteristic speeds are symmetrically distributed about the streamline direction. Thirdly, the eigenvalue pairs $(\|\lambda_1^E\|, \|\lambda_2^E\|)$ and $(\|\lambda_3^E\|, \|\lambda_4^E\|)$ remain mirror skew-symmetric with respect to the crossflow direction, in the sense that the curves representative of $\|\lambda_2^E\|$ and $\|\lambda_4^E\|$ become the respective mirror images of the variations of $\|\lambda_1^E\|$ and $\|\lambda_3^E\|$ with reference to this direction. The streamline and crossflow directions, therefore, become two fundamental wave-propagation axes.

For vanishing Mach numbers, the acoustic-convection propagation curves in the figure approach two circumferences. The distribution of propagation speeds in this case is therefore isotropic, which corresponds to the direction-invariant propagation of acoustic waves. As the Mach number increases from zero, the curves in the figure progressively become circular asymmetric, which corresponds to anisotropic wave propagation. For $M = 0.5$ this anisotropy is already evident and becomes more pronounced for higher Mach numbers. The non-dimensional characteristic speeds then approach 1 in the region about the crossflow direction, which corresponds to essentially acoustic propagation.

For all Mach numbers, the convection eigenvalues $\lambda_{0,2}$ change sign when the \mathbf{n} -direction shifts from an upstream to a downstream axis with respect to \mathbf{u} . For this reason, the associated curves cross the polar origin. Pure convective propagation, therefore, remains mono-axial, from upstream to downstream of P , and the axis of this type of wave propagation is the streamline.

For subsonic Mach numbers the acoustic-convection eigenvalues λ_3^E and λ_4^E respectively remain positive and negative for all directions. For this reason the associated curves contain the polar origin. For subsonic flows, therefore, acoustic-convection waves propagate bi-modally, from both upstream and downstream toward and away from point P , along all directions radiating from P .

Beginning at the sonic state, this pattern drastically changes for supersonic Mach numbers. In this case both λ_3^E and λ_4^E change algebraic sign when the \mathbf{n} shifts from upstream to downstream of P along a streamline. For this reason, the associated curves cross the polar origin. For supersonic flows, therefore, acoustic-convection wave propagation becomes mono-axial along a streamline, from upstream to downstream of P .

4.4 Regions of Supersonic and Subsonic Wave Propagation

The streamline and crossflow directions are principal directions of gas dynamic acoustic and convection wave propagation. These directions become the axes of distinct wave-propagation regions, which in this report are named the streamline and crossflow wave propagation regions.

The supersonic mono-axial wave propagation pattern does not extend to the entire plane Π , but remains confined within two disconnected wedge regions about the streamline. About the crossflow direction, in fact, there exist two other wedge regions within which acoustic-convection wave propagation remains bi-modal, from both upstream and downstream toward and away from point P , even for supersonic flows. These regions are determined by finding the lines where the Euler eigenvalues vanish. These lines are the crossflow and conjugate lines, as shown for subsonic and supersonic flows in Figure 3, along with the bi-modal and mono-axial propagation regions, on plane Π , and the domain of dependence and region of influence of point P .

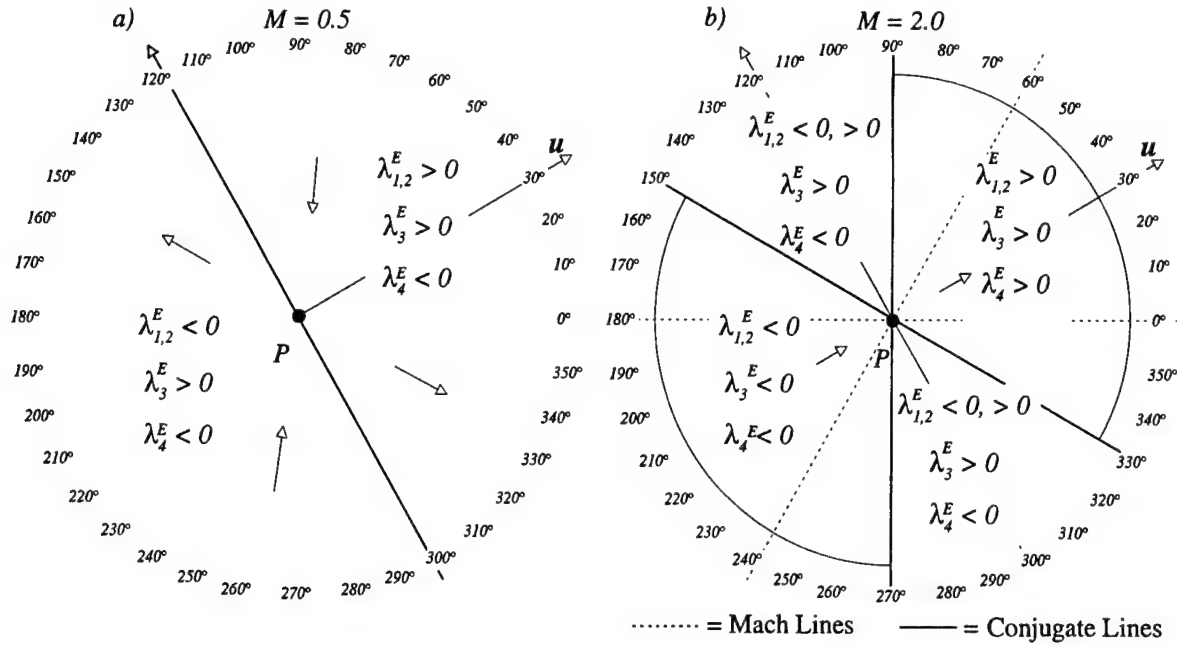


Figure 3: Wave Velocity Distribution: a) Subsonic Flows, b) Supersonic Flows

As Figure 3-a shows, subsonic acoustic-convection waves propagate bi-modally over the entire plane, hence the Euler eigenvalues do not all have the same algebraic sign. For supersonic flows, Figure 3-b shows the streamline regions of mono-axial wave propagation, where the Euler eigenvalues all have the same algebraic sign. The conjugate lines mark the boundary with the crossflow regions of bi-modal wave propagation, where the Euler eigenvalues do not all have the same algebraic sign, like the subsonic-flow situation. In particular, $\lambda_{0,2} < 0$ and $\lambda_{0,2} > 0$ respectively upstream and downstream of the crossflow direction.

Since the conjugate lines remain perpendicular to the Mach lines, it becomes easy to describe the growth of the mono-axial propagation regions as the Mach number increases. For $M < 1$, no mono-axial propagation region exists. For $M = 1$, the Mach lines coincide with the crossflow direction, the conjugate lines coincide with the streamline direction, hence the mono-axial propagation region consists of the streamline only. As the Mach number increases, the Mach lines approach the streamline and the conjugate lines approach the crossflow direction. The mono-axial propagation regions thus grow as circular sectors of increasing angle, and the bi-modal propagation regions simultaneously shrink. Only for a theoretically infinite M will the mono-axial propagation region spread throughout the entire plane Π . The presence, perhaps unexpected, of these bi-modal-propagation regions even for supersonic flows is readily reconciled with the existence of the domain of dependence and region of influence for P by the observation that the bi-modal-propagation regions simply correspond to spaces within the domains of dependence and ranges of influence of other flow field points besides P .

4.5 Physical Multi-dimensional Upstream Bias

Since for all Mach numbers there simultaneously exist regions of mono-axial and bi-modal propagation, a physically consistent, intrinsically multi-dimensional, and infinite directional upstream formulation for the Euler and Navier-Stokes equations has to provide an upstream approximation suitable for supersonic flows within the mono-axial region, but consistent with subsonic wave propagation within the bi-modal region. This formulation has to involve a streamline upstream ap-

proximation that remains bi-modal for subsonic flows and then becomes mono-axial for supersonic flows. For all Mach numbers, a physical upstream approximation must then induce a bi-modal upstream bias along the crossflow direction.

This upstream approximation has to introduce an upstream bias along all directions radiating from each flow field point. The bias in this approximation must change with varying direction and correlate with the directional distribution of the characteristic propagation speeds. Furthermore, the directional distribution of the upstream bias must remain symmetrical like the propagation speeds with respect to both the crossflow and streamline directions on any plane Π that contains the velocity vector.

The formulation presented in this report first identifies the genuine streamline and crossflow convection and acoustics components within the flux jacobian matrices. The formulation then establishes a physically consistent upstream approximation for each of these components, along all wave-propagation directions, with an upstream-bias magnitude that correlates with the directional distribution of the characteristic propagation speeds. For increasing Mach numbers, from zero to arbitrarily high, the approximation gradually changes from bi-modal in subsonic flows to mono-axial in supersonic flows, within the domain of dependence and range of influence of each flow-field point, while remaining bi-modal for all Mach numbers within an appropriate region about the crossflow direction.

5 Acoustics-Convection Flux Jacobian Components

This section determines the flux jacobian components that correspond to multidimensional convection and acoustics. The characteristic analysis of the acoustics components shows that the three-dimensional isotropic acoustic propagation naturally decomposes into three directional propagations, the first along the streamline direction and the remaining two along any two mutually perpendicular crossflow directions; these two cross flow propagation, in particular, combine into a two-dimensional isotropic acoustic propagation on any plane perpendicular to the velocity direction.

5.1 Convection and Pressure-Gradient Components

The flux divergence $\frac{\partial f_j}{\partial x_j}$ can be decomposed into convection and pressure-gradient components as

$$\frac{\partial f_j}{\partial x_j} = \frac{\partial f_j^q}{\partial x_j} + \frac{\partial f_j^p}{\partial x_j} \quad (46)$$

where f_j^q and f_j^p respectively denote the convection and pressure flux components, defined as

$$f_j^q(q) \equiv \begin{Bmatrix} m_j \\ \frac{m_j}{\rho} m_1 \\ \frac{m_j}{\rho} m_2 \\ \frac{m_j}{\rho} m_3 \\ \frac{m_j}{\rho} (E + p) \end{Bmatrix} = \frac{m_j}{\rho} \cdot \begin{Bmatrix} \rho \\ m_1 \\ m_2 \\ m_3 \\ E + p \end{Bmatrix}, \quad f_j^p(q) \equiv \begin{Bmatrix} 0 \\ p\delta_1^j \\ p\delta_2^j \\ p\delta_2^j \\ 0 \end{Bmatrix} \quad (47)$$

For supersonic flows, the Euler eigenvalues (42), associated with $\frac{\partial f_j}{\partial x_j}$ all have the same algebraic sign within the streamline region and the entire flux divergence can be upstream approximated along the streamline principal direction, within this region. For subsonic flows these eigenvalues have mixed algebraic sign and an upstream approximation for the flux divergence along one single direction remains inconsistent with the two-way propagation of acoustic waves. Without the pressure gradient in the momentum equation, however, the corresponding flux-jacobian eigenvalues all have the same algebraic sign⁹ within the streamline region and the resulting convection flux divergence can then be upstream approximated along one single direction. The flux divergence can thus be decomposed as the linear combination

$$\frac{\partial f_j}{\partial x_j} = \left[\frac{\partial f_j^q}{\partial x_j} + \beta \frac{\partial f_j^p}{\partial x_j} \right] + \left[(1 - \beta) \frac{\partial f_j^p}{\partial x_j} \right], \quad 0 \leq \beta \leq 1 \quad (48)$$

where the positive pressure-gradient partition function β can be chosen in such a way that all the eigenvalues associated with each of the two components between brackets in (48) keep the same algebraic sign within the streamline region, for all Mach numbers. In this manner, these entire components can be upstream approximated along the streamline. This choice for β is possible because the eigenvalues of a matrix are continuous functions of the matrix entries¹⁰ and hence all the eigenvalues for the components in (48) will continuously depend upon β . The function β will gradually increase toward 1 for increasing Mach number, so that an upstream approximation for the components in (48) smoothly approaches and then becomes an upstream approximation for the entire $\frac{\partial f_j}{\partial x_j}$ along the streamline, which also ensures consistency with 1-D formulations. Decomposition (48) is thus used for an upstream approximation of the flux divergence within the streamline region, for subsonic and supersonic flows.

Decomposition (48), however, is insufficient for an accurate multi-dimensional upstream modeling of acoustic waves, for a large Mach number range within the crossflow region and for low and vanishing Mach numbers within the streamline region. Concerning the cross-flow region, the eigenvalues associated with (48) become the Euler eigenvalues (42) for $\beta = 1$, hence for supersonic flows. As indicated in Section 4, these eigenvalues do not all have the same algebraic sign within the cross-flow wave propagation region. A mono-axial upstream-bias approximation of (48) within the cross-flow region, therefore, remains inconsistent with the existing two-way wave propagation in this region. Concerning the streamline wave propagation region, for a Mach number that approaches zero, the Euler eigenvalues (42) can all keep the same algebraic sign only if the sound speed contribution vanishes, which corresponds to a vanishing pressure gradient contribution and hence β approaching zero.⁹ But for β approaching zero, the eigenvalues associated with the components in (48) approach the eigenvalues of the jacobians

$$\frac{\partial f_j^q(q)}{\partial q} n_j = \begin{pmatrix} 0 & , & n_1 & , & n_2 & , & n_3 & , & 0 \\ -u_1 u_j n_j & , & u_1 n_1 + u_j n_j & , & u_1 n_2 & , & u_1 n_3 & , & 0 \\ -u_2 u_j n_j & , & u_2 n_1 & , & u_2 n_2 + u_j n_j & , & u_2 n_3 & , & 0 \\ -u_3 u_j n_j & , & u_3 n_1 & , & u_3 n_2 & , & u_3 n_3 + u_j n_j & , & 0 \\ u_j n_j (p_\rho - H) & , & H n_1 + u_j n_j p_{m_1} & , & H n_2 + u_j n_j p_{m_2} & , & H n_3 + u_j n_j p_{m_3} & , & u_j n_j (1 + p_E) \end{pmatrix} \quad (49)$$

and

$$\frac{\partial f_j^p(q)}{\partial q} n_j = \begin{pmatrix} 0 & 0 & 0 & 0 & 0 \\ p_\rho n_1 & p_{m_1} n_1 & p_{m_2} n_1 & p_{m_3} n_1 & p_E n_1 \\ p_\rho n_2 & p_{m_1} n_2 & p_{m_2} n_2 & p_{m_3} n_2 & p_E n_2 \\ p_\rho n_3 & p_{m_1} n_3 & p_{m_2} n_3 & p_{m_3} n_3 & p_E n_3 \\ 0 & 0 & 0 & 0 & 0 \end{pmatrix} \quad (50)$$

Using the pressure-derivative identity (8) the eigenvalues of these jacobians respectively are

$$\lambda_{0,3}^q = u_j n_j, \quad \lambda_4^q = u_j n_j (1 + p_E) \quad (51)$$

and

$$\lambda_{0,3}^p = 0, \quad \lambda_4^p = -u_j n_j p_E \quad (52)$$

which certainly all keep the same algebraic sign for any wave propagation direction, but for vanishing Mach number remain far less than the dominant speed of sound c . For low Mach numbers, therefore, an upstream approximation for the components in (48) would inaccurately model the physics of acoustics. This difficulty is resolved by further decomposing the pressure gradient in (48) in terms of genuine streamline and crossflow acoustic components, for accurate upstream modeling of acoustic waves throughout the flow field.

5.2 Acoustic Equations

Let (v_1, v_2, v_3) denote the components of a unit vector \mathbf{v} locally parallel to the velocity \mathbf{u} . Upon expressing the velocity components (u_1, u_2, u_3) in terms of the Mach number M as

$$(u_1, u_2, u_3) = cM(v_1, v_2, v_3) \quad (53)$$

and using the pressure derivative identities (8), the Euler system becomes

$$\frac{\partial}{\partial t} \begin{pmatrix} \rho \\ m_1 \\ m_2 \\ m_3 \\ E \end{pmatrix} + \left[\begin{pmatrix} 0 & \delta_1^j & \delta_2^j & \delta_3^j & 0 \\ p_\rho \delta_1^j & 0 & 0 & 0 & p_E \delta_1^j \\ p_\rho \delta_2^j & 0 & 0 & 0 & p_E \delta_2^j \\ p_\rho \delta_3^j & 0 & 0 & 0 & p_E \delta_3^j \\ 0 & H \delta_1^j & H \delta_2^j & H \delta_3^j & 0 \end{pmatrix} + cMC_j \right] \frac{\partial}{\partial x_j} \begin{pmatrix} \rho \\ m_1 \\ m_2 \\ m_3 \\ E \end{pmatrix} = 0 \quad (54)$$

where δ_i^j and C_j respectively denote Kronecker's delta and a completion matrix. The form of this matrix is $C_j \equiv$

$$\begin{pmatrix} 0 & 0 & 0 & 0 & 0 \\ -v_1 u_j & v_1 \delta_1^j + v_j - v_1 p_E \delta_1^j & v_1 \delta_2^j - v_2 p_E \delta_1^j & v_1 \delta_3^j - v_3 p_E \delta_1^j & 0 \\ -v_2 u_j & v_2 \delta_1^j - v_1 p_E \delta_2^j & v_2 \delta_2^j + v_j - v_2 p_E \delta_2^j & v_2 \delta_3^j - v_3 p_E \delta_2^j & 0 \\ -v_3 u_j & v_3 \delta_1^j - v_1 p_E \delta_3^j & v_3 \delta_2^j - v_2 p_E \delta_3^j & v_3 \delta_3^j + v_j - v_3 p_E \delta_3^j & 0 \\ v_j (p_\rho - H) & -v_j u_1 p_E & -v_j u_2 p_E & -v_j u_3 p_E & v_j (1 + p_E) \end{pmatrix} \quad (55)$$

For a vanishing M these equations then reduce to the acoustics equations

$$\frac{\partial}{\partial t} \begin{pmatrix} \rho \\ m_1 \\ m_2 \\ m_3 \\ E \end{pmatrix} + \left[\begin{pmatrix} 0 & \delta_1^j & \delta_2^j & \delta_3^j & 0 \\ p_\rho \delta_1^j & 0 & 0 & 0 & p_E \delta_1^j \\ p_\rho \delta_2^j & 0 & 0 & 0 & p_E \delta_2^j \\ p_\rho \delta_3^j & 0 & 0 & 0 & p_E \delta_3^j \\ 0 & H \delta_1^j & H \delta_2^j & H \delta_3^j & 0 \end{pmatrix} \right] \frac{\partial}{\partial x_j} \begin{pmatrix} \rho \\ m_1 \\ m_2 \\ m_3 \\ E \end{pmatrix} = 0 \quad (56)$$

for which $A_j^{a_0}$ will denote the acoustics matrix multiplying the gradient of q in (56). The dependent variables in these equations obviously correspond to those in a flow field that originates from slight perturbations to an otherwise quiescent field.

Heed, in particular, that in this case the energy equation toward steady state is no longer linearly independent from the continuity equation. Moreover, the momentum equations become linearly dependent upon each other for steady wave-like solutions $q = q(\tilde{\eta}_1) = q(x_j n_j)$. For these solutions, in fact, the acoustics momentum equations become

$$p_\rho \frac{\partial \rho}{\partial \tilde{\eta}_1} n_i + p_E \frac{\partial E}{\partial \tilde{\eta}_1} n_i \quad , \quad 1 \leq i \leq 3 \quad (57)$$

This linear-dependence phenomenon directly explains the widely reported convergence difficulties towards steady state experienced in the CFD simulation of incompressible, i.e. low-Mach-number, flows with a compressible flow formulation. The infinite-directional algorithm detailed in this report will incorporate a convenient upstream-bias expression to eliminate within the discrete equations this steady-state linear-dependence phenomenon.

As Appendix A shows, the propagation velocity components λ for a wave-like solution (38) of this system correspond to the eigenvalues of the matrix $A_j^{a_0} n_j$, which are

$$\lambda_{0,2}^{a_0} = 0 \quad , \quad \lambda_{3,4}^{a_0} = \pm (p_\rho + p_E H)^{1/2} = \pm \left(\frac{\partial p}{\partial \rho} \Big|_S \right)^{1/2} \Rightarrow H = \frac{c^2 - p_\rho}{p_E} \quad (58)$$

and remain independent from the wave-propagation direction unit vector \mathbf{n} . Both c and the eigenvalues $\lambda_{3,4}^{a_0}$ in (58) correspond to the zero-Mach-number isentropic speed of sound (10). With $\lambda_{0,2}^{a_0} = 0$, the propagation of acoustic waves governed by this system, therefore, corresponds to an isentropic process with negligible flow kinetic energy.

Equations (56) contain the important partial-derivative relations

$$\frac{\partial E}{\partial x_i} = \frac{c^2 - p_\rho}{p_E} \frac{\partial \rho}{\partial x_i} \quad , \quad \frac{\partial \rho}{\partial x_i} = \frac{p_E}{c^2 - p_\rho} \frac{\partial E}{\partial x_i} \quad (59)$$

which result from the momentum equations by expressing p_ρ therein using (11) as

$$\begin{aligned} \frac{\partial m_i}{\partial t} &= -\frac{\partial p}{\partial x_i} = -p_\rho \frac{\partial \rho}{\partial x_i} - p_E \frac{\partial E}{\partial x_i} = \\ &- \left(\frac{\partial p}{\partial \rho} \Big|_S - p_E \frac{E + p}{\rho} \right) \frac{\partial \rho}{\partial x_i} - p_E \frac{\partial E}{\partial x_i} = -\frac{\partial p}{\partial \rho} \Big|_S \frac{\partial \rho}{\partial x_i} - p_E \left(\frac{\partial E}{\partial x_i} - \frac{E + p}{\rho} \frac{\partial \rho}{\partial x_i} \right) \end{aligned} \quad (60)$$

For an isentropic flow $p = p(\rho)$, hence the first rhs term in (60) equals $\frac{\partial p}{\partial x_i}$. The second rhs term must consequently vanish, which returns results (59).

On the basis of (59) the acoustics equations become

$$\begin{cases} \frac{\partial \rho}{\partial t} &= -\frac{\partial m_i}{\partial x_j} \\ \frac{\partial m_i}{\partial t} &= -c^2 \frac{\partial \rho}{\partial x_i} \end{cases} \quad (61)$$

For wave-like fields, these equations yield the fundamental result

$$\frac{\partial m_i}{\partial x_k} n_k = \frac{\partial m_j}{\partial x_j} n_i \quad (62)$$

as obtained from expressions (137) in Appendix A. Specifically, the first of (137) for m_i and the second of (137) for ρ are inserted into the momentum equations in (61) to substitute for $\frac{\partial m_i}{\partial t}$ and $\frac{\partial \rho}{\partial x_i}$. The partial derivative $\frac{\partial \rho}{\partial t}$ in the resulting momentum equations is then replaced by the continuity equation in (61), which leads to (62). These expressions then simplify to

$$\begin{aligned}\frac{\partial m_1}{\partial x_2} n_2 + \frac{\partial m_1}{\partial x_3} n_3 &= \frac{\partial m_2}{\partial x_2} n_1 + \frac{\partial m_3}{\partial x_3} n_1 \\ \frac{\partial m_2}{\partial x_1} n_1 + \frac{\partial m_2}{\partial x_3} n_3 &= \frac{\partial m_1}{\partial x_1} n_2 + \frac{\partial m_3}{\partial x_3} n_2 \\ \frac{\partial m_3}{\partial x_1} n_1 + \frac{\partial m_3}{\partial x_2} n_2 &= \frac{\partial m_1}{\partial x_1} n_3 + \frac{\partial m_2}{\partial x_2} n_3\end{aligned}\quad (63)$$

Results (59), (62), and (63) are used in Section 5.3.2 to simplify an upstream-bias formulation for the acoustic components within the Euler flux jacobian.

5.3 Acoustic Components

For arbitrary Mach numbers and corresponding dependent variables ρ , m_1 , m_2 , m_3 , and E , the Euler flux jacobians in (40) can be decomposed as

$$\frac{\partial f_j}{\partial q} = \frac{\partial f_j^q}{\partial q} + \frac{\partial f_j^p}{\partial q} = \frac{\partial f_j^q}{\partial q} + A_j^a + A_j^{nc} \quad (64)$$

where, with reference to the acoustics equations (56), the matrices A_j^a and A_j^{nc} are defined as

$$A_j^a \equiv \begin{pmatrix} 0 & \delta_1^j & \delta_2^j & \delta_3^j & 0 \\ p_\rho \delta_1^j & 0 & 0 & 0 & p_E \delta_1^j \\ p_\rho \delta_2^j & 0 & 0 & 0 & p_E \delta_2^j \\ p_\rho \delta_3^j & 0 & 0 & 0 & p_E \delta_3^j \\ 0 & \frac{c^2 - p_\rho}{p_E} \delta_1^j & \frac{c^2 - p_\rho}{p_E} \delta_2^j & \frac{c^2 - p_\rho}{p_E} \delta_3^j & 0 \end{pmatrix} \quad (65)$$

$$A_j^{nc} \equiv \begin{pmatrix} 0 & -\delta_1^j & -\delta_2^j & -\delta_3^j & 0 \\ 0 & p_{m_1} \delta_1^j & p_{m_2} \delta_1^j & p_{m_3} \delta_1^j & 0 \\ 0 & p_{m_1} \delta_2^j & p_{m_2} \delta_2^j & p_{m_3} \delta_2^j & 0 \\ 0 & p_{m_1} \delta_3^j & p_{m_2} \delta_3^j & p_{m_3} \delta_3^j & 0 \\ 0 & -\frac{c^2 - p_\rho}{p_E} \delta_1^j & -\frac{c^2 - p_\rho}{p_E} \delta_2^j & -\frac{c^2 - p_\rho}{p_E} \delta_3^j & 0 \end{pmatrix} \quad (66)$$

Heed, in particular that no flux component of $f_j(q)$ exists, of which the jacobian equals A_j^a . The eigenvalues of the matrix $A_j^{nc} n_j$ have been determined in closed form as

$$\lambda_{0,3}^{nc} = 0, \quad \lambda_4^{nc} = -cM p_E v_j n_j \quad (67)$$

which become infinitesimal for vanishing M . The matrix A_j^{nc} can be termed a “non-linear coupling” matrix, for it completes the non-linear coupling between convection and acoustics within (64) so that the two Euler eigenvalues $\lambda_{3,4}^{nc}$ in (42) do correspond to the sum of convection and acoustic speeds. Since the matrix A_j^a will be used in the upstream-bias formulation for small Mach numbers only and considering that the eigenvalues in (67) vanish for these Mach numbers and also for n pointing in the crossflow direction, for which $v_j n_j = 0$, no need exists to involve A_j^{nc} in the upstream-bias approximation of the flux jacobian (40).

The eigenvalues of $A_j^a n_j$ have been exactly determined in closed form as

$$\lambda_{0,2}^a = 0 \quad , \quad \lambda_{3,4}^a = \pm c \quad (68)$$

and remain independent of the propagation vector \mathbf{n} , which signifies isotropic propagation. The matrix A_j^a , therefore, can be termed the “acoustics” matrix, for its eigenvalues, unlike (51)-(52) approach the speed of sound c for decreasing Mach number. This matrix, therefore, can be used for an upstream-bias approximation of the Euler equations in the low Mach-number regime, within the streamline region, and for any Mach number, within the crossflow region.

5.3.1 Streamline and Crossflow Components

For any three mutually orthogonal unit vectors $\mathbf{a} = (a_1, a_2, a_3)$, $\mathbf{a}^{N_1} = (a_1^{N_1}, a_2^{N_1}, a_3^{N_1})$, and $\mathbf{a}^{N_2} = (a_1^{N_2}, a_2^{N_2}, a_3^{N_2})$ within a 3-D flow, along with implied summation on repeated indices, the acoustics component within the Euler flux divergence can be expressed as

$$A_j^a \frac{\partial q}{\partial x_j} = A_j^a a_j a_k \frac{\partial q}{\partial x_k} + A_j^a a_j^{N_1} a_k^{N_1} \frac{\partial q}{\partial x_k} + A_j^a a_j^{N_2} a_k^{N_2} \frac{\partial q}{\partial x_k} \quad (69)$$

For \mathbf{a} parallel to \mathbf{u} , this expression corresponds to a decomposition of the Euler acoustics component into one streamline and two crossflow acoustics components. For wave-like solutions (38), three eigenvalues of each component vanish; the remaining eigenvalues of these three separate components have been determined as

$$\lambda_{3,4}^s = \pm c a_j n_j \quad , \quad \lambda_{3,4}^{N_1} = \pm c a_j^{N_1} n_j \quad , \quad \lambda_{3,4}^{N_2} = \pm c a_j^{N_2} n_j \quad (70)$$

The two non-vanishing eigenvalues associated with the entire acoustics component at the lhs of (69), but as expressed as the rhs combination of streamline and crossflow components have then been determined as

$$\lambda_{3,4}^a = c \left((a_j n_j)^2 + (a_j^{N_1} n_j)^2 + (a_j^{N_2} n_j)^2 \right)^{1/2} \quad , \quad (a_j n_j)^2 + (a_j^{N_1} n_j)^2 + (a_j^{N_2} n_j)^2 = 1 \quad (71)$$

which shows that the square of the acoustic eigenvalues (68) equals the sum of the square of the streamline and crossflow acoustic eigenvalues (70). On any plane Π that contains \mathbf{a} , \mathbf{a}^{N_1} and \mathbf{n} , therefore, acoustic propagation naturally decomposes into two directional components, one along \mathbf{a} and the other along \mathbf{a}^{N_1} , as illustrated in Figure 4.

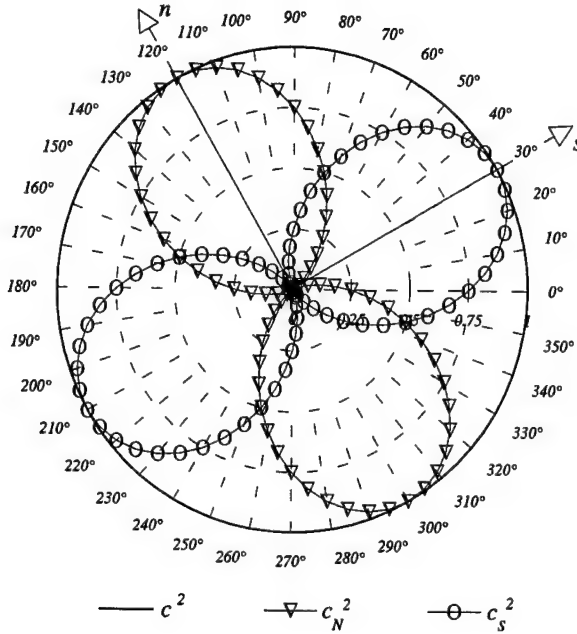


Figure 4: Polar Variation of Square of Acoustic Speeds on Plane II

This planar two-direction acoustic decomposition remains unaltered on plane Π , as this plane spans the entire 3-D space by rotating about the line of \mathbf{a} . Acoustic propagation, therefore, decomposes into a directional component along \mathbf{a} and an isotropic component on any plane orthogonal to \mathbf{a} . This result also follows from the expression

$$(a_j^{N_1} n_j)^2 + (a_j^{N_2} n_j)^2 = 1 - (a_j n_j)^2 \quad (72)$$

from (71), which shows that acoustic propagation on the plane of \mathbf{a}^{N_1} and \mathbf{a}^{N_2} only depends upon $(a_j n_j)$, hence on the angle between \mathbf{a} and \mathbf{n} . For any such angle, the “lhs” of (72) remains constant for any orientation of \mathbf{n} with respect to \mathbf{a}^{N_1} and \mathbf{a}^{N_2} . This result indicates that (72) is the equation of a circle, which signifies isotropic acoustic propagation on the plane of \mathbf{a}^{N_1} and \mathbf{a}^{N_2} .

For \mathbf{a} , \mathbf{a}^{N_1} , and \mathbf{a}^{N_2} respectively pointing in the streamline and two mutually perpendicular crossflow directions, the Euler flux divergence can then be decomposed as

$$\frac{\partial f_j(q)}{\partial x_j} = \bar{\alpha} A_j^a a_j a_k \frac{\partial q}{\partial x_k} + A_j^a a_j^{N_1} a_k^{N_1} \frac{\partial q}{\partial x_k} + A_j^a a_j^{N_2} a_k^{N_2} \frac{\partial q}{\partial x_k} + \frac{\partial f_j^q}{\partial x_j} + (1 - \bar{\alpha}) A_j^a a_j a_k \frac{\partial q}{\partial x_k} + A_j^{nc} \frac{\partial q}{\partial x_j} \quad (73)$$

The weights 1 and $\bar{\alpha}$, $1 \leq \bar{\alpha} \leq 0$, respectively for the crossflow and streamline components in this expression are different from each other because the streamline and crossflow characteristic velocity components remain distinct from each other, following the Euler eigenvalues (42); furthermore, the pressure-gradient term in decomposition (48) will contribute different characteristic velocity components along the streamline and crossflow directions. The magnitudes of needed acoustic upstream bias for (73) along these three directions, therefore, will have to differ from one another and this “differential” upstream bias can be easily instituted through the distinct weights $\bar{\alpha}$ and 1 on the streamline and crossflow components.

5.3.2 Absolute Acoustics Matrices

Despite its zero eigenvalues, $A_j^a a_j$ features a complete set of eigenvectors X , detailed in Appendix C, and thus possesses the similarity-transformation form

$$A_j^a a_j = X \Lambda^a X^{-1} = X \Lambda^{a+} X^{-1} + X \Lambda^{a-} X^{-1} , \quad \Lambda^a = \Lambda^{a+} + \Lambda^{a-} \quad (74)$$

where the diagonal matrices Λ^{a+} and Λ^{a-} only contain $\pm c$ along their diagonals. The matrices $X \Lambda^{a+} X^{-1}$ and $X \Lambda^{a-} X^{-1}$ respectively correspond to the “forward” and “backward” acoustic-propagation matrix components of $A_j^a a_j$. A bi-modal upstream-bias approximation of $A_j^a a_j$, therefore, readily follows from instituting a forward and a backward upstream-bias approximation respectively for the forward- and backward- propagation matrices in (74). Results similar to (74) then readily follow by replacing a with a^{N_1} and a^{N_2} . This bi-modal approximation directly yields both the non-negative-eigenvalue matrices $|A_j^a a_j| \equiv X (\Lambda^{a+} - \Lambda^{a-}) X^{-1}$

$$|A_j^a a_j^{N_1}| \equiv X_{N_1} (\Lambda^{a+} - \Lambda^{a-}) X_{N_1}^{-1} , \quad |A_j^a a_j^{N_2}| \equiv X_{N_2} (\Lambda^{a+} - \Lambda^{a-}) X_{N_2}^{-1} \quad (75)$$

and the associated matrix product $|A_j^a a_j| a_k \partial q / \partial x_k$. The matrices in (75) correspond to the streamline and crossflow absolute acoustics matrices. With reference to the results in Appendix C, the unabridged form of the matrix product $|A_j^a a_j| a_k \partial q / \partial x_k$ has been determined as

$$|A_j^a a_j| a_k \frac{\partial q}{\partial x_k} = \begin{pmatrix} p_\rho / c & , & 0 & , & 0 & , & p_E / c \\ 0 & , & a_1^2 c & , & a_1 a_2 c & , & a_1 a_3 c & , & 0 \\ 0 & , & a_2 a_1 c & , & a_2^2 c & , & a_2 a_3 c & , & 0 \\ 0 & , & a_3 a_1 c & , & a_3 a_2 c & , & a_3^2 c & , & 0 \\ (c^2 - p_\rho) p_\rho / (c p_E) & , & 0 & , & 0 & , & 0 & , & (c^2 - p_\rho) / c \end{pmatrix} a_k \frac{\partial q}{\partial x_k} \quad (76)$$

with analogous results obtained by replacing a with a^{N_1} and a^{N_2} . This result is considerably simplified upon imposing on it the conditions that its continuity and energy components satisfy the acoustic-field results (59) and that its momentum components satisfy results (62) and (63) on the basis of a wave-like field approximation outlined below.

Upon imposing that (59) should also apply to (76) for vanishing Mach numbers, hence negligible flow kinetic energy, the continuity and energy components in (76) become

$$\frac{p_\rho}{c} a_k \frac{\partial \rho}{\partial x_k} + \frac{p_E}{c} a_k \frac{\partial E}{\partial x_k} = c a_k \frac{\partial \rho}{\partial x_k} , \quad \frac{(c^2 - p_\rho) p_\rho}{c p_E} a_k \frac{\partial \rho}{\partial x_k} + \frac{(c^2 - p_\rho)}{c} a_k \frac{\partial E}{\partial x_k} = c a_k \frac{\partial E}{\partial x_k} \quad (77)$$

Next, imposing that (62) and (63) should also apply to (76) under the same conditions, simplifies the momentum components in (76). For instance, the x_1 momentum component in (76) becomes

$$\begin{aligned} c a_1^2 a_k \frac{\partial m_1}{\partial x_k} + c a_1 a_2 a_k \frac{\partial m_2}{\partial x_k} + c a_1 a_3 a_k \frac{\partial m_3}{\partial x_k} = \\ c a_1^2 a_k \frac{\partial m_1}{\partial x_k} + c a_1 a_2^2 \frac{\partial m_k}{\partial x_k} + c a_1 a_3^2 \frac{\partial m_k}{\partial x_k} = c a_k \frac{\partial m_1}{\partial x_k} \end{aligned} \quad (78)$$

Analogous results are obtained for the x_2 and x_3 momentum Components, hence

$$c a_i a_j a_k \frac{\partial m_j}{\partial x_k} = c a_k \frac{\partial m_i}{\partial x_k} , \quad 1 \leq i \leq 3 \quad (79)$$

Following (62), these results are exact for wave-like acoustic fields. For non-acoustic fields, the wave-like field approximation for (78) rests upon the first term of a mean-value-theorem expansion

of a general solution $q = q(x_1, x_2, x_3, t)$. Appendix A shows that such a solution can be expressed as $q = q(\eta_1, \eta_2, \eta_3, \eta_4)$, where η_1 is expressed as in (38). A mean-value-theorem expansion of this general solution thus depends upon η_2 , η_3 , and η_4 and yields

$$q(\eta_1, \eta_2, \eta_3, \eta_4) = q(\eta_1, \tilde{\eta}_2, \tilde{\eta}_3, \tilde{\eta}_4) + \sum_{\ell=2}^4 \frac{\partial q}{\partial \eta_\ell} \Delta \eta_\ell \Bigg|_{\eta_1, \eta_2 + \theta_2(\eta_2 - \tilde{\eta}_2), \eta_3 + \theta_3(\eta_3 - \tilde{\eta}_3), \eta_4 + \theta_4(\eta_4 - \tilde{\eta}_4)}, \quad 0 \leq \theta_2, \theta_3, \theta_4 \leq 1 \quad (80)$$

where $\tilde{\eta}_2$, $\tilde{\eta}_3$, and $\tilde{\eta}_4$ are now fixed, which render $q(\eta_1, \tilde{\eta}_2, \tilde{\eta}_3, \tilde{\eta}_4)$ a wave-like function with respect to η_1 , for which (62) and (63) apply. The wave-like field approximation also rests on the recognition that the eigenvalues of the absolute acoustics matrix $|A_j^a a_j|$ achieve their maximum along the streamline direction a , as shown in Section 3, which justifies the choice $n = a$ in the expression $\eta_1 = x_j n_j - \lambda t$ for expansion (80).

Relations (77)-(78), therefore, lead to the beautifully simple acoustic-field result

$$|A_j^a a_j| a_k \frac{\partial q}{\partial x_k} = c I a_k \frac{\partial q}{\partial x_k} = c a_k \frac{\partial q}{\partial x_k} \quad (81)$$

A simplification similar to (77)-(80) is also applied to the crossflow components $|A_j^a a_j^{N_i}| a_k^{N_i} \frac{\partial q}{\partial x_k}$ and leads to the similar result

$$|A_j^a a_j^{N_i}| a_k^{N_i} \frac{\partial q}{\partial x_k} = c I a_k^{N_i} \frac{\partial q}{\partial x_k} = c a_k^{N_i} \frac{\partial q}{\partial x_k} \quad (82)$$

For the stated approximations, therefore, results (81)-(82) indicate within matrix product (76) and its crossflow counterpart the equivalence of replacing $|A_j^a a_j|$, $|A_j^a a_j^{N_1}|$, and $|A_j^a a_j^{N_2}|$ with the matrix $c I$, of which all eigenvalues approach $+c$ for vanishing Mach number. Appendix C also presents a different choice for Λ^{a+} and Λ^{a-} that makes the absolute acoustic matrices identical to $c I$ without any need for resolutions (77)-(80).

For acoustic flows and related dependent variables ρ , m_1 , m_2 , m_3 and E expressions (81)-(82), based on (74), are exact. Figure 5 in Section (7.4) then reveals that the contribution to the upstream-bias formulation associated with (82) remains significant for $M < 1.0$ only, whereas the contribution associated with (81) remains significant for $M < 0.39$ only. These computationally advantageous approximation on the acoustics upstream-bias, not on the flux divergence itself, therefore, will be used essentially in these Mach number ranges.

6 Acoustics-Convection Flux Divergence Decomposition

The acoustics-convection flux jacobian decomposition consists of components that genuinely model the physics of multi-dimensional acoustics and convection. These components combine the computational simplicity of FVS with the accuracy and stability of FDS and also feature eigenvalues with uniform algebraic sign. This formulation eliminates the unstable linear-dependence problem in steady low-Mach-number flows and satisfies by design the upstream-bias stability condition. As the Mach number increases, the formulation smoothly approaches and then becomes an upstream-bias approximation of the entire flux divergence, along one single direction.

6.1 Equivalent Decompositions

The previous sections have shown that the Euler flux divergence can be equivalently expressed as

$$\frac{\partial f_j}{\partial x_j} = \begin{cases} \left[\frac{\partial f_j^q}{\partial x_j} + \beta \frac{\partial f_j^p}{\partial x_j} \right] + \left[(1 - \beta) \frac{\partial f_j^p}{\partial x_j} \right]; \\ \bar{\alpha} (X \Lambda^{a+} X^{-1} + X \Lambda^{a-} X^{-1}) a_k \frac{\partial q}{\partial x_k} + \\ + (X_{N_1} \Lambda^{a+} X_{N_1}^{-1} + X_{N_1} \Lambda^{a-} X_{N_1}^{-1}) a_k^{N_1} \frac{\partial q}{\partial x_k} + (X_{N_2} \Lambda^{a+} X_{N_2}^{-1} + X_{N_2} \Lambda^{a-} X_{N_2}^{-1}) a_k^{N_2} \frac{\partial q}{\partial x_k} + \\ + \frac{\partial f_j^q}{\partial x_j} + (1 - \bar{\alpha}) A_j^a a_j a_k \frac{\partial q}{\partial x_k} + A_j^{nc} \frac{\partial q}{\partial x_j} \end{cases} \quad (83)$$

where the first expression is convenient for a characteristics-bias approximation within the streamline region, for high-subsonic and supersonic Mach numbers, and the second expression is convenient for a characteristics- bias approximation within the crossflow region and within the streamline region, for low subsonic Mach numbers.

For a multidimensional upstream-bias approximation throughout the flow field and for all Mach numbers, the flux divergence can thus be cast as the linear combination

$$\begin{aligned} \frac{\partial f_j}{\partial x_j} = (1 - \tilde{\alpha}) & \left\{ \left[\frac{\partial f_j^q}{\partial x_j} + \beta \frac{\partial f_j^p}{\partial x_j} \right] + \left[(1 - \beta) \frac{\partial f_j^p}{\partial x_j} \right] \right\} + \tilde{\alpha} \left\{ \bar{\alpha} (X \Lambda^{a+} X^{-1} + X \Lambda^{a-} X^{-1}) a_k \frac{\partial q}{\partial x_k} + \right. \\ & + (X_{N_1} \Lambda^{a+} X_{N_1}^{-1} + X_{N_1} \Lambda^{a-} X_{N_1}^{-1}) a_k^{N_1} \frac{\partial q}{\partial x_k} + (X_{N_2} \Lambda^{a+} X_{N_2}^{-1} + X_{N_2} \Lambda^{a-} X_{N_2}^{-1}) a_k^{N_2} \frac{\partial q}{\partial x_k} + \\ & \left. + \frac{\partial f_j^q}{\partial x_j} + (1 - \bar{\alpha}) A_j^a a_j a_k \frac{\partial q}{\partial x_k} + A_j^{nc} \frac{\partial q}{\partial x_j} \right\} \end{aligned} \quad (84)$$

with $0 \leq \bar{\alpha}, \tilde{\alpha} \leq 1$, which leads to the following acoustics-convection flux divergence decomposition

$$\begin{aligned} \frac{\partial f_j(q)}{\partial x_j} = \tilde{\alpha} \bar{\alpha} & (X \Lambda^{a+} X^{-1} + X \Lambda^{a-} X^{-1}) a_k \frac{\partial q}{\partial x_k} + \\ & + \tilde{\alpha} (X_{N_1} \Lambda^{a+} X_{N_1}^{-1} + X_{N_1} \Lambda^{a-} X_{N_1}^{-1}) a_k^{N_1} \frac{\partial q}{\partial x_k} + \tilde{\alpha} (X_{N_2} \Lambda^{a+} X_{N_2}^{-1} + X_{N_2} \Lambda^{a-} X_{N_2}^{-1}) a_k^{N_2} \frac{\partial q}{\partial x_k} + \\ & + \left[\frac{\partial f_j^q}{\partial x_j} + (1 - \tilde{\alpha} \bar{\alpha}) \beta \frac{\partial f_j^p}{\partial x_j} \right] + (1 - \tilde{\alpha} \bar{\alpha})(1 - \beta) \frac{\partial f_j^p}{\partial x_j} + \tilde{\alpha} (\bar{\alpha} - 1) \frac{\partial f_j^p}{\partial x_j} + \tilde{\alpha} (1 - \bar{\alpha}) A_j^a a_j a_k \frac{\partial q}{\partial x_k} + \tilde{\alpha} A_j^{nc} \frac{\partial q}{\partial x_j} \end{aligned} \quad (85)$$

In this decomposition, the expression $\left[\frac{\partial f_j^q}{\partial x_j} + (1 - \tilde{\alpha} \bar{\alpha}) \beta \frac{\partial f_j^p}{\partial x_j} \right]$ is counted as one term because, with reference to (48), the eigenvalues associated with this term will all keep the same sign within the streamline region, since $(1 - \tilde{\alpha} \bar{\alpha}) \beta \leq \beta$. As mentioned in Section 5.3, an upstream-bias approximation for the Euler flux divergence is developed by establishing upstream approximations only for the first 8 terms in (85). One justification for the selective upstream formulation on these terms rests on the physical acoustics and convection significance of these terms.

Since the bi-modal crossflow wave propagation region exists for all Mach numbers, the crossflow acoustic term $\tilde{\alpha} (X_{N_1} \Lambda^{a+} X_{N_1}^{-1} + X_{N_1} \Lambda^{a-} X_{N_1}^{-1}) a_k^{N_1} \frac{\partial q}{\partial x_k} + \tilde{\alpha} (X_{N_2} \Lambda^{a+} X_{N_2}^{-1} + X_{N_2} \Lambda^{a-} X_{N_2}^{-1}) a_k^{N_2} \frac{\partial q}{\partial x_k}$ has to receive a bi-modal upstream bias. The function $\tilde{\alpha}$ will decrease for increasing M , because the

bi-modal crossflow region shrinks for increasing Mach number. For supersonic flows, the flux divergence $\left[\frac{\partial f_j^q}{\partial x_j} + \frac{\partial f_j^p}{\partial x_j} \right]$ can be upstreamed in its entirety along a streamline, which implies that the weight $(1 - \tilde{\alpha}\bar{\alpha})\beta$ must approach 1, as M increases toward $M > 1$, while $0 \leq \tilde{\alpha}, \bar{\alpha}, \beta \leq 1$ simultaneously. On the other hand, the weight $\tilde{\alpha}$ controls the magnitude of crossflow upstream bias, which does not have to vanish for supersonic flows, because of the presence of the finite bi-modal wave-propagation regions. Hence, $\tilde{\alpha}$ does not have to approach 0 for these flows, which implies that $(1 - \tilde{\alpha})$ remains less than 1 for finite $M > 1$. As a consequence, the contribution $(1 - \tilde{\alpha}\bar{\alpha})\beta \frac{\partial f_j^p}{\partial x_j}$ is the only correct pressure-gradient fraction within (85) that should be streamline upstreamed for subsonic flows, so that as M increases the pressure-gradient weight $(1 - \tilde{\alpha}\bar{\alpha})\beta$ can smoothly and uniformly approach 1, with $0 \leq \tilde{\alpha}, \bar{\alpha}, \beta \leq 1$.

For any magnitude of both pressure and pressure gradient, the convection field uniformly carries information along streamlines; hence, $\frac{\partial f_j^q}{\partial x_j}$ can receive an upstream bias in its entirety for any M . The matrices $X\Lambda^{a+}X^{-1}$ and $X\Lambda^{a-}X^{-1}$ account for the streamline bi-modal propagation of acoustic waves; these matrices are thus used for an acoustics upstream-bias approximation within the streamline region, for low Mach numbers. As the Mach number increases from zero, therefore, a smaller and smaller fraction $\tilde{\alpha}\bar{\alpha}(X\Lambda^{a+}X^{-1} + X\Lambda^{a-}X^{-1})$ of $(X\Lambda^{a+}X^{-1} + X\Lambda^{a-}X^{-1})$ is upstream approximated, which implies that $\tilde{\alpha}\bar{\alpha}$ approaches 0 for increasing M , and $\tilde{\alpha}\bar{\alpha} \equiv 0$ for $M > 1$. The pressure gradient $\frac{\partial f_j^p}{\partial x_j}$ too accounts for the bi-modal propagation of acoustic waves, but in conjunction with $\frac{\partial f_j^q}{\partial x_j}$. As the Mach number increases from zero, a larger and larger fraction $(1 - \tilde{\alpha}\bar{\alpha})\beta \frac{\partial f_j^p}{\partial x_j}$ of the pressure gradient can thus be upstreamed in the same direction as and along with $\frac{\partial f_j^q}{\partial x_j}$, while $(1 - \tilde{\alpha}\bar{\alpha})(1 - \beta) \frac{\partial f_j^p}{\partial x_j}$ is upstreamed in the opposite direction. Hence, the function β has to increase for increasing Mach number. It follows, therefore, that the upstream-bias functions $\tilde{\alpha}$, $\bar{\alpha}$ and β have to depend upon M and ensure physical significance of the overall upstream-bias approximation to (85). These functions are then cast through the expressions

$$\delta = (1 - \tilde{\alpha}\bar{\alpha})(2\beta - 1) , \quad \alpha = \tilde{\alpha}\bar{\alpha} , \quad \alpha^N = \tilde{\alpha} \quad (86)$$

These substitutions in terms of the functions α , α^N and δ lead to significantly simpler expressions for the characteristics flux.

6.2 Multidimensional Characteristics Euler Flux

With reference to (19), given the physical significance of the terms in decomposition (85) and algebraic signs of the corresponding eigenvalues, the associated principal direction unit vectors for these terms are

$$\mathbf{a}_1 = -\mathbf{a}_2 = \mathbf{a}_7 = -\mathbf{a}_8 = \mathbf{a} , \quad \mathbf{a}_3 = -\mathbf{a}_4 = \mathbf{a}^{N_1} , \quad \mathbf{a}_5 = -\mathbf{a}_6 = \mathbf{a}^{N_2} , \quad \mathbf{a}_9 = \mathbf{a}_{10} = \mathbf{a}_{11} = \mathbf{0} \quad (87)$$

At each flow-field point, \mathbf{a} is parallel to the local velocity vector, whereas \mathbf{a}^{N_1} and \mathbf{a}^{N_2} remain orthogonal to velocity.

With (85), (87) and approximations (81)- (82), the general upstream-bias expression (19) directly yields the acoustics-convection characteristics flux divergence

$$\frac{\partial f_j^C}{\partial x_j} = \frac{\partial f_j}{\partial x_j} - \frac{\partial}{\partial x_i} \left[\varepsilon \psi \left(c \left(\alpha a_i a_j + \alpha^N \left(a_i^{N_1} a_j^{N_1} + a_i^{N_2} a_j^{N_2} \right) \right) \frac{\partial q}{\partial x_j} + a_i \frac{\partial f_j^q}{\partial x_j} + a_i \delta \frac{\partial f_j^p}{\partial x_j} \right) \right] \quad (88)$$

In this result, the expressions $\left(c \alpha a_i a_j \frac{\partial q}{\partial x_j} + a_i \frac{\partial f_j^q}{\partial x_j} + a_i \delta \frac{\partial f_j^p}{\partial x_j} \right)$ and $\left(c \alpha^N \left(a_i^{N_1} a_j^{N_1} + a_i^{N_2} a_j^{N_2} \right) \frac{\partial q}{\partial x_j} \right)$ determine the upstream biases within respectively the streamline and crossflow wave propagation

regions. These two expressions combined then induce a correct upwind bias along all wave propagation regions. In particular, the coupling of an upstream approximation for $(1 - \alpha)\beta \frac{\partial f_j^p}{\partial x_j}$, via \mathbf{a}_7 , with a downstream approximation for $(1 - \alpha)(1 - \beta) \frac{\partial f_j^p}{\partial x_j}$, via \mathbf{a}_8 results in an overall upstream approximation of the pressure gradient, but with variable weight δ . The operation count for expression (88) is then comparable to that of an FVS formulation. The terms in this expression, furthermore, directly correspond to the physics of acoustics and convection. Expression (88) determines f_i^C itself, up to an arbitrary divergence-free vector, as

$$f_i^C = f_i(q) - \varepsilon\psi \left[c \left(\alpha a_i a_j + \alpha^N \left(a_i^{N_1} a_j^{N_1} + a_i^{N_2} a_j^{N_2} \right) \right) \frac{\partial q}{\partial x_j} + a_i \frac{\partial f_j^q}{\partial x_j} + a_i \delta \frac{\partial f_j^p}{\partial x_j} \right] \quad (89)$$

According to this result, the intrinsic multi-dimensionality of each component f_i^C derives from its dependence upon the entire divergence of f_j^q and f_j^p .

For vanishing Mach numbers, α and α^N will approach 1 whereas δ will approach 0. Under these conditions, (88) reduces to

$$\frac{\partial f_j^C}{\partial x_j} = \frac{\partial f_j}{\partial x_j} - \frac{\partial}{\partial x_i} \left[\varepsilon\psi \left(c \frac{\partial q}{\partial x_i} + a_i \frac{\partial f_j^q}{\partial x_j} \right) \right] \quad (90)$$

which essentially induces only an acoustics upstream bias. Heed that this bias becomes independent of specific propagation directions, for it no longer depends on $(\alpha a_i a_j + \alpha^N (a_i^{N_1} a_j^{N_1} + a_i^{N_2} a_j^{N_2}))$. This bias, therefore, becomes isotropic, in harmony with the isotropic propagation of acoustic waves. Observe, moreover, that the components within $\partial f_j^C / \partial x_j$ remain linearly independent of one another, which avoids the linear-dependence instability in the steady low-Mach-number Euler equations. For supersonic flows, $\alpha = 0$ and $\delta = 1$ and (88) thus becomes

$$\frac{\partial f_j^C}{\partial x_j} = \frac{\partial f_j}{\partial x_j} - \frac{\partial}{\partial x_i} \left[\varepsilon\psi \left(c \alpha^N (a_i^{N_1} a_j^{N_1} + a_i^{N_2} a_j^{N_2}) \frac{\partial q}{\partial x_j} + a_i \frac{\partial f_j}{\partial x_j} \right) \right] \quad (91)$$

which depends on the crossflow component of the absolute acoustics matrix and the entire divergence of the Euler inviscid flux vector.

7 Infinite Directional Upstream Bias

In jacobian form, expression (88) becomes

$$\frac{\partial f_j^C}{\partial x_j} = \frac{\partial f_j}{\partial x_j} - \frac{\partial}{\partial x_i} \left[\varepsilon\psi \left(c \left(\alpha a_i a_j + \alpha^N \left(a_i^{N_1} a_j^{N_1} + a_i^{N_2} a_j^{N_2} \right) \right) I + a_i \frac{\partial f_j^q}{\partial q} + a_i \delta \frac{\partial f_j^p}{\partial q} \right) \frac{\partial q}{\partial x_j} \right] \quad (92)$$

Expressions (88), (92) essentially depend upon the six upstream-bias functions $a_1, a_2, a_3, \alpha, \delta, \alpha^N$, considering that \mathbf{a}^{N_1} and \mathbf{a}^{N_2} are obtained from \mathbf{a} as shown in Section 7.4. In order to ensure physical significance for the characteristics flux (89), hence for the upstream-bias approximation to decomposition (85), these functions are determined by imposing on (92) the stringent stability requirement that it should induce an upstream-bias diffusion not just along the principal streamline and crossflow upstream directions, but along all directions $\mathbf{n} = (n_1, n_2, n_3)$ radiating from any flow-field point. Appendix D shows that this demanding stability conditions is satisfied when all the eigenvalues of the associated upstream-bias matrix

$$\mathcal{A} \equiv n_i \left(c \left(\alpha a_i a_j + \alpha^N \left(a_i^{N_1} a_j^{N_1} + a_i^{N_2} a_j^{N_2} \right) \right) I + a_i \frac{\partial f_j^q}{\partial q} + a_i \delta \frac{\partial f_j^p}{\partial q} \right) n_j \quad (93)$$

remain positive for all M and propagation directions \mathbf{n} .

Despite the formidable non-linear algebraic complexity of \mathcal{A} , all of its eigenvalues have been analytically determined exactly in closed form. Dividing through by the speed of sound c , the non-dimensional form of these eigenvalues is

$$\begin{aligned}\lambda_{0,2} &= n_i \left(\alpha a_i a_j + \alpha^N \left(a_i^{N_1} a_j^{N_1} + a_i^{N_2} a_j^{N_2} \right) \right) n_j + n_i a_i v_j n_j M \\ \lambda_{3,4} &= n_i \left(\alpha a_i a_j + \alpha^N \left(a_i^{N_1} a_j^{N_1} + a_i^{N_2} a_j^{N_2} \right) \right) n_j + \\ &+ n_i a_i \left(1 + \frac{1-\delta}{2} p_E \right) v_j n_j M \pm n_i a_i \sqrt{\left(\frac{1-\delta}{2} p_E v_j n_j M \right)^2 + \delta}\end{aligned}\quad (94)$$

where v_j denotes the j^{th} direction cosine of a unit vector \mathbf{v} parallel to the local velocity \mathbf{u} . Following the considerations after (82), in particular, all these eigenvalues must converge to 1 for vanishing Mach number. Heed that for both $\mathbf{a} = \mathbf{v}$ and $\mathbf{n} = \mathbf{v}$, the functions α and δ within (94) determine the corresponding streamline upstream-bias eigenvalues

$$\lambda_{0,2} = \alpha + M \quad , \quad \lambda_{3,4} = \alpha + \left(1 + \frac{1-\delta}{2} p_E \right) M \pm \sqrt{\left(\frac{1-\delta}{2} p_E M \right)^2 + \delta} \quad (95)$$

Rather than prescribing some expressions for α and δ and accepting the resulting variations for these eigenvalues, physically consistent expressions for the streamline upstream-bias eigenvalues are instead prescribed and the corresponding functions for α and δ determined.

7.1 Conditions on Upstream-Bias Functions and Eigenvalues

The eigenvalues (94) are expressed as

$$\lambda_{0,4} = \lambda_{0,4}(M, \mathbf{n}) \quad (96)$$

to stress their dependence upon both M and \mathbf{n} . The six conditions for the determination of the six functions $a_1, a_2, a_3, \alpha, \delta, \alpha^N$ are

$$a_1^2 + a_2^2 + a_3^2 = 1 \quad , \quad \lambda_{0,2}(M, \mathbf{n}) \geq 0 \quad , \quad \lambda_{0,1}(M, \mathbf{v}) = \lambda_1 \quad , \quad \lambda_4(M, \mathbf{v}) = \lambda_4 \quad , \quad \lambda_{3,4}(M, \mathbf{n}) \geq 0 \quad (97)$$

where λ_1 and λ_4 now denote prescribed streamline upstream-bias eigenvalues. The first condition stipulates \mathbf{a} as a unit vector and with the second condition it determines \mathbf{a} , \mathbf{a}^{N_1} , and \mathbf{a}^{N_2} , for \mathbf{a} , \mathbf{a}^{N_1} , and \mathbf{a}^{N_2} are mutually perpendicular to one another. In particular, these two conditions theoretically confirm that the unit vector \mathbf{a} has to point in the streamline direction, which implies that \mathbf{a}^{N_1} , and \mathbf{a}^{N_2} have to point in any two mutually perpendicular crossflow directions. The third, fourth, and fifth conditions stipulate that the streamline upstream-bias eigenvalues must equal prescribed eigenvalues, and thereby determine α and δ . For the determined \mathbf{a} , \mathbf{a}^{N_1} , \mathbf{a}^{N_2} , α , and δ , the sixth condition then establishes α^N .

7.2 Streamline Eigenvalue λ_4

This eigenvalue will correlate with the absolute Euler eigenvalue $|M - 1|$. As a consequence, λ_4 will vary between 1 and $1 - M$ for $0 \leq M \leq 1 - \varepsilon_M$ and smoothly shift from $1 - M$ to $M - 1$ within the sonic transition layer $1 - \varepsilon_M \leq M \leq 1 + \varepsilon_M$, where ε_M denotes a transition-layer parameter;

in this work $\varepsilon_M = \frac{1}{5}$. One expression for λ_4 that remains smooth and meets these requirements is the composite spline

$$\lambda_4(M) \equiv \begin{cases} 1 - M & , \quad 0 \leq M \leq 1 - \varepsilon_M \\ \frac{(M-1)^2}{2\varepsilon_M} + \frac{\varepsilon_M}{2} & , \quad 1 - \varepsilon_M < M < 1 + \varepsilon_M \\ M - 1 & , \quad 1 + \varepsilon_M \leq M \end{cases} \quad (98)$$

7.3 Streamline Eigenvalue λ_1

This eigenvalue correlates with the non-dimensional Euler eigenvalue M , but it too has to equal 1 for $M = 0$; it then must coincide with M for $M > 1$ and also remain greater than λ_4 , as expressed through (98), for consistency with the Euler eigenvalues (42). This condition in particular implies $\lambda_1 \geq \frac{1}{2}$. It thus follows that λ_1 will vary between 1 and M for $0 \leq M \leq \frac{1}{2} + \varepsilon_M$. An expression for $\lambda_1 = \lambda_1(M)$ that remains smooth and meets all of these requirements is the composite spline

$$\lambda_1(M) \equiv \begin{cases} 1 - M & , \quad 0 \leq M \leq \frac{1}{2} - \varepsilon_M \\ \frac{(M - \frac{1}{2})^2}{2\varepsilon_M} + \frac{1 + \varepsilon_M}{2} & , \quad \frac{1}{2} - \varepsilon_M < M < \frac{1}{2} + \varepsilon_M \\ M & , \quad \frac{1}{2} + \varepsilon_M \leq M \end{cases} \quad (99)$$

7.4 Upstream-Bias Functions \mathbf{a} , \mathbf{a}^{N1} , \mathbf{a}^{N2} , $\boldsymbol{\alpha}$, $\boldsymbol{\delta}$ and $\boldsymbol{\alpha}^N$

These functions are used in actual computations based on the characteristics flux divergence (88). In the eigenvalues $\lambda_{0,2}$ in (94), the components

$$n_i \alpha a_i a_j n_j = \alpha (a_j n_j)^2 \quad , \quad n_i \alpha^N a_i^{N1} a_j^{N1} n_j = \alpha^{N1} (a_j^{N1} n_j)^2 \quad , \quad n_i \alpha^N a_i^{N2} a_j^{N2} n_j = \alpha^{N2} (a_j^{N2} n_j)^2 \quad (100)$$

are already non-negative for non-negative α and α^N . The eigenvalues $\lambda_{0,2}$, therefore, will remain non-negative for all positive α and α^N , including $\alpha \rightarrow 0$ and $\alpha^N \rightarrow 0$, when the additional component $n_i a_i v_j n_j M$ remains non-negative for all M . This requirement is met along with the first condition in (97) when $\mathbf{a} = \mathbf{v}$, for

$$n_i a_i v_j n_j M = M (v_j n_j)^2 \geq 0 \quad (101)$$

This finding is not surprising, for the streamline direction is a (principal) characteristic direction. In any flow region where velocity vanishes, it is then computationally convenient to set $a_1 = 1$, $a_2 = a_3 = 0$. The components of \mathbf{a} , \mathbf{a}^{N1} , \mathbf{a}^{N2} can thus be expressed as

$$\begin{aligned} a_1 &= \frac{u_1}{\|u\|} \quad , \quad a_2 = \frac{u_2}{\|u\|} \quad , \quad a_3 = \frac{u_3}{\|u\|} \\ a_1^{N1} &= -\frac{a_2}{\sqrt{a_1^2 + a_2^2}} \quad , \quad a_2^{N1} = \frac{a_1}{\sqrt{a_1^2 + a_2^2}} \quad , \quad a_3^{N1} = 0 \\ a_1^{N2} &= -\frac{a_1 a_3}{\sqrt{a_1^2 + a_2^2}} \quad , \quad a_2^{N2} = -\frac{a_2 a_3}{\sqrt{a_1^2 + a_2^2}} \quad , \quad a_3^{N2} = \sqrt{a_1^2 + a_2^2} \end{aligned} \quad (102)$$

It is straightforward to verify that with these expressions, \mathbf{a} , \mathbf{a}^{N_1} , and \mathbf{a}^{N_2} are unit vectors that remain mutually perpendicular with respect to one another.

From λ_1 and λ_4 in (95), the corresponding expressions for both $\alpha = \alpha(M)$ and $\delta = \delta(M)$ are then directly and exactly determined as

$$\alpha(M) = \lambda_1(M) - M, \quad \delta(M) = \frac{(\lambda_1(M) - \lambda_4(M))(\lambda_1(M) - \lambda_4(M) + p_E M)}{1 + p_E M (\lambda_1(M) - \lambda_4(M))} \quad (103)$$

where according to the fourth and fifth conditions in (97) the streamline eigenvalues λ_4 and λ_1 are respectively given by (98), (99).

Appendix E shows that the sixth condition in (97) leads to the following expression for α^N

$$\alpha^N(M) \equiv \begin{cases} 1 + \left(\frac{3(\alpha^N(M_M) - 1)}{M_M^2} - \frac{\alpha^{N'}(M_M)}{M_M} \right) M^2 + \left(\frac{\alpha^{N'}(M_M)}{M_M^2} - \frac{2(\alpha^N(M_M) - 1)}{M_M^3} \right) M^3, & 0 \leq M < M_M; \\ \frac{1}{2} \left(1 + \frac{\varepsilon_M}{M_M - \sqrt{M_M^2 - 1}} \right) (M - \sqrt{M^2 - 1}), & M_M \leq M \end{cases} \quad (104)$$

where superscript prime “'” denotes differentiation with respect to M .

The variations of $\alpha = \alpha(M)$, $\alpha^N = \alpha^N(M)$ and $\delta = \delta(M)$ in Figure 5 indicate that these three

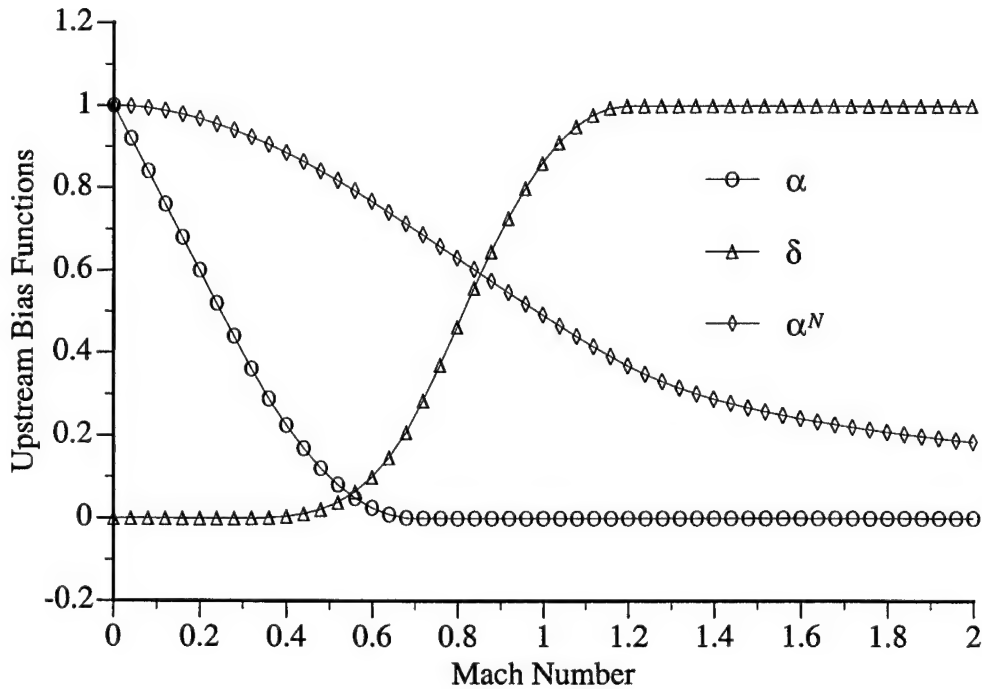


Figure 5: Upstream-Bias Functions

functions as well as their slopes remain continuous for all Mach numbers, with $0 \leq \alpha, \alpha^N, \delta \leq 1$ and $\alpha \equiv 0$ for $M > \frac{1}{2} + \varepsilon_M$, $\delta \equiv 0$ for $M \leq 0.3$, and $\delta \equiv 1$ for $M > 1 + \varepsilon_M$. The variation of $\delta = \delta(M)$ shows that the pressure-gradient contribution to this upstream-bias formulation increases monotonically, while remaining less than 25% of its maximum, for $0 \leq M \leq 0.7$. As $\delta = \delta(M)$ rises, the effect of the acoustic-flow result (81) is concurrently reduced, because the streamline

upstream-bias α contribution from the corresponding acoustics matrix decreases rapidly, reducing by 75% at $M = 0.39$.

The decrease of α^N , hence of the crossflow upstream-bias from (82), is less rapid because this is the only contribution to a crossflow upstream. The function α^N , nevertheless, decreases by 50%, at the sonic state, and by 80% for $M = 1.8$. For this function, forcing non-negativity of $\lambda_{3,4}$ as opposed to equality to a prescribed positive constant, in particular, ensures minimal cross flow diffusion. Expression (104) leads to the conclusions

$$\lim_{M \rightarrow \infty} \alpha^N(M) = 0 \quad , \quad \lim_{M \rightarrow \infty} \frac{\partial \alpha^N}{\partial M} = 0 \quad (105)$$

which indicate that the magnitude of crossflow upstream decreases with increasing M . This result agrees with the physics of high- M flows, where the bi-modal propagation region narrows about the crossflow direction, as seen in Section 4.4. Convection thereby becomes the prevailing wave propagation mechanism, which therefore reduces the need for acoustic crossflow upstream bias.

7.5 Streamline Upstream-Bias Eigenvalues

As Figure 6 shows, the streamline upstream bias eigenvalues (95) remain positive. Furthermore,

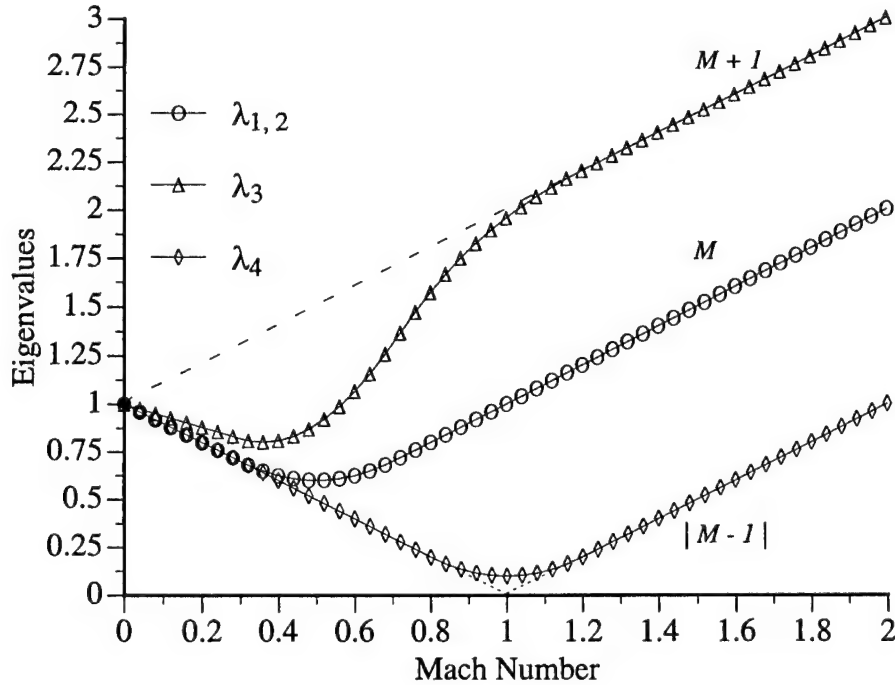


Figure 6: Upstream-Bias Eigenvalues

these eigenvalues and their slopes remain continuous for all Mach numbers. For $0 \leq M \leq 1 + \varepsilon_M$, the eigenvalues $\lambda_{0,2}$, λ_3 , λ_4 smoothly approach 1 for vanishing M , indicating a physically consistent upstream-bias approximation of the acoustic equations (56) embedded within the Euler equations. For $M > 1 + \varepsilon_M$, these eigenvalues respectively coincide with the Euler flux jacobian streamline eigenvalues M , $M + 1$, $M - 1$, which corresponds to a streamline upstream-bias approximation of the entire flux vector, for supersonic flows. Observe also the smooth transition in the critical sonic region within the transition layer, where λ_4 does not vanish, but remains not less than $\varepsilon_M/2$.

7.6 Polar Variation of Upstream-Bias

The directional variation of the upstream bias eigenvalues (94) is presented in Figures 7 - 8 for representative subsonic and supersonic Mach numbers. These variations are obtained for a variable unit vector $\mathbf{n} \equiv (\cos \theta, \sin \theta)$ and fixed unit vector $\mathbf{a} = \mathbf{v}$, in this representative case inclined by $+30^\circ$ with respect to an x_1 axis on any plane Π that contains the velocity vector.

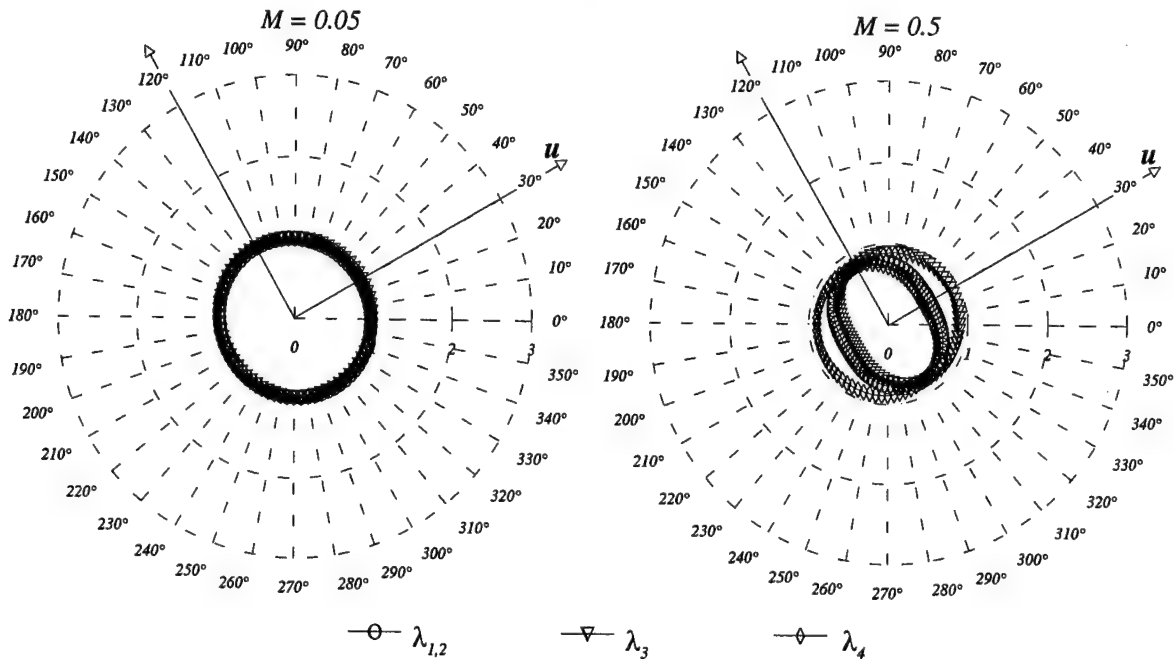


Figure 7: Polar Variation of Subsonic Upstream Bias

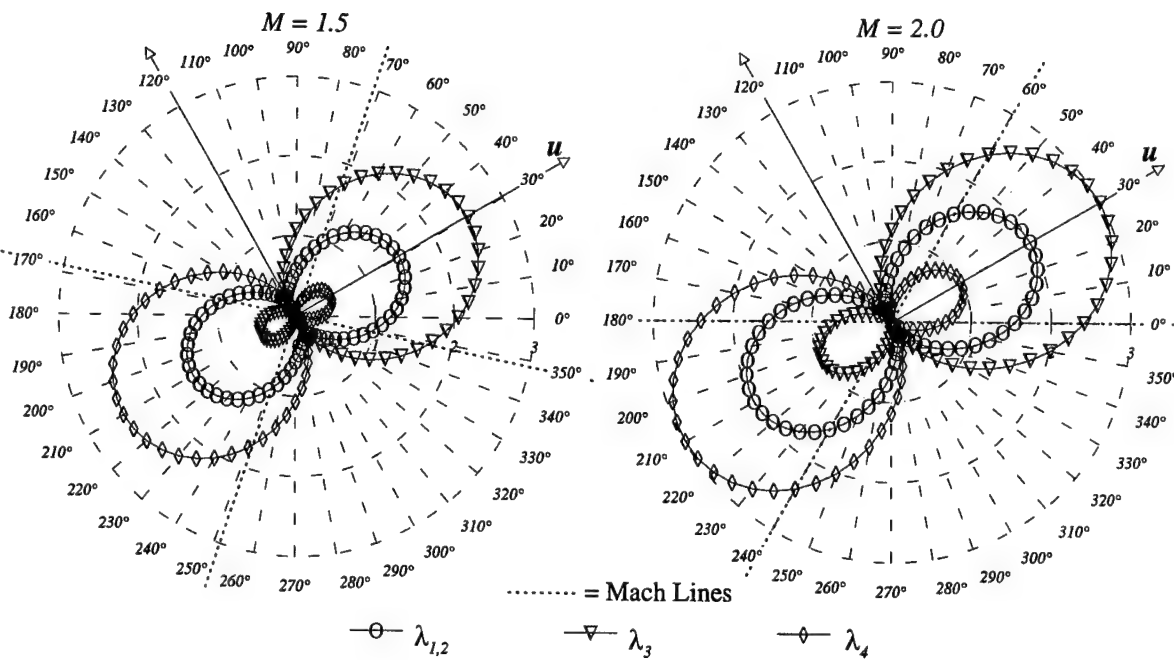


Figure 8: Polar Variation of Supersonic Upstream Bias

These figures collectively indicate that the characteristics flux divergence (88) induces a physically consistent upstream bias because, for any Mach number and wave propagation direction n , the associated upstream-bias eigenvalues (94) remain positive and their directional variation mirrors the directional variation of the characteristic Euler eigenvalues (42). The upstream-bias eigenvalues, moreover, are symmetrical about the crossflow direction and characteristic streamline, precisely like the characteristic Euler eigenvalues (10). For $M = 0.05$, the directional variation of the upstream-bias eigenvalues in Figure 7 correlates with that in Figure 1 and thereby corresponds to an isotropic upstream bias, in complete agreement with the isotropic acoustic wave propagation speed in the Euler equations. For increasing Mach numbers, the upstream bias becomes anisotropic, again in agreement with the anisotropic distribution of the Euler eigenvalues (42). For $M = 0.5$ this anisotropy is already evident and then becomes more marked for supersonic Mach numbers as indicated in Figure 8. In particular, the crossflow upstream bias decreases for increasing Mach number.

Figures 9 - 10 compare the directional variations of the representative upstream-bias eigenvalue λ_3 and the corresponding Euler eigenvalue λ_3^E . This comparison is sufficient to depict the correlation between all the Euler and upstream-bias eigenvalues, for $\lambda_{0,2}$ and $\lambda_{0,2}^E$ are topologically similar to each other, compare Figures 2 and 8, while λ_4 and λ_4^E are respectively mirror skew-symmetric to λ_3 and λ_3^E with respect to the crossflow direction.

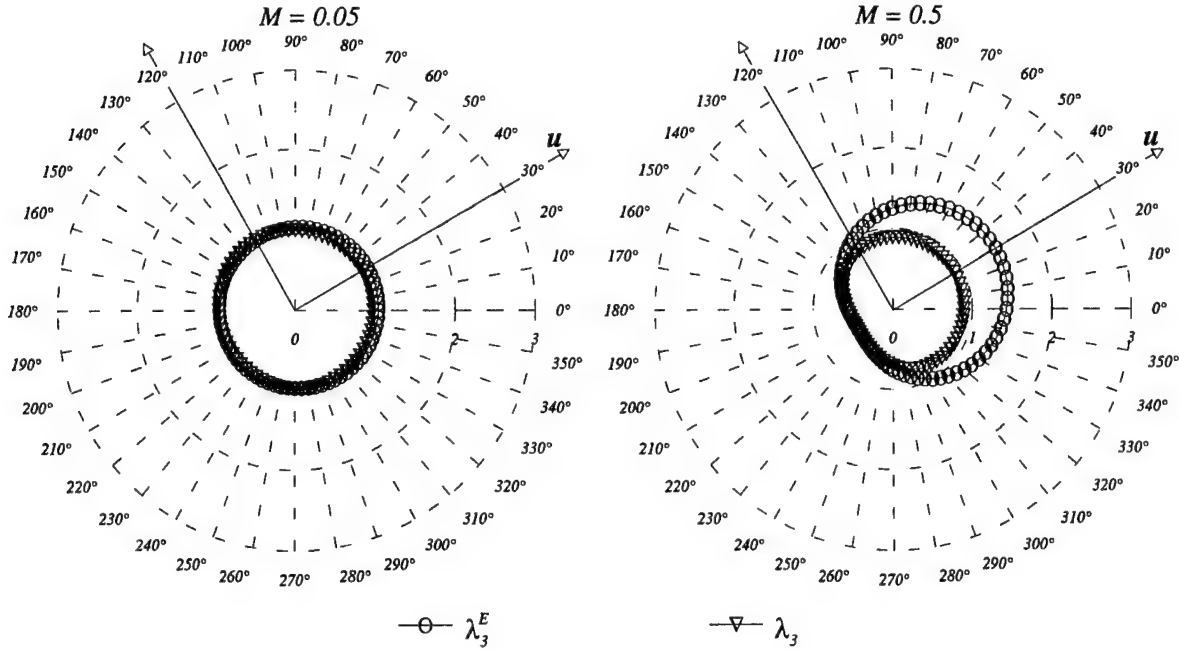


Figure 9: Polar Correlation of Subsonic Characteristic λ_3^E and Upstream λ_3

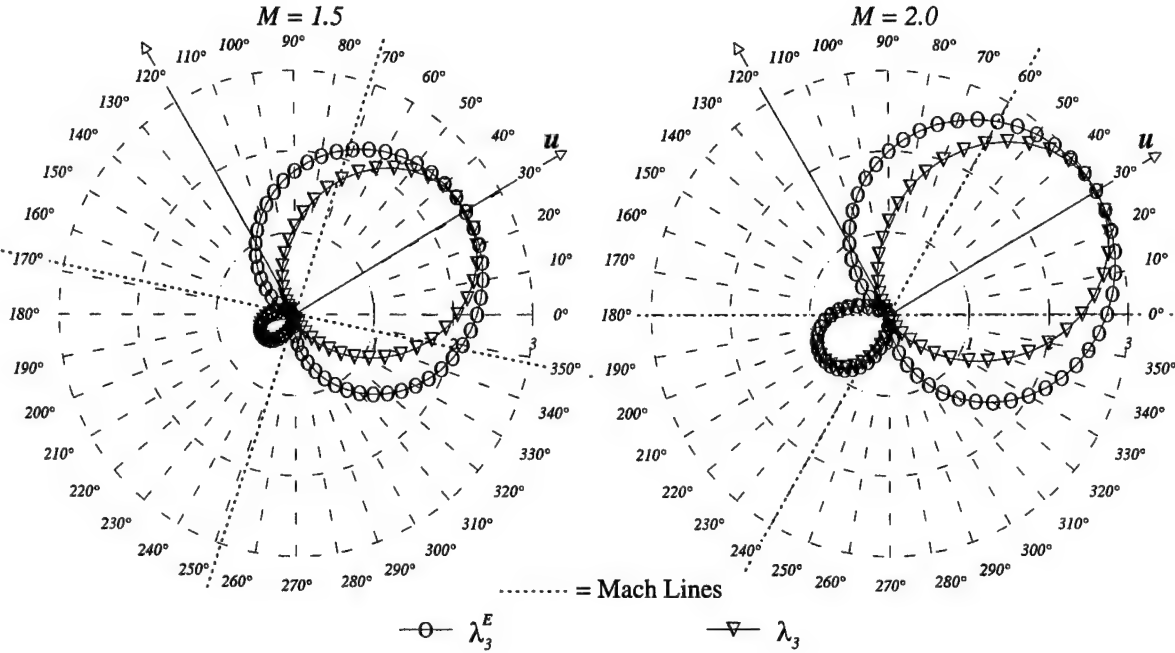


Figure 10: Polar Correlation of Supersonic Characteristic λ_3^E and Upstream λ_3

As Figures 9 - 10 indicate, λ_3 is symmetrical about the characteristic streamline, precisely like the corresponding characteristic Euler eigenvalue λ_3^E and the corresponding polar curve is topologically similar to the Euler eigenvalue curve. For $M = 0.05$, λ_3 and λ_3^E virtually coincide with each other and remain direction invariant, which corresponds to an isotropic upstream bias in correlation with the acoustic speed. For $M = 0.5$, Figure 9 indicates that λ_3^E is greater than λ_3 in the streamline direction. This results corresponds to minimal streamline upstream diffusion and is explained in terms of Figure 6, which shows λ_3 in the streamline direction as substantially less than $M + 1$, for this Mach number.

For supersonic Mach numbers, λ_3 in the streamline direction coincides with $M + 1$. As shown in Figure 10, therefore, the magnitude of the upstream bias for supersonic flows is virtually identical to the magnitude of the characteristic eigenvalues, within the domain of dependence and range of influence of any flow field point. Outside this region, the upstream-bias eigenvalues are modestly less than the characteristic eigenvalues. In these variations, the upstream-bias eigenvalues are vanishingly small in the cross-flow direction, which, in particular, corresponds to minimal crossflow diffusion.

8 Finite Element Weak Statement

The divergence (88) of the characteristics flux f_j^C leads to the following characteristics-bias integral statement with implied summation on repeated subscript indices i, j

$$\begin{aligned}
 & \int_{\Omega} w \left[\frac{\partial q}{\partial t} + \frac{\partial f_j}{\partial x_j} - \frac{\partial f_j^v}{\partial x_j} \right] d\Omega \\
 & - \int_{\Omega} w \left[\frac{\partial}{\partial x_i} \left(\varepsilon \psi \left(c \left(\alpha a_i a_j + \alpha^N \left(a_i^{N_1} a_j^{N_1} + a_i^{N_2} a_j^{N_2} \right) \right) \frac{\partial q}{\partial x_j} + a_i \frac{\partial f_j^q}{\partial x_j} + a_i \delta \frac{\partial f_j^p}{\partial x_j} \right) \right) \right] d\Omega = 0
 \end{aligned} \tag{106}$$

An integration by parts of the characteristics-bias expression then generates the weak statement

$$\begin{aligned}
 & \int_{\Omega} w \left[\frac{\partial q}{\partial t} + \frac{\partial f_j}{\partial x_j} - \frac{\partial f_j^v}{\partial x_j} \right] d\Omega \\
 & + \int_{\Omega} \left[\frac{\partial w}{\partial x_i} \varepsilon \psi \left(c \left(\alpha a_i a_j + \alpha^N \left(a_i^{N_1} a_j^{N_1} + a_i^{N_2} a_j^{N_2} \right) \right) \frac{\partial q}{\partial x_j} + a_i \frac{\partial f_j^q}{\partial x_j} + a_i \delta \frac{\partial f_j^p}{\partial x_j} \right) \right] d\Omega - \\
 & \oint_{\partial\Omega} w \varepsilon \psi \left(c \left(\alpha \mathbf{a} \cdot \mathbf{n} a_j + \alpha^N \left(\mathbf{a}^{N_1} \cdot \mathbf{n} a_j^{N_1} + \mathbf{a}^{N_2} \cdot \mathbf{n} a_j^{N_2} \right) \right) \frac{\partial q}{\partial x_j} + \mathbf{a} \cdot \mathbf{n} a_j \frac{\partial f_j^q}{\partial x_j} + \mathbf{a} \cdot \mathbf{n} a_j \delta \frac{\partial f_j^p}{\partial x_j} \right) d\Gamma = 0
 \end{aligned} \tag{107}$$

where \mathbf{n} denotes the outward pointing unit vector orthogonal to the boundary $\partial\Omega$ of Ω .

8.1 Elimination of Spurious Upstream Boundary Dissipation

On any boundary facet where $w \neq 0$, expression (107) would induce spurious upstream boundary dissipation if the boundary integral were not evaluated. It is possible, however, to eliminate both this surface integral and any spurious upstream boundary dissipation. This result is achieved by setting \mathbf{a} , \mathbf{a}^{N_1} , and \mathbf{a}^{N_2} , within every finite element with a face on the boundary $\partial\Omega$, equal to unit vectors that are orthogonal to \mathbf{n} . One choice is

$$(\mathbf{a})_{\partial\Omega} = \mathbf{a} - \mathbf{a} \cdot \mathbf{n} \mathbf{n}, \quad (\mathbf{a}^{N_1})_{\partial\Omega} = \mathbf{a}^{N_1} - \mathbf{a}^{N_1} \cdot \mathbf{n} \mathbf{n}, \quad (\mathbf{a}^{N_2})_{\partial\Omega} = \mathbf{a}^{N_2} - \mathbf{a}^{N_2} \cdot \mathbf{n} \mathbf{n} \tag{108}$$

With this choice $(\mathbf{a})_{\partial\Omega} \cdot \mathbf{n} = 0$, $(\mathbf{a}^{N_1})_{\partial\Omega} \cdot \mathbf{n} = 0$, $(\mathbf{a}^{N_2})_{\partial\Omega} \cdot \mathbf{n} = 0$, the corresponding surface integral in (107) naturally vanishes, hence no spurious upstream boundary dissipation is induced by not evaluating this integral.

8.2 Galerkin Finite Element Equations

The finite element weak statement associated with (107) is

$$\begin{aligned}
 & \int_{\Omega^h} w^h \left(\frac{\partial q^h}{\partial t} + \frac{\partial f_j^h}{\partial x_j} - \frac{\partial f_j^{vh}}{\partial x_j} \right) d\Omega + \\
 & \int_{\Omega^h} \frac{\partial w^h}{\partial x_i} \varepsilon^h \psi^h \left(c^h \left(\alpha^h a_i^h a_j^h + \alpha^{N^h} \left(a_i^{N_1^h} a_j^{N_1^h} + a_i^{N_2^h} a_j^{N_2^h} \right) \right) \frac{\partial q^h}{\partial x_j} + a_i^h \frac{\partial f_j^{q^h}}{\partial x_j} + a_i^h \delta^h \frac{\partial f_j^{p^h}}{\partial x_j} \right) d\Omega = 0
 \end{aligned} \tag{109}$$

where superscript “ h ” signifies spatial discrete approximation. The approximation q^h exists on a partition Ω^h , $\Omega^h \subseteq \Omega$, of Ω . This partition Ω^h has its boundary nodes on the boundary $\partial\Omega$ of Ω and results from the union of N_e non-overlapping elements Ω_e , $\Omega^h = \bigcup_{e=1}^{N_e} \Omega_e$. Within Ω^h , there exists a cluster of “master” elements Ω_k^M , each comprising only those adjacent elements that share a mesh node x_k , with $1 \leq k \leq N$, where N denotes the total number of mesh nodes and hence master elements.

In the representative case of a 2-D flow, as Figure 11 shows, the discrete test function w^h within each master element Ω_k^M will coincide with the “pyramid” basis function $w_k = w_k(\mathbf{x})$, $1 \leq k \leq N$, with compact support on Ω_k^M . Such a function equals one at node x_k , zero at all other mesh nodes and also identically vanishes both on the boundary segments of Ω_k^M not containing x_k and on the computational domain outside Ω_k^M .

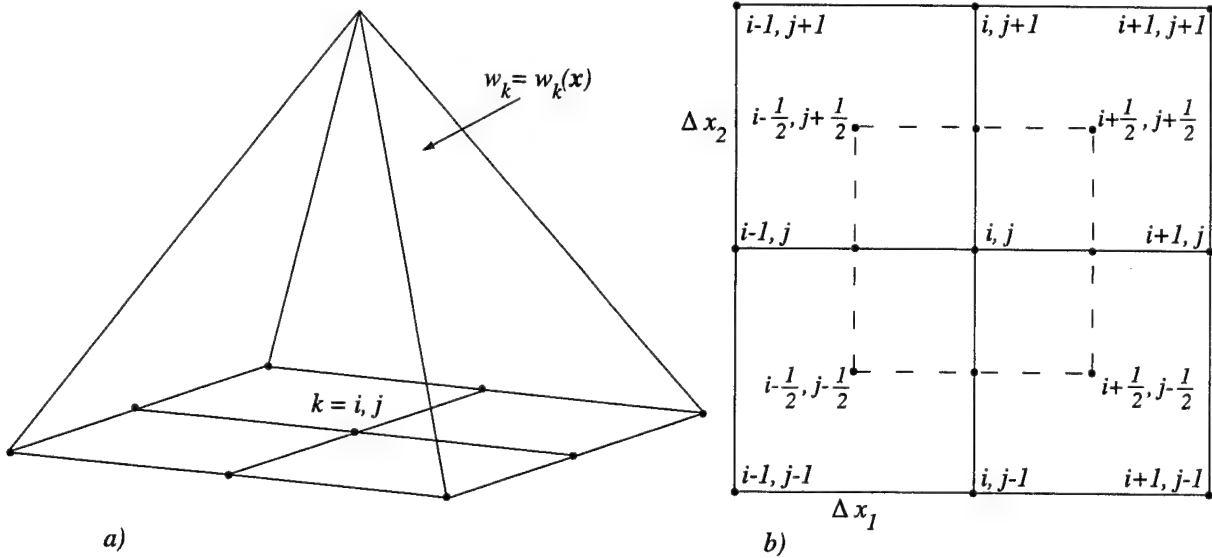


Figure 11: a) Pyramid Test Function for Ω_k^M , b) Assembly of 4 Uniform Quadrilaterals

The discrete solution q^h and flux f_j^h at each time t assume the form of the following group linear combinations

$$q^h(\mathbf{x}, t) \equiv \sum_{\ell=1}^N w_\ell(\mathbf{x}) \cdot q^h(\mathbf{x}_\ell, t) , \quad f_j^h(\mathbf{x}, t) \equiv \sum_{\ell=1}^N w_\ell(\mathbf{x}) \cdot f_j(q^h(\mathbf{x}_\ell, t)) \quad (110)$$

of time-dependent nodal solution values $q^h(\mathbf{x}_\ell, t)$, to be determined, and trial functions, which coincide with the test functions $w_\ell(\mathbf{x})$ for a Galerkin formulation. Similarly, the fluxes $f_j^q = f_j^q(q(\mathbf{x}, t))$ and $f_j^p = f_j^p(q(\mathbf{x}, t))$ are discretized through the group expressions

$$f_j^{q^h}(\mathbf{x}, t) \equiv \sum_{\ell=1}^N w_\ell(\mathbf{x}) \cdot f_j^q(q^h(\mathbf{x}_\ell, t)) , \quad f_j^{p^h}(\mathbf{x}, t) \equiv \sum_{\ell=1}^N w_\ell(\mathbf{x}) \cdot f_j^p(q^h(\mathbf{x}_\ell, t)) \quad (111)$$

with similar expansions applying for the components of the viscous flux f_j^{vh} . The notation for the discrete nodal variable and fluxes is then simplified as $q_\ell(t) \equiv q(\mathbf{x}_\ell, t)$, $f_{j_\ell} \equiv f_j(q^h(\mathbf{x}_\ell, t))$, $f_{j_\ell}^q \equiv f_j^q(q^h(\mathbf{x}_\ell, t))$, $f_{j_\ell}^p \equiv f_j^p(q^h(\mathbf{x}_\ell, t))$ and expansions (110)-(111) are then inserted into (109), which yields the discrete finite element weak statement

$$\begin{aligned} & \int_{\Omega^h} w_k \left(w_\ell \frac{dq_\ell}{dt} + \frac{\partial w_\ell}{\partial x_j} f_{j_\ell} - \frac{\partial f_j^{vh}}{\partial x_j} \right) d\Omega + \\ & + \int_{\Omega^h} \frac{\partial w_k}{\partial x_i} \frac{\partial w_\ell}{\partial x_j} \varepsilon^h \psi^h \left[c^h \left(\alpha^h a_i^h a_j^h + \alpha^{N^h} \left(a_i^{N_1^h} a_j^{N_1^h} + a_i^{N_2^h} a_j^{N_2^h} \right) \right) q_\ell + a_i^h f_{j_\ell}^q + a_i^h \delta^h f_{j_\ell}^q \right] d\Omega = 0 \end{aligned} \quad (112)$$

for $1 \leq k \leq N$. There are three implied summations with respect to the subscript indices i, j, ℓ . The subscript indices i, j in this expression denote cartesian-axis directions, hence $1 \leq i, j \leq 3$, whereas subscript ℓ indicates a mesh node, hence $1 \leq \ell \leq N$.

While an expansion like the ones in (110) for ψ^h , α^h , c^h , \mathbf{a}^h , $\mathbf{a}^{N_1^h}$, $\mathbf{a}^{N_2^h}$, and δ^h can be directly accommodated within (112), each of these variables in this study has been set equal to a piece wise constant for computational simplicity, one centroidal constant value per element. Likewise, ε^h is

set equal to a reference length within each element, typically a measure of the element size. In this study, $\varepsilon^h = (\ell)_e/2$ within each element “ e ”, Where $(\ell)_e$ denotes the length of the streamline diameter of the generalized ellipsoid inscribed within the element. The choice of a diameter in the streamline direction for $(\ell)_e$ rests on the recognition that the streamline is a characteristic principal direction, as discussed in Sections 4.2 - 4.4.

Since the test and trial functions w_ℓ are prescribed functions of \mathbf{x} , the spatial integrations in (112) are directly carried out. For arbitrarily shaped elements, these integrations take place via the usual finite element local-coordinate transformation^{22,23} that for example maps a quadrilateral into a square. In this study, the resulting coordinate- transformation metrics within each element are set to constants equal to their respective centroidal values. This simplification allows the exact integration of the remaining integrals, which are then evaluated only once for each computation. The complete integration with respect to \mathbf{x} transforms (112) into a system of continuum-time ordinary differential equations (ODE) for determining at each time level t the unknown nodal values $q^h(\mathbf{x}_\ell, t)$, $1 \leq \ell \leq N$. This ODE system is numerically integrated in time via an implicit diagonal Runge-Kutta algorithm that remains absolutely stable for stiff non-linear dissipative systems. Concerning the boundary variables, no extrapolation of variables is needed in this algorithm on a variable that is not constrained via a Dirichlet boundary condition. In this case, instead, the finite element algorithm (109) naturally generates for each unconstrained boundary variable a boundary-node ordinary differential equation.

8.3 Discrete Conservation

The finite element equations (112) naturally lead to a discretely conservative algorithm, for they can be rearranged in a traditional “numerical flux” form. When the mesh nodes of a rectangular grid of squares are numbered via integer coordinates i, j , for a representative 2-D Euler formulation, the specific numerical-flux form of the finite element system is

$$\frac{d\bar{q}_{i,j}}{dt} + \frac{F_{1_{i+\frac{1}{2},j}} - F_{1_{i-\frac{1}{2},j}}}{\Delta x_{1_{i,j}}} + \frac{F_{2_{i,j+\frac{1}{2}}} - F_{2_{i,j-\frac{1}{2}}}}{\Delta x_{2_{i,j}}} = 0 \quad (113)$$

which is analogous to the form of upwind finite-volume schemes.¹⁸ In this expression, $\bar{q}_{i,j}$ denotes the average value of the discrete q^h at node “ i, j ”. The finite element formulation directly generates this average, which for the simple representative case of a uniform cartesian mesh with constant Δx_1 and Δx_2 becomes

$$\bar{q}_{i,j} \equiv \frac{q_{i-1,j-1} + 4q_{i,j-1} + q_{i+1,j-1} + 4q_{i-1,j} + 16q_{i,j} + 4q_{i+1,j} + q_{i-1,j+1} + 4q_{i,j+1} + q_{i+1,j+1}}{36} \quad (114)$$

Likewise, the formulation directly generates the intrinsically multi-dimensional “numerical fluxes” $F_{1_{i+\frac{1}{2},j}}$ and $F_{2_{i,j+\frac{1}{2}}}$. For a uniform cartesian mesh, these fluxes are expressed as

$$\begin{aligned} F_{1_{i+\frac{1}{2},j}} &\equiv \bar{f}_{1_{i+\frac{1}{2},j}} - \overline{\left(\varepsilon \psi a_1 \frac{\Delta f_\ell^q}{\Delta x_\ell} \right)}_{i+\frac{1}{2},j} - \overline{\left(\varepsilon \psi a_1 \delta \frac{\Delta f_\ell^p}{\Delta x_\ell} \right)}_{i+\frac{1}{2},j} - \\ &\quad - \overline{\left(\varepsilon \psi c \alpha a_1 a_\ell \frac{\Delta q}{\Delta x_\ell} \right)}_{i+\frac{1}{2},j} - \overline{\left(\varepsilon \psi c \alpha^N a_1^N a_\ell^N \frac{\Delta q}{\Delta x_\ell} \right)}_{i+\frac{1}{2},j} \end{aligned} \quad (115)$$

and

$$F_{2_{i,j+\frac{1}{2}}} \equiv \bar{f}_{2_{i,j+\frac{1}{2}}} - \overline{\left(\varepsilon \psi a_2 \frac{\Delta f_\ell^q}{\Delta x_\ell} \right)}_{i,j+\frac{1}{2}} - \overline{\left(\varepsilon \psi a_2 \delta \frac{\Delta f_\ell^p}{\Delta x_\ell} \right)}_{i,j+\frac{1}{2}} -$$

$$-\overline{\left(\varepsilon\psi c\alpha a_2 a_\ell \frac{\Delta q}{\Delta x_\ell}\right)}_{i,j+\frac{1}{2}} - \overline{\left(\varepsilon\psi c\alpha^N a_2^N a_\ell^N \frac{\Delta q}{\Delta x_\ell}\right)}_{i,j+\frac{1}{2}} \quad (116)$$

where “ $\overline{(\)}$ ” denotes an average over the elements sharing node “ i, j ”. Appendix F presents the expressions for these averages. Apart from becoming the discrete counterparts of the multi-dimensional characteristics-bias flux (19), expressions (115)-(116) correspond to authentic numerical fluxes¹⁸ because they respectively reduce to $f_1(q)$ and $f_2(q)$ when each nodal value of q^h therein is replaced by q , for fixed Δx_1 and Δx_2 .

The non-negative controller ψ determines the amount of induced upstream bias in these expressions. For $\psi = 0$, no upstream bias, hence dissipation, is induced and (109)-(116) generate a centered approximation for the Euler equations. The local element length ε^h , hence $(\ell)_e$, is then chosen so that $\psi = 1$ then corresponds to a fully upwind approximation, hence maximum upstream dissipation. The numerical solution for q^h drives the local magnitude of ψ within each element¹⁷ : in flow regions where discontinuities would form then $\psi = \psi_{\max}$, for essentially non-oscillatory shock capturing, and in smooth flow regions then $\psi = \psi_{\min}$, for increased accuracy. Equations (109)-(116) induce an upstream bias in the correct direction with respect to the velocity direction because the direction cosines a_1 and a_2 of velocity \mathbf{u} determine the upstream direction. In particular, when either a_1 or a_2 vanishes, then either F_1 or F_2 becomes a centered numerical flux in the x_1 or x_2 cartesian direction, while featuring an acoustics upstream bias in the corresponding orthogonal direction, as induced by either a_2^N or a_1^N . In any case, equations (109)-(116) ultimately induce an upstream bias on the entire Euler flux divergence for any orientation of $\mathbf{a} = \mathbf{v}$.

9 Discrete Upstream-Bias Controller ψ^h

This section introduces a new upstream-bias controller ψ^h . This controller varies in the range $0 \leq \psi_{\min} \leq \psi^h \leq \psi_{\max} \leq 1$ and controls within (112) the amount of induced upstream-bias, hence artificial diffusion. By design, $\psi^h = 0$ corresponds to a classical centered discretization, hence no upwind diffusion; $\psi^h = 1$, instead, corresponds to a fully upwind formulation, hence maximum diffusion.

Denote then with ψ_i the numerical value of the controller at the representative node “ i ”, for a 1-D formulation, or at the face shared by two 2-D or 3-D elements. By analogy with (110), the discrete controller $\psi^h(s, t)$ is cast as the following linear expansion

$$\psi^h(x, t) = \sum_{j=1}^2 w_j(s) \psi(s_j, t) = \sum_{j=1}^N w_j(s) \psi_j \quad (117)$$

This is a 1-D expansion even for a 3-D flow and corresponds to the variation of $\psi^h(s, t)$ within each element with respect to the coordinate s along the arc of streamline that crosses the element centroid and intersects two faces of the element; the centroidal evaluation of this expression within each element then yields

$$\psi_{i+\frac{1}{2}} = \frac{\psi_i + \psi_{i+1}}{2} \quad (118)$$

In regions of smooth flow ψ^h approaches ψ_{\min} for a local reduction of upstream-bias diffusion; in region of discontinuous solution ψ^h approaches ψ_{\max} , for an essentially non-oscillatory resolution of local discontinuities. The controller will thus correlate with a local measure φ_i of slope discontinuity.

For a smooth variation, ψ_i is expressed as a function of the measure φ_i as the composite spline

$$\psi_i \equiv \begin{cases} \psi_{\min} & , \quad \varphi_i \leq \varphi_c \\ \psi_{\max} + \frac{\psi_{\max} - \psi_{\min}}{(\varphi_D - \varphi_c)^3} \cdot \\ \left[-(\varphi_D - 3\varphi_c)\varphi_D^2 - 6\varphi_c\varphi_D\varphi_i + 3(\varphi_D + \varphi_c)\varphi_i^2 - 2\varphi_i^3 \right] & , \quad \varphi_c < \varphi_i < \varphi_D \\ \psi_{\max} & , \quad \varphi_D \leq \varphi_i \end{cases} \quad (119)$$

where $0 \leq \varphi_i \leq 1$ and the positive φ_c and φ_D respectively denote threshold continuity and discontinuity measures. Figure 12 shows the smooth variation of this type of spline controller.

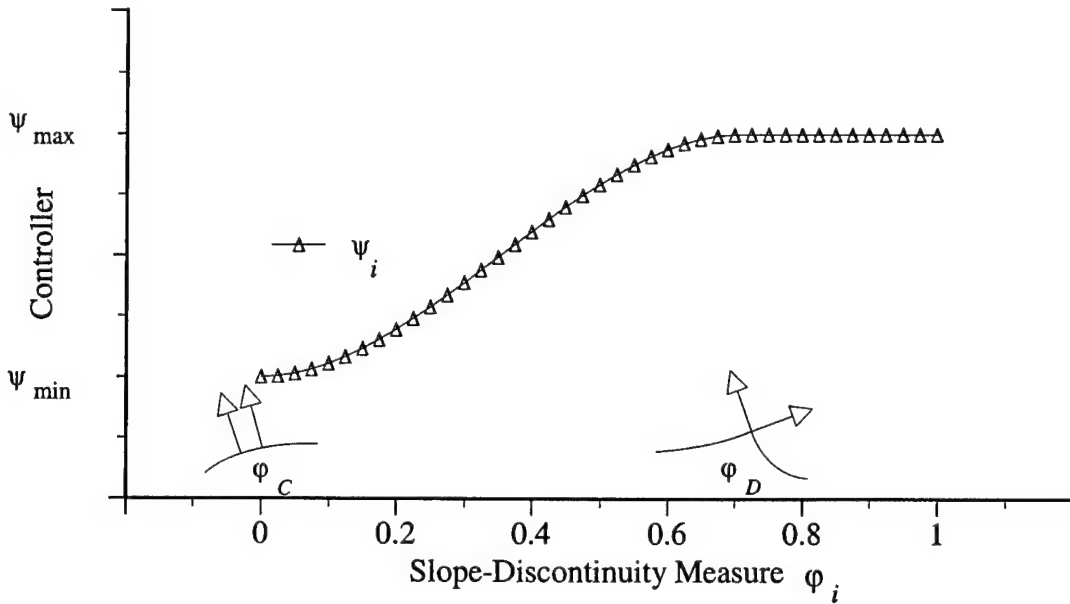


Figure 12: Variation of Controller ψ_i

The implementation of ψ^h thus requires a set of points within Ω^h where the slopes of the approximate solution are generally discontinuous. For the finite element approximation (110), this set of points is taken as the set of locations on faces shared by any two distinct elements in Ω^h , for the continuous expansion (110) changes approximating polynomial from element to element, which implies that solution slopes are generally discontinuous at element faces. This type of slope discontinuity is depicted in Figure 13 via the local normal unit vectors \mathbf{n}^L and \mathbf{n}^R respectively to the left and right of the slope-discontinuity point P , where there exist two distinct normal unit vectors, one for each of two elements sharing P . This picture refers to 1-D, 2-D and 3-D formulations. In 1-D, point P in this picture corresponds to a finite element node; in 2-D and 3-D, point P is the centroid on the face shared by any two contiguous elements and the corresponding arcs indicate the variation of q_c^h along the element centroidal streamline arc.

With reference to Figure 13, the magnitude $\|\mathbf{n}^R - \mathbf{n}^L\|$ of the vector difference $\mathbf{n}^R - \mathbf{n}^L$ becomes proportional to a bounded measure of local slope discontinuity. If the graph slope is continuous at P , then \mathbf{n}^L coincides with \mathbf{n}^R and $\|\mathbf{n}^R - \mathbf{n}^L\|$ vanishes. On the other hand, when a slope

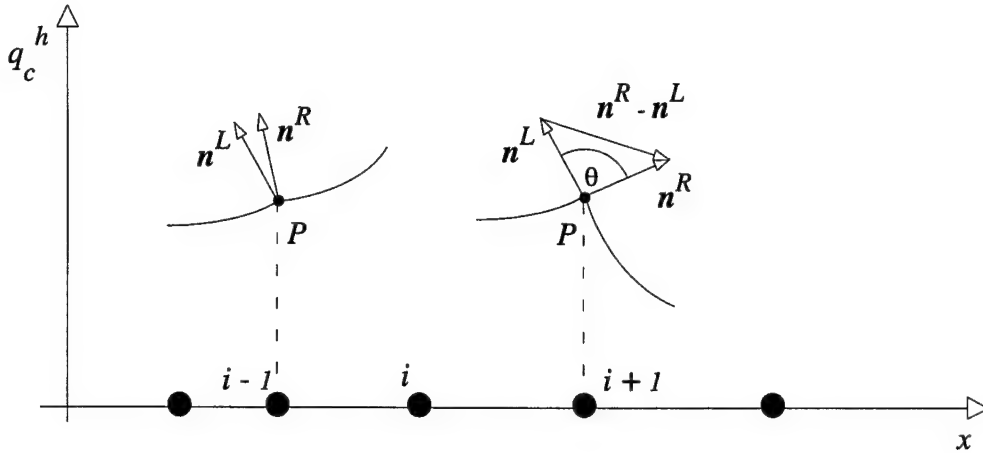


Figure 13: Slope Discontinuities and Local Unit Vectors

discontinuity exists at P , as shown in the figure, $\|n^R - n^L\|$ varies between 0 and 2 depending on the magnitude of the slope jump. A positive measure of slope discontinuity that vanishes for continuous slopes, remains bounded and strictly varies between 0 and 1 can thus be defined as

$$\varphi_i \equiv \frac{1}{2} \|n^R - n^L\|_{x=x_i} \quad (120)$$

By virtue of the law of cosines, the local measure φ_i also equals

$$\varphi_i = \left(\frac{1 - \cos \theta}{2} \right)_{x=x_i}^{\frac{1}{2}} \quad (121)$$

where θ denotes the angle between the unit vectors in Figure 13.

With reference to Figure 14 and (121), specific numerical values for φ_C , φ_D , ψ_{\min} and ψ_{\max} can be easily established. At a point of solution smoothness, like point $i-1$ in the figure, n^L will be parallel to n^R , hence $\theta = 0^\circ$ which from (121) leads to $\varphi_C = 0$. At a shock, instead, θ can become greater than 90° , as shown in the figure for point i . The threshold $\theta = 90^\circ$ is thus selected for φ_D , which from (121) leads to $\varphi_D = 1/\sqrt{2}$. Numerous numerical experiments with the acoustics-convection algorithm have indicated that a minimal amount of “background” upstream bias is necessary for convergence; this finding is not surprising, since the formulation is essentially centered, hence devoid of any upstream-bias dissipation for $\psi^h = 0$. Hence, $\psi_{\min} > 0$, with typical numerical values in the range $\frac{1}{4} \leq \psi_{\min} \leq \frac{1}{2}$. Concerning ψ_{\max} , a relation with ψ_{\min} readily follows from the requirement that in the neighborhood of a shock the maximum upstream bias can at most correspond to a fully upwind algorithm, for an essentially non-oscillatory capturing of shock waves. Hence, from (118), $\psi_{i+\frac{1}{2}} \leq 1$ with $i + \frac{1}{2}$ denoting the centroid of a finite element (cell) that supports a shock. For a typical case of a shock captured within at least two cells, as shown in Figure 14, (119) leads to $\psi_i = \psi_{\max}$ and $\psi_{i+1} \simeq \psi_{\min}$. From (118), therefore

$$\frac{\psi_{\max} + \psi_{\min}}{2} \leq 1 \Rightarrow \psi_{\max} \leq 2 - \psi_{\min} \quad (122)$$

which linearly decreases as a function of increasing ψ_{\min} . The specific objective of letting ψ^h vary as the solution evolves is to minimize induced upstream-bias dissipation for maximum accuracy within the prescribed computational stencil. As its distinguishing design feature, the acoustics-convection upstream resolution algorithm nevertheless remains an authentic characteristics-bias formulation for any ψ^h with $\psi_{\min} \leq \psi^h \leq \psi_{\max}$.

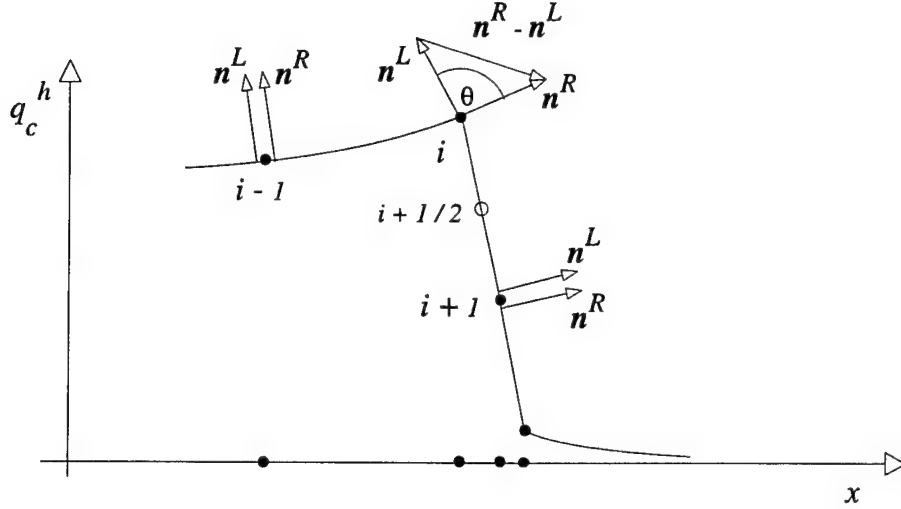


Figure 14: Local Unit Vectors at a Shock

The general expression of φ_i corresponding to a scalar component q_c^h of q^h directly derives from the finite element expansion (110), which can be expressed in synthetic implicit form as $F(q_c^h, \mathbf{x}, t) \equiv q_c^h - q_c^h(\mathbf{x}, t) = 0$. Hence, a normal unit vector \mathbf{n} can be cast at each time level t as $\mathbf{n} \equiv \text{grad } F(q_c^h, \mathbf{x}, t) / \|\text{grad } F\|$, where the vector operator “grad” encompasses the dependent variable q_c^h . For an n -dimensional formulation, with $1 \leq n \leq 3$, the expression for the corresponding φ_i at time level t and face centroid \mathbf{x}_i then becomes

$$\begin{aligned} \varphi_i \equiv \varphi^h(\mathbf{x}_i, t) &= \frac{1}{2} \left[\left(\frac{1}{\sqrt{1 + \sum_{\ell=1}^n \frac{\partial q_c^{hR}}{\partial x_\ell} \frac{\partial q_c^{hR}}{\partial x_\ell}}} - \frac{1}{\sqrt{1 + \sum_{\ell=1}^n \frac{\partial q_c^{hL}}{\partial x_\ell} \frac{\partial q_c^{hL}}{\partial x_\ell}}} \right)^2 \right. \\ &+ \left. \sum_{j=1}^n \left(\frac{\frac{\partial q_c^{hR}}{\partial x_j}}{\sqrt{1 + \sum_{\ell=1}^n \frac{\partial q_c^{hR}}{\partial x_\ell} \frac{\partial q_c^{hR}}{\partial x_\ell}}} - \frac{\frac{\partial q_c^{hL}}{\partial x_j}}{\sqrt{1 + \sum_{\ell=1}^n \frac{\partial q_c^{hL}}{\partial x_\ell} \frac{\partial q_c^{hL}}{\partial x_\ell}}} \right)^2 \right]_{x=x_i}^{\frac{1}{2}} \end{aligned} \quad (123)$$

The 1-D form of φ_i is

$$\varphi_i \equiv \varphi^h(\mathbf{x}_i, t) = \frac{1}{2} \left[\left(\frac{1}{\sqrt{1 + \left(\frac{\partial q_c^{hR}}{\partial x} \right)^2}} - \frac{1}{\sqrt{1 + \left(\frac{\partial q_c^{hL}}{\partial x} \right)^2}} \right)^2 \right]$$

$$+ \left[\left(\frac{\frac{\partial q_c^{hR}}{\partial x}}{\sqrt{1 + \left(\frac{\partial q_c^{hR}}{\partial x} \right)^2}} - \frac{\frac{\partial q_c^{hL}}{\partial x}}{\sqrt{1 + \left(\frac{\partial q_c^{hL}}{\partial x} \right)^2}} \right)^2 \right]_{x=x_i}^{\frac{1}{2}} \quad (124)$$

where the partial derivatives are determined through the finite element expansion (110), and where superscripts *L* and *R* indicate evaluation within the elements respectively to the left and right of the shared face where $x = x_i$ lies.

The representative 1-D form of (124) at node *i* of a uniform grid is

$$\begin{aligned} \varphi_i = & \frac{1}{2} \left[\left(\frac{\Delta x}{\sqrt{\Delta x^2 + (q_{c_{i+1}} - q_{c_i})^2}} - \frac{\Delta x}{\sqrt{\Delta x^2 + (q_{c_i} - q_{c_{i-1}})^2}} \right)^2 \right. \\ & \left. + \left(\frac{q_{c_{i+1}} - q_{c_i}}{\sqrt{\Delta x^2 + (q_{c_{i+1}} - q_{c_i})^2}} - \frac{q_{c_i} - q_{c_{i-1}}}{\sqrt{\Delta x^2 + (q_{c_i} - q_{c_{i-1}})^2}} \right)^2 \right]^{\frac{1}{2}} \end{aligned} \quad (125)$$

where the denominator never vanishes. This expression, furthermore, remains bounded and differentiable for arbitrary nodal values of q_c^h . For the sole purpose of determining the order of this expression with respect to Δx , for a smooth solution over any two contiguous elements, the discrete solution values q_{c_j} , $i-1 \leq j \leq i+1$, over these elements, can be considered as the nodal values of a single auxiliary continuous functions $q_c(x, t)$: a Lagrangian, trigonometric, or other interpolant of the q_{c_j} 's over both elements. With this consideration, the Taylor's series expansion of (125) yields

$$\varphi_i = \frac{\left| q_c''(x_i, t) \right|}{1 + (q_c'(x_i, t))^2} \frac{\Delta x}{2} + \mathcal{O}(\Delta x^2) = \mathcal{K} \left[1 + (q_c'(x_i, t))^2 \right]^{\frac{1}{2}} \frac{\Delta x}{2} + \mathcal{O}(\Delta x^2) \quad (126)$$

where superscript prime indicates differentiation with respect to x and \mathcal{K} denotes the local curvature. This expansion reveals that φ_i decreases for vanishing Δx . Even for large slopes, furthermore, φ_i remains of order Δx in regions of small curvature. Only when both curvature and slope drastically rise, e.g. at a shock, will φ_i increase, which precisely corresponds to the desired behavior.

10 Implicit Runge Kutta Time Integration

The finite element equations (112) along with appropriate boundary equations and conditions can be abridged as the non-linear ODE system

$$\mathcal{M} \frac{dQ(t)}{dt} = F(t, Q(t)) \quad (127)$$

where $\mathcal{M} \frac{dQ(t)}{dt}$ corresponds to the coupling of time derivatives in (112), and $F(t, Q(t))$ represents the remaining terms in (112). The numerical time integration of (127) in this study takes place through a new class of two-stage diagonally implicit Runge-Kutta algorithms⁷ (IRK2) expressed as

$$\begin{aligned} Q_{n+1} - Q_n &= b_1 K_1 + b_2 K_2 \\ MK_1 &= \Delta t \cdot F(t_n + c_1 \Delta t, Q_n + a_{11} K_1) \\ MK_2 &= \Delta t \cdot F(t_n + c_2 \Delta t, Q_n + a_{21} K_1 + a_{22} K_2) \end{aligned} \quad (128)$$

where n now denotes a discrete time station and $b_1, b_2, c_1, c_2, a_{11}, a_{21}$, and a_{22} indicate constant Runge-Kutta coefficients, subject to the constraints $c_i = \sum_{j=1}^2 a_{ij}$ and $\sum_{i=1}^2 b_i = 1$. The coefficients for second order accuracy are listed in the Table 1. With these coefficients, in particular, algorithm

Table 1: Runge-Kutta Coefficients

	b_1	b_2	a_{11}	a_{21}	a_{22}
IRK2	$\frac{3 - \sqrt{3}}{4}$	$\frac{1 + \sqrt{3}}{4}$	$\frac{3 - \sqrt{3}}{6}$	$2 - \sqrt{3}$	$\frac{\sqrt{3} - 1}{2}$

(128) becomes absolutely stable for arbitrary stiff non-linear dissipative ODE systems.^{7,12}

This algorithm is implicit because the entries in the arrays K_1 and K_2 remain coupled and are then computed by solving algebraic systems. Diagonally implicit signifies that K_1 is determined independently of K_2 . Thus, given the solution Q_n at time t_n , K_1 is computed first, followed by K_2 . The solution Q_{n+1} is then determined by way of the first expression in (128).

The terminal numerical solution is then determined using Newton's method, which for the implicit fully-coupled computation of the IRK2 arrays K_i , $1 \leq i \leq 2$, is cast as

$$\left[\mathcal{M} - a_{ii} \Delta t \left(\frac{\partial F}{\partial Q} \right)_{Q_i^p}^p \right] (K_i^{p+1} - K_i^p) = \Delta t F(t_n + c_i \Delta t, Q_i^p) - \mathcal{M} K_i^p$$

$$Q_i^p \equiv Q_n + a_{i1} K_1^p + a_{i2} K_2^p \quad (129)$$

where $a_{ij} = 0$ for $j > i$, p is the iteration index, and $K_1^p \equiv K_1$ for $i = 2$; for linear finite elements, the jacobian

$$J_i(Q) \equiv \mathcal{M} - a_{ii} \Delta t \left(\frac{\partial F}{\partial Q} \right)_{Q_i^p}^p \quad (130)$$

then becomes a block sparse matrix. The initial estimate K_i^0 can be set equal to the zero array. When one iteration only is executed for (129) within each time interval Newton's iteration becomes akin to a classical direct linearized implicit solver.

11 Concluding Remarks

The characteristics-bias upstream method rests upon the physics and mathematics of multi - dimensional characteristic acoustics and convection for general equations of state. It generates the upstream bias at the differential equation level, before any discrete approximation, by way of a characteristics-bias system and associated decomposition of the Euler flux divergence into convection and streamline and crossflow acoustic components.

A natural Galerkin finite element discretization of the characteristics-bias system directly provides an accurate and genuinely multi-dimensional upstream- bias approximation of the Euler and Navier-Stokes equations, in the form of a non-linear combination of upstream diffusive and downstream anti-diffusive flux differences, with greater bias on the upstream diffusive flux difference.

Along all the infinite directions of wave propagation, the formulation induces anisotropic and variable-strength consistent upstream bias that correlates with the spatial distribution of characteristic velocities. The developments in this report have implemented the algorithm using a linear approximation of fluxes within quadrilateral cells without any MUSCL-type local extrapolation of variables.

This characteristics-bias algorithm, admits a straightforward implicit implementation, features a computational simplicity that parallels a traditional centered discretization, and rationally eliminates superfluous artificial diffusion.

Acknowledgements

The research in this paper has been partly supported by the U.S. Army Research Office (ARO) under grant number DAAH04-96-1-0095. The author is especially grateful to Dr. Tom Doligalski, program manager, for this ARO support.

References

- [1] A. J. Baker and J. W. Kim, "A Taylor Weak Statement Algorithm for Hyperbolic Conservation Laws", *International Journal for Numerical Methods in Fluids*, 7, 489-520, (1987).
- [2] H. Luo, J. D. Baum, R. Löhner, J. Cabello, "Adaptive Edge-Based Finite Element Schemes for the Euler and Navier-Stokes Equations on Unstructured Grids", *AIAA 93-0336* (1993).
- [3] T. J. R. Hughes and A. Brooks, "A Theoretical Framework for Petrov-Galerkin Methods with Discontinuous Weighting Functions: Application to the Streamline-Upwind Procedure", *Finite Elements in Fluids IV*, 47-65, John Wiley, (1982).
- [4] T. J. R. Hughes, "Recent Progress in the Development and Understanding of SUPG Methods with Special Reference to the Compressible Euler and Navier-Stokes Equations", *International Journal for Numerical Methods in Fluids*, 7, 11, (1987).
- [5] C. Johnson, *Numerical Solution of Partial Differential Equations by the Finite Element Method*, Cambridge (1987).
- [6] C. Johnson and Anders Szepessy, "On the Convergence of a Finite Element Method for a Nonlinear Hyperbolic Conservation Law", *Mathematics of Computation*, 49, 180, 427-444, (1987).
- [7] C. Johnson, A. Szepessy, P. Hansbo, "On the Convergence of Shock-Capturing Streamline Diffusion Finite Element Methods for Hyperbolic Conservation Laws", *Mathematics of Computation*, 54, 189, 107-129, (1990).
- [8] J.-C. Carette, H. Deconinck, H. Paillere, P. L. Roe, "Multidimensional Upwinding: Its Relation to Finite Elements", *Inter. Journ. Numer. Meth. in Fluids*, 20, 935-955, (1995).
- [9] S.F. Davis, "A Rotationally-Biased Upwind Difference Scheme for the Euler Equations", *Journal of Computational Physics* 56, 65-92 (1984).
- [10] D.W. Levy, K.G. Powell, and B. van Leer, "Use of a Rotated Riemann Solver for the Two-Dimensional Euler Equations", *Journal of Computational Physics* 106, 201-214 (1993).
- [11] A. Dadone, and B. Grossman, "A Rotated Upwind Scheme for the Euler Equations", *AIAA 91-0635* (1991).
- [12] W. Coirier and B. van Leer, "Numerical Flux Formulas for the Euler and Navier-Stokes Equations: II. Progress in Flux-Vector Splitting", *AIAA-91-1566*, (1991).

- [13] C. L. Rumsey, B. van Leer, P. L. Roe, "A Multidimensional Flux Function with Applications to the Euler and Navier-Stokes Equations" *Journal of Computational Physics* 105, 306-323 (1993).
- [14] I. H. Parpia, "A Planar Oblique Wave Model for the Euler Equations" *AIAA-91-1545-CP*, (1991).
- [15] H. Paillere, H. Deconinck, R. Struijs, P. L. Roe, L.M. Mesaros, J.D. Muller, "Computations of Inviscid Compressible Flows Using Fluctuation-Splitting on Triangular Meshes", *AIAA 93-3301*, (1993).
- [16] P. L. Roe, "Beyond the Riemann Problem: Part I", in *Algorithmic Trends in CFD*, Springer Verlag (1993).
- [17] J. Iannelli "A CFD Euler Solver from a Physical Acoustics- Convection Flux Divergence Decomposition", Technical Report, U.S. Army Research Office, MAES-97-12-1.0-CFDL, Research Triangle Park, N.C., (1997)
- [18] C. Hirsch, *Numerical Computation of Internal and External Flows*, Vol. 1, 2 John Wiley & Sons, New York, NY, (1991).
- [19] W. G. Vincenti and C. H. Kruger, Jr., *Introduction to Physical Gas Dynamics*, John Wiley and Sons, Inc., New York, London, Sydney, (1965).
- [20] P. R. Garabedian, *Partial Differential Equations*, Chelsea Publishing Company, New York, N. Y., (1986).
- [21] E. Zauderer, *Partial Differential Equations of Applied Mathematics*, John Wiley, New York, N. Y., (1989).
- [22] J. Iannelli "A Characteristics - Based Finite Element Algorithm for Minimal Artificial Diffusion CFD", Technical Report, U.S. Army Research Office, ES96-1.0-CFDL, Research Triangle Park, N.C., (1996)
- [23] R. A. Horn, C. R. Johnson, *Matrix Analysis*, Cambridge (1991).
- [24] G. Iannelli "A Globally Well-Posed Accurate and Efficient Finite Element CFD Algorithm for Compressible Aerodynamics", Ph.D. Dissertation, The University of Tennessee, Knoxville, (1991).
- [25] G. S. Iannelli, A. J. Baker, "An Intrinsically N-Dimensional Generalized Flux Vector Splitting Implicit Finite Element Euler Algorithm Aerodynamics", *AIAA 91-0123*, 29th Aerospace Sciences Meeting, Reno, NV, (1991).
- [26] G. S. Iannelli "A Non-linear Element-Upstream Weak Statement Finite Element Algorithm for Conservation Laws" University of Tennessee Tech. Report CFDL/95-2-1.0, (1995).
- [27] K. Dekker and J.G. Verwer, *Stability of Runge-Kutta Methods for Stiff Non-Linear Differential Equations*, Elsevier Publishers, Amsterdam, (1984).

A Solutions in Non-linear Wave-Like Form

With implied summation on repeated indices, a solution of the Euler equations in non-linear wave-like form is expressed as

$$q = q(\eta_1) \quad , \quad \eta_1 \equiv \mathbf{x} \cdot \mathbf{n} - \lambda(q)t = x_j n_j - \lambda(q)t \quad (131)$$

where \mathbf{n} denotes a propagation-direction unit vector, independent of (\mathbf{x}, t) , and $\lambda = \lambda(q)$ indicates a solution-dependent wave-propagation velocity component along the \mathbf{n} direction. For $\mathbf{x} \cdot \mathbf{n} - \lambda(q)t$ equal to a constant, the wave-like solution q in (131) remains itself constant, which also makes $\lambda = \lambda(q)$ a constant. In the time-space continuum (\mathbf{x}, t) , therefore, the equation

$$\mathbf{x} \cdot \mathbf{n} - \lambda t = \mathcal{C} \quad (132)$$

represents a hyper-plane with \mathcal{C} and $(n_1, n_2, n_3, -\lambda(q))$ respectively denoting a constant and a unit vector orthogonal to this plane, as depicted in Figure 15. The surface that remains tangent to these planes for all \mathbf{n} 's is then tangent itself to a characteristic surface, for λ corresponding to a characteristic velocity component. Equation (132) corresponds in the (x_1, x_2) space of a 2-D flow to a bundle of parallel lines for a fixed t and different \mathcal{C} . For a fixed \mathcal{C} and variable t , the equation represents a \mathcal{C} -line propagating in the \mathbf{n} direction with velocity component λ .

Next, consider the coordinate transformation

$$\eta_1 = x_j n_j - \lambda(q)t \quad , \quad \eta_2 = \eta_2(x_1, x_2, x_3, t) \quad , \quad \eta_3 = \eta_3(x_1, x_2, x_3, t) \quad , \quad \eta_4 = \eta_4(x_1, x_2, x_3, t) \quad (133)$$

with η_2 , η_3 , and η_4 chosen so that the reference frame $(\eta_1, \eta_2, \eta_3, \eta_4)$ is also right-handed like (x_1, x_2, x_3, t) . With this transformation, $q(x_j n_j - \lambda(q)t) = q(\eta_1)$ and for each t and non-linear q , the η_1 axis then points in the $(n_1, n_2, n_3, -\lambda(q))$ direction. This result follows from the partial derivatives of η_1 with respect to (x_1, x_2, x_3, t)

$$\left(1 + t \frac{\partial \lambda}{\partial \eta_1}\right) \frac{\partial \eta_1}{\partial t} = -\lambda(q) \quad , \quad \left(1 + t \frac{\partial \lambda}{\partial \eta_1}\right) \frac{\partial \eta_1}{\partial x_j} = n_j \quad (134)$$

hence

$$\frac{-\lambda}{\frac{\partial \eta_1}{\partial t}} = \frac{n_1}{\frac{\partial \eta_1}{\partial x_1}} = \frac{n_2}{\frac{\partial \eta_1}{\partial x_2}} = \frac{n_3}{\frac{\partial \eta_1}{\partial x_3}} \quad (135)$$

which shows that the η_1 -axis direction vector $(\frac{\partial \eta_1}{\partial x_1}, \frac{\partial \eta_1}{\partial x_2}, \frac{\partial \eta_1}{\partial x_3}, \frac{\partial \eta_1}{\partial t})$ is parallel to $(n_1, n_2, n_3, -\lambda(q))$. Since \mathbf{n} is a unit vector, the second result in (134) also leads to the following relations

$$\left(1 + t \frac{\partial \lambda}{\partial \eta_1}\right) \frac{\partial \eta_1}{\partial x_\ell} n_\ell = 1 \quad , \quad \frac{\partial \eta_1}{\partial x_j} = \frac{\partial \eta_1}{\partial x_\ell} n_\ell n_j \quad (136)$$

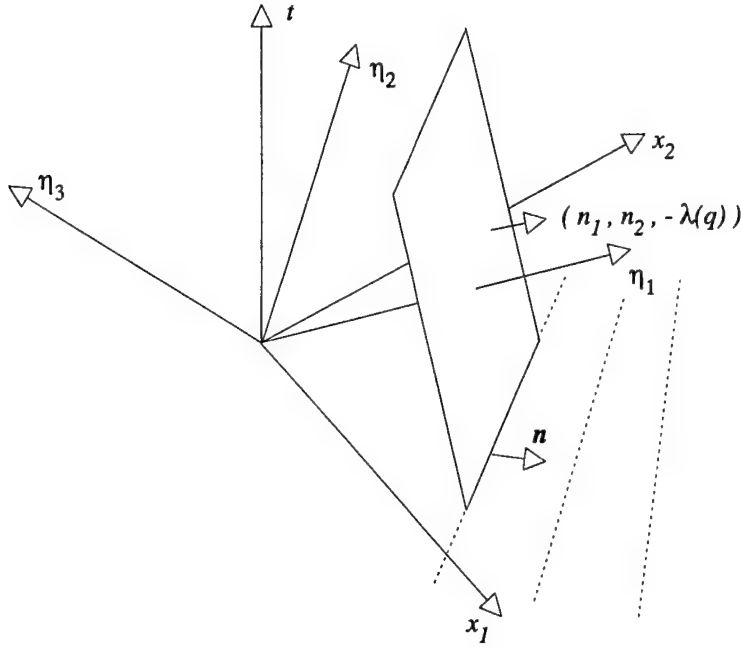


Figure 15: Wave Plane and Reference Frames

The partial derivatives of the wave-like solutions (131) also satisfy the conditions

$$\frac{\partial q}{\partial t} = -\lambda(q) \frac{\partial q}{\partial x_\ell} n_\ell, \quad \lambda(q) \frac{\partial q}{\partial x_j} = -n_j \frac{\partial q}{\partial t} \quad (137)$$

This result follows from the partial derivatives of (131) as

$$\frac{\partial q}{\partial t} = \frac{\partial q}{\partial \eta_1} \left(-t \frac{\partial \lambda}{\partial q} \frac{\partial q}{\partial t} - \lambda(q) \right), \quad \frac{\partial q}{\partial x_j} = \frac{\partial q}{\partial \eta_1} \left(-t \frac{\partial \lambda}{\partial q} \frac{\partial q}{\partial x_j} + n_j \right) \quad (138)$$

where $\frac{\partial q}{\partial \eta_1}$ denotes a column array and $\frac{\partial \lambda}{\partial q}$ indicates a row array, which implies that $\frac{\partial q}{\partial \eta_1} \frac{\partial \lambda}{\partial q}$ is a square matrix. These relations then lead to the two systems

$$\left(I + t \frac{\partial q}{\partial \eta_1} \frac{\partial \lambda}{\partial q} \right) \frac{\partial q}{\partial t} = -\lambda(q) \frac{\partial q}{\partial \eta_1}, \quad \left(I + t \frac{\partial q}{\partial \eta_1} \frac{\partial \lambda}{\partial q} \right) \frac{\partial q}{\partial x_j} = n_j \frac{\partial q}{\partial \eta_1} \quad (139)$$

where I denotes a 4×4 identity matrix. Since the square matrix $\frac{\partial q}{\partial \eta_1} \frac{\partial \lambda}{\partial q}$ results from the product of column and row arrays, the rows of this matrix are all linear combinations of the single $\frac{\partial \lambda}{\partial q}$ row. All the eigenvalues of this matrix, but one, therefore, vanish. Consequently, all the eigenvalues of the matrix $\left(I + t \frac{\partial q}{\partial \eta_1} \frac{\partial \lambda}{\partial q} \right)$ equal 1, except one eigenvalue $\tilde{\lambda}$, which has been exactly determined as

$$\tilde{\lambda} = 1 + t \frac{\partial \lambda}{\partial \eta_1} \quad (140)$$

As the product of all its matrix eigenvalues, therefore, the determinant of the matrix $\left(I + t \frac{\partial q}{\partial \eta_1} \frac{\partial \lambda}{\partial q} \right)$ equals $\tilde{\lambda}$, and the associated matrix of cofactors is then denoted with B . Systems (139) can then be solved to yield

$$\frac{\partial q}{\partial t} = -\frac{\lambda(q)}{1 + t \frac{\partial \lambda}{\partial \eta_1}} B \frac{\partial q}{\partial \eta_1}, \quad \frac{\partial q}{\partial x_j} = \frac{n_j}{1 + t \frac{\partial \lambda}{\partial \eta_1}} B \frac{\partial q}{\partial \eta_1} \quad (141)$$

With a finite $\frac{\partial q}{\partial \eta_1}$, if the denominator $1 + t \frac{\partial \lambda}{\partial \eta_1}$ approaches zero, then $\frac{\partial q}{\partial t}$ and $\frac{\partial q}{\partial x_j}$ become unbounded, which indicates that a positive $t = -1/\frac{\partial \lambda}{\partial \eta_1}$ corresponds to a “breaking” time of shock-wave formation. In any region that does not contain shock waves, or in the absence of shock waves, therefore, $\tilde{\lambda} = 1 + t \frac{\partial \lambda}{\partial \eta_1}$ does not vanish, the matrix $(I + t \frac{\partial q}{\partial \eta_1} \frac{\partial \lambda}{\partial q})$ is not singular, and the corresponding wave-like solutions are non-singular. Unless stated otherwise, the wave-like solutions considered in the following sections are non-singular. For these solutions, comparing the two results in (141) generates the second expression in (137), while the operations of contracting this expression with n_j then returns the first expression in (137), which in view of $q = q(\eta_1)$ can also be expressed as

$$\frac{\partial q}{\partial t} = -\lambda(q) \frac{\partial q}{\partial \eta_1} \frac{\partial \eta_1}{\partial x_\ell} n_\ell \quad (142)$$

The velocity component $\lambda = \lambda(q)$ is determined by imposing the condition that the non-linear wave-like expression (131) satisfies the Euler equations (1). For $q = q(\eta_1)$, system (1) becomes

$$\frac{\partial q}{\partial t} + \frac{\partial f_j}{\partial q} \frac{\partial \eta_1}{\partial x_j} \frac{\partial q}{\partial \eta_1} = 0 \quad (143)$$

Substitution into this system of (142) and the second of (136), respectively for $\frac{\partial q}{\partial t}$ and $\frac{\partial \eta_1}{\partial x_j}$, leads to

$$\frac{\partial \eta_1}{\partial x_\ell} n_\ell \left(-\lambda(q) \frac{\partial q}{\partial \eta_1} + \frac{\partial f_j}{\partial q} n_j \frac{\partial q}{\partial \eta_1} \right) = 0 \quad (144)$$

which yields the eigenvalue problem

$$\left(-\lambda(q) I + \frac{\partial f_j}{\partial q} n_j \right) \frac{\partial q}{\partial \eta_1} = 0 \quad (145)$$

B Wave-Propagation and Characteristic Surfaces

B.1 Wave-Propagation Surfaces

The wave propagation surface is the surface where acoustic and convection waves propagate and therefore, is the surface that remains tangent to the wave-propagation hyper-planes expressed by (132) for λ corresponding to a wave-propagation velocity component. The surface

$$q_\ell(x_j n_j - \lambda t) = \text{constant} \quad (146)$$

for each scalar component q_ℓ within q is then itself tangent to a characteristic surface for an appropriate “constant”, because

$$\text{grad } q_\ell = -\frac{1}{\lambda} (n_1, n_2, n_3, -\lambda) \frac{\partial q_\ell}{\partial t} \quad \text{parallel to} \quad (n_1, n_2, n_3, -\lambda) \quad (147)$$

as obtained from the second expression in (137).

Let, then

$$\mathcal{F}(x_1, x_2, x_3, t) = \text{constant} \quad (148)$$

represent the mathematical function of a wave-propagation surface. From vector analysis the vector $\text{grad } \mathcal{F}$ remains perpendicular to the surface at each point. Since the surface must be tangent to the propagation plane (132), $\text{grad } \mathcal{F}$ must be parallel at each point to the unit vector $(n_1, n_2, n_3, -\lambda)$ itself perpendicular to plane (132). With $n_j n_j = 1$, this condition yields

$$n_1 = \mp \frac{\frac{\partial \mathcal{F}}{\partial x_1}}{\sqrt{\frac{\partial \mathcal{F}}{\partial x_j} \frac{\partial \mathcal{F}}{\partial x_j}}} \quad , \quad n_2 = \mp \frac{\frac{\partial \mathcal{F}}{\partial x_2}}{\sqrt{\frac{\partial \mathcal{F}}{\partial x_j} \frac{\partial \mathcal{F}}{\partial x_j}}} \quad , \quad n_3 = \mp \frac{\frac{\partial \mathcal{F}}{\partial x_3}}{\sqrt{\frac{\partial \mathcal{F}}{\partial x_j} \frac{\partial \mathcal{F}}{\partial x_j}}} \quad , \quad \lambda = \pm \frac{\frac{\partial \mathcal{F}}{\partial t}}{\sqrt{\frac{\partial \mathcal{F}}{\partial x_j} \frac{\partial \mathcal{F}}{\partial x_j}}} \quad (149)$$

Substitution of these expressions into the eigenvalues (42) thus generates the separate propagation-surface differential equations

$$\mathcal{F}_t + u_j \mathcal{F}_{x_j} = 0 \quad , \quad \left(\mathcal{F}_t + u_j \mathcal{F}_{x_j} \right)^2 = c^2 \mathcal{F}_{x_j} \mathcal{F}_{x_j} \quad (150)$$

where a subscript variable denotes differentiation with respect to that variable. The different form of these two differential equations implies the existence of multiple propagation surfaces.

B.2 Characteristic Surfaces

The surfaces of wave propagation are characteristic surfaces. By definition, a characteristic surface is a surface across which the solution q of (1) may become discontinuous. Let η_1 indicate a coordinate in the direction normal to each facet of the characteristic surface, as shown in Figure 15

In terms of the partial derivative with respect to this coordinate direction, therefore, system (1) becomes singular, or equivalently, the derivative of q in this direction cannot be determined by the system itself, where q is not necessarily a wave-like solution. By expressing the partial derivatives of q in (1) in terms of other coordinates η_j as

$$\frac{\partial q}{\partial t} = \frac{\partial q}{\partial \eta_\ell} \frac{\partial \eta_\ell}{\partial t} \quad , \quad \frac{\partial q}{\partial x_j} = \frac{\partial q}{\partial \eta_\ell} \frac{\partial \eta_\ell}{\partial x_j} \quad (151)$$

system (1) becomes

$$\left(I \frac{\partial \eta_1}{\partial t} + \frac{\partial f_j(q)}{\partial q} \frac{\partial \eta_1}{\partial x_j} \right) \frac{\partial q}{\partial \eta_1} = - \sum_{\ell=2}^4 \left(I \frac{\partial \eta_\ell}{\partial t} + \frac{\partial f_j(q)}{\partial q} \frac{\partial \eta_\ell}{\partial x_j} \right) \frac{\partial q}{\partial \eta_\ell} \quad (152)$$

where $\left(\frac{\partial \eta_1}{\partial x_1}, \frac{\partial \eta_1}{\partial x_2}, \frac{\partial \eta_1}{\partial x_3}, \frac{\partial \eta_1}{\partial t} \right)$ represent the cartesian components of a vector normal to a facet of each “ $\mathcal{F} = \text{constant}$ ” characteristic surface. From vector analysis, the components of this normal vector can then be expressed in terms of the gradient of \mathcal{F} as

$$\frac{\partial \eta_1}{\partial t} = k \frac{\partial \mathcal{F}}{\partial t} \quad , \quad \frac{\partial \eta_1}{\partial x_j} = k \frac{\partial \mathcal{F}}{\partial x_j} \quad (153)$$

where k is a single scalar constant. With this specification, system (152) becomes

$$k \left(I \frac{\partial \mathcal{F}}{\partial t} + \frac{\partial f_j(q)}{\partial q} \frac{\partial \mathcal{F}}{\partial x_j} \right) \frac{\partial q}{\partial \eta_1} = - \sum_{\ell=2}^4 \left(I \frac{\partial \eta_\ell}{\partial t} + \frac{\partial f_j(q)}{\partial q} \frac{\partial \eta_\ell}{\partial x_j} \right) \frac{\partial q}{\partial \eta_\ell} \quad (154)$$

which becomes singular, hence cannot determine $\frac{\partial q}{\partial \eta_1}$, when the “lhs” jacobian matrix is itself singular. Accordingly, the governing equation for the characteristic surface \mathcal{F} is the vanishing determinant

$$\det \left(I \frac{\partial \mathcal{F}}{\partial t} + \sum_{j=1}^3 \frac{\partial f_j(q)}{\partial q} \frac{\partial \mathcal{F}}{\partial x_j} \right) = 0 \quad (155)$$

which becomes

$$\left(\mathcal{F}_t + u_j \mathcal{F}_{x_j} \right)^2 \left(\left(\mathcal{F}_t + u_j \mathcal{F}_{x_j} \right)^2 - c^2 \mathcal{F}_{x_j} \mathcal{F}_{x_j} \right) = 0 \quad (156)$$

This expression yields the following partial differential equations for \mathcal{F}

$$\left(\mathcal{F}_t + u_j \mathcal{F}_{x_j} \right)^2 = 0 \quad , \quad \left(\mathcal{F}_t + u_j \mathcal{F}_{x_j} \right)^2 = c^2 \mathcal{F}_{x_j} \mathcal{F}_{x_j} \quad (157)$$

identical to (150), which proves that the surfaces of wave propagation are characteristic surfaces.

B.3 Characteristic Cones

The principal propagation directions as well as the supersonic- and subsonic- flow domain of dependence and range of influence of a flow field point P in the time-space continuum can be determined by studying the variation of the characteristic-surface shape versus the Mach number. To investigate these shape changes it suffices to study the shape changes of the corresponding characteristic cones, which are tangent at each flow field point P to the corresponding characteristic surfaces, but are far easier to determine.

The characteristic cones at each flow field point P are readily determined by significantly simplifying equations (157) through the following Galilean space-time coordinate transformation

$$\begin{cases} X_1 = x_1 - u_1 t \\ X_2 = x_2 - u_2 t \\ X_3 = x_3 - u_3 t \\ \tau = ct \end{cases} \quad (158)$$

where τ now denotes a “space-like” variable corresponding to the distance traveled by a constant-speed acoustic wave. With this coordinate transformation, the equation of each eventual cone corresponds to the shape of the cone as recorded by an observer that moves along with a fluid particle with local convection velocity \mathbf{u} .

By virtue of transformation (158), the function \mathcal{F} is recast as

$$\mathcal{F}(X_1, X_2, X_3, \tau) = \mathcal{F}(X_1(x_1, t), X_2(x_2, t), X_3(x_3, t), \tau(t)) \quad (159)$$

and the partial derivatives of \mathcal{F} with respect to X_1, X_2, X_3, τ and x_1, x_2, x_3, t are related as

$$\begin{aligned} \frac{\partial \mathcal{F}}{\partial x_1} \Big|_{x_2, x_3, t} &= \frac{\partial \mathcal{F}}{\partial X_1} \Big|_{X_2, X_3, \tau}, \quad \frac{\partial \mathcal{F}}{\partial x_2} \Big|_{x_1, x_3, t} = \frac{\partial \mathcal{F}}{\partial X_2} \Big|_{X_1, X_3, \tau}, \quad \frac{\partial \mathcal{F}}{\partial x_3} \Big|_{x_1, x_2, t} = \frac{\partial \mathcal{F}}{\partial X_3} \Big|_{X_1, X_2, \tau} \\ \frac{\partial \mathcal{F}}{\partial t} \Big|_{x_1, x_2, x_3} &= c \frac{\partial \mathcal{F}}{\partial \tau} \Big|_{X_1, X_2, X_3} - u_j \frac{\partial \mathcal{F}}{\partial x_j} \end{aligned} \quad (160)$$

With these partial-derivative relations, therefore, the characteristic-surface equations (157) simplify to

$$\mathcal{G} \equiv \left(\frac{\partial \mathcal{F}}{\partial \tau} \right)^2 = 0, \quad \mathcal{G} \equiv \left(\frac{\partial \mathcal{F}}{\partial \tau} \right)^2 - \left(\frac{\partial \mathcal{F}}{\partial X_1} \right)^2 - \left(\frac{\partial \mathcal{F}}{\partial X_2} \right)^2 - \left(\frac{\partial \mathcal{F}}{\partial X_3} \right)^2 = 0 \quad (161)$$

The equation of the tangent characteristic cone is then directly obtained from these equations upon using the correct multi-dimensional generalization of the Monge-cone ordinary differential system,²⁰⁻²¹ which yields the characteristic-cone differential equations

$$\begin{aligned} \frac{d(\frac{\partial \mathcal{F}}{\partial X_1})}{\frac{\partial \mathcal{G}}{\partial X_1} + \frac{\partial \mathcal{G}}{\partial \mathcal{F}} \frac{\partial \mathcal{F}}{\partial X_1}} &= \frac{d(\frac{\partial \mathcal{F}}{\partial X_2})}{\frac{\partial \mathcal{G}}{\partial X_2} + \frac{\partial \mathcal{G}}{\partial \mathcal{F}} \frac{\partial \mathcal{F}}{\partial X_2}} = \frac{d(\frac{\partial \mathcal{F}}{\partial X_3})}{\frac{\partial \mathcal{G}}{\partial X_3} + \frac{\partial \mathcal{G}}{\partial \mathcal{F}} \frac{\partial \mathcal{F}}{\partial X_3}} = \frac{d(\frac{\partial \mathcal{F}}{\partial \tau})}{\frac{\partial \mathcal{G}}{\partial \tau} + \frac{\partial \mathcal{G}}{\partial \mathcal{F}} \frac{\partial \mathcal{F}}{\partial \tau}} = \\ &= \frac{dX_1}{-\frac{\partial \mathcal{G}}{\partial(\frac{\partial \mathcal{F}}{\partial X_1})}} = \frac{dX_2}{-\frac{\partial \mathcal{G}}{\partial(\frac{\partial \mathcal{F}}{\partial X_2})}} = \frac{dX_3}{-\frac{\partial \mathcal{G}}{\partial(\frac{\partial \mathcal{F}}{\partial X_3})}} = \frac{d\tau}{-\frac{\partial \mathcal{G}}{\partial(\frac{\partial \mathcal{F}}{\partial \tau})}} \end{aligned} \quad (162)$$

The solution of these ordinary differential equations for each equation in (161) is

$$\begin{cases} X_1 - X_{1o} = 0 \\ X_2 - X_{2o} = 0 \\ X_3 - X_{3o} = 0 \end{cases}, \quad (X_1 - X_{1o})^2 + (X_2 - X_{2o})^2 + (X_3 - X_{3o})^2 = (\tau - \tau_o)^2 \quad (163)$$

By virtue of (158), the equation of the first characteristic cone with respect to the fixed reference coordinates (x_1, x_2, x_3, t) then becomes

$$\frac{x_1 - x_{1o}}{t - t_o} = u_1, \quad \frac{x_2 - x_{2o}}{t - t_o} = u_2, \quad \frac{x_3 - x_{3o}}{t - t_o} = u_3 \quad (164)$$

In the time-space continuum of a 2-D flow, these equations correspond to the single “convection” straight line S^-S^+ , as displayed in Figures 16-17. As time elapses, therefore, waves reach and then leave P along this line, which projects onto the 3-D streamline

$$\frac{x_1 - x_{1o}}{u_1} = \frac{x_2 - x_{2o}}{u_2} = \frac{x_3 - x_{3o}}{u_3} \quad (165)$$

in the space continuum. A spatial discretization that aims to model this propagation mode, therefore, can receive un upstream bias in the streamline direction.

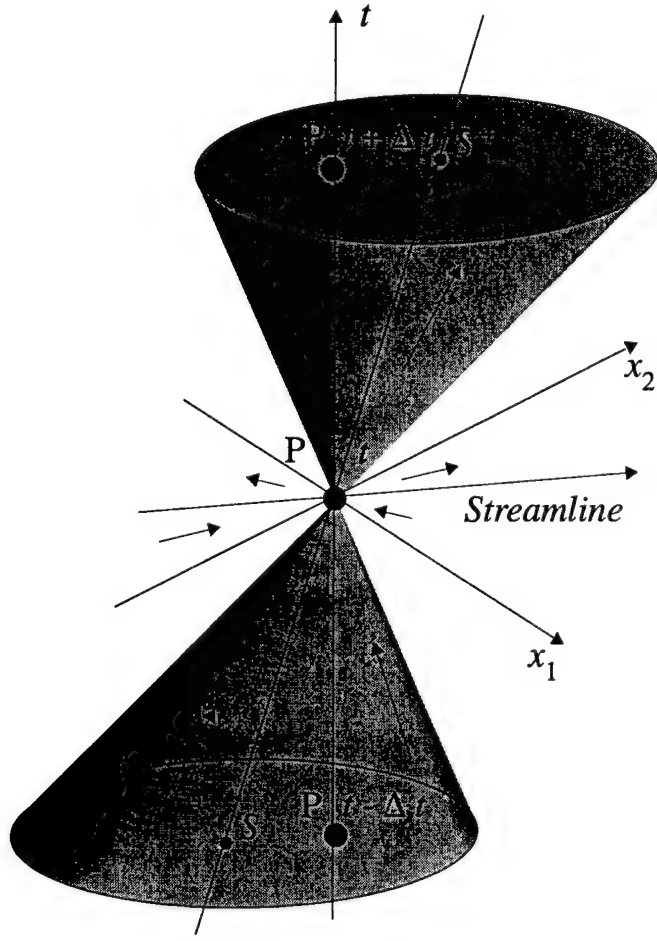


Figure 16: Subsonic Characteristic Cone

In the time-space continuum, the equation of the second characteristic cone becomes

$$(x_1 - x_{1o} - u_1(t - t_o))^2 + (x_2 - x_{2o} - u_2(t - t_o))^2 + (x_3 - x_{3o} - u_3(t - t_o))^2 = c^2(t - t_o)^2 \quad (166)$$

hence

$$(x_1 - x_{1o} - u_1(t - t_o))^2 + (x_2 - x_{2o} - u_2(t - t_o))^2 + (x_3 - x_{3o} - u_3(t - t_o))^2 = \|u\|^2 \frac{(t - t_o)^2}{M^2} \quad (167)$$

This equation corresponds to a characteristic cone with vertex at P that is tangent to the local characteristic surface at P and whose shape depends on M . As time elapses, therefore, waves funnel in towards P and out and away from P within the characteristic cone. In the space continuum, expression (167) also represents the equation of a family of spheres with center coordinates $[x_{1o} + u_1(t - t_o), x_{2o} + u_2(t - t_o), x_{3o} + u_3(t - t_o)]$ and radius $\|u\|(t - t_o)/M$. For a vanishing c , furthermore, this cone collapses onto the convection line (164), which, however, is not the axis of the characteristic cone. Figures 16-17 portray this characteristic cone for subsonic and supersonic 2-D flows. Significantly, as M increases, the cone shears in the streamline direction, while its cross section remains an ellipse, whose axes project onto the streamline and crossflow directions.

As a fundamental geometric difference between supersonic and subsonic flows, a time axis through P is respectively outside and inside the cone. In this manner, time-independent rays, i.e. lines issuing from the time axis for constant t , that are tangent to this cone only exist when the time axis is not inside the cone, that is for supersonic flows. The lines that issue from the time axis and are tangent to spheres (167) in the (x_1, x_2, x_3) domain are then found to be Mach cones. This finding is not coincidental, because time-invariant rays tangent to the characteristic cone correspond to steady-state (i.e. time-invariant) characteristic surfaces, which are the Mach cones for the steady Euler equations, as remarked at the end of Section 4.2.

Figure 16 presents the subsonic characteristic cone for a 2-D flow. The time axis is inside the cone and no tangent time-invariant lines exist. Accordingly, as time elapses, in this case, the funneling of waves within the cone, towards and then away from P , corresponds on any constant- t plane to closed curves encircling P that shrink towards P and then expand away from P . From this perspective, a region of space centered about P is simultaneously the domain of dependence and range of influence for P . A spatial discretization that aims to model this propagation mode, therefore, should receive an upstream bias along all directions radiating from P .

Figure 17 presents the supersonic characteristic cone for a 2-D flow.

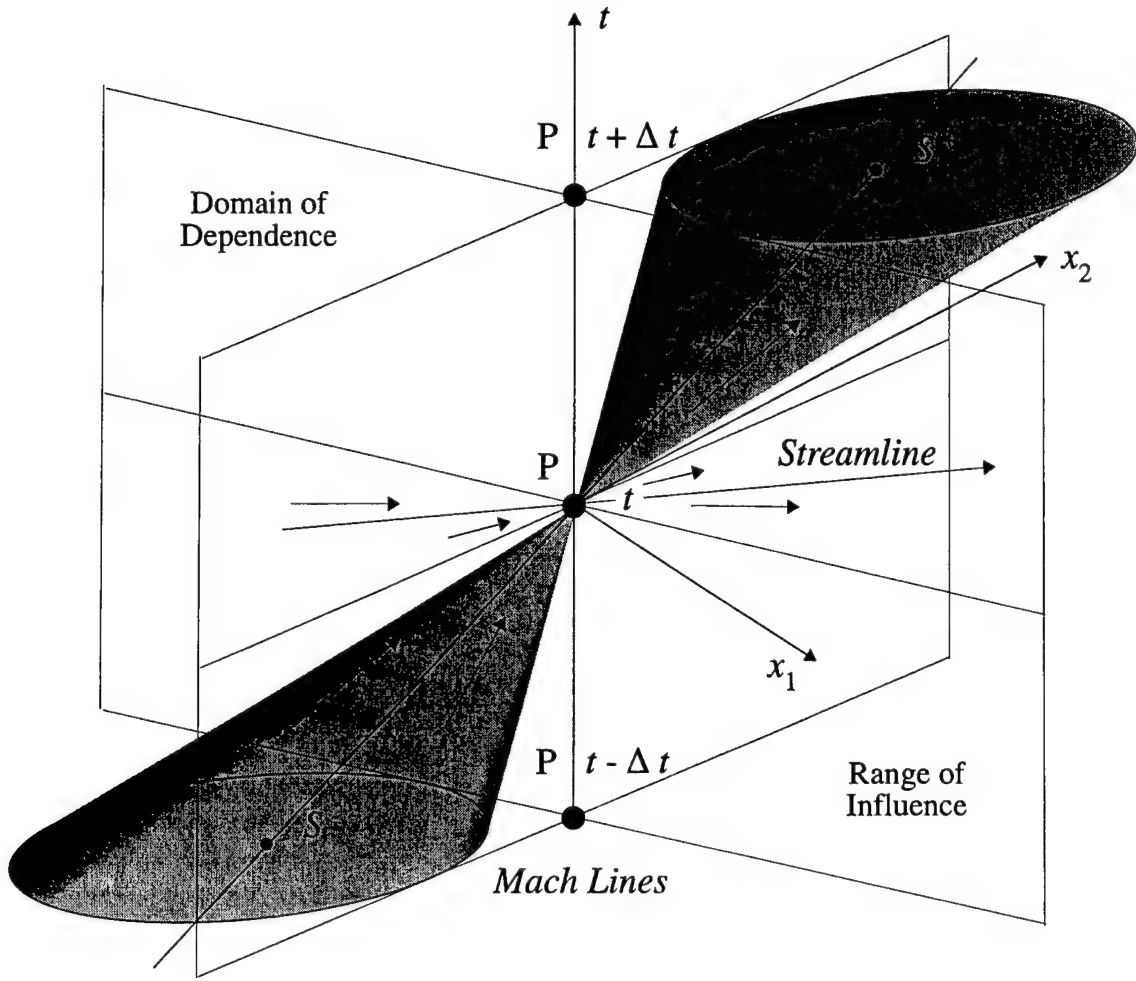


Figure 17: Supersonic Characteristic Cone

The time axis is outside the cone and the Mach lines are tangent to the cone on each constant- t plane. As time elapses, in this case, the funneling of waves within the cone, towards and then away from P , corresponds on any constant- t plane to information reaching P within its domain of dependence, between the two Mach lines upstream of P , and leaving P within its range of influence, between the two Mach lines downstream of P . A spatial discretization that aims to model this propagation mode, therefore, should receive an upstream bias along all directions within the domain of dependence of P , with the streamline direction as the upstream bias principal direction, since the streamline remains the axis of the domain of dependence and region of influence.

The investigation of the characteristic cone shape change versus M , therefore, indicates that for unsteady and steady supersonic flows, the upstream-bias domain of dependence and region of influence for each flow field point P consist of the regions that contain the streamline through P and are bound by the Mach lines. For unsteady and steady subsonic flows, both the domain of dependence and region of influence encompass regions encircling P .

C Acoustics Matrices

Despite its zero eigenvalues, $A_j^a a_j$ features a complete set of eigenvectors X and thus possesses the similarity transformation

$$A_j^a a_j = X \Lambda^a X^{-1}, \quad \Lambda^a \equiv \begin{pmatrix} c, & 0, & 0, & 0, & 0 \\ 0, & -c, & 0, & 0, & 0 \\ 0, & 0, & 0, & 0, & 0 \\ 0, & 0, & 0, & 0, & 0 \\ 0, & 0, & 0, & 0, & 0 \end{pmatrix} \quad (168)$$

where the corresponding eigenvector matrix X and its inverse X^{-1} for general equations of state (7) are

$$X = \begin{pmatrix} p_E, & p_E, & p_E, & 0, & 0 \\ cp_E a_1, & -cp_E a_1, & 0, & -a_2, & -a_1 a_3 \\ cp_E a_2, & -cp_E a_2, & 0, & a_1, & -a_2 a_3 \\ cp_E a_3, & -cp_E a_3, & 0, & 0, & a_1^2 + a_2^2 \\ c^2 - p_\rho, & c^2 - p_\rho, & -p_\rho, & 0, & 0 \end{pmatrix} \quad (169)$$

$$X^{-1} = \frac{1}{2c^2 p_E} \begin{pmatrix} p_\rho, & ca_1, & ca_2, & ca_3, & p_E \\ p_\rho, & -ca_1, & -ca_2, & -ca_3, & p_E \\ 2(c^2 - p_\rho), & 0, & 0, & 0, & -2p_E \\ 0, & -\frac{2c^2 p_E a_2}{a_1^2 + a_2^2}, & \frac{2c^2 p_E a_1}{a_1^2 + a_2^2}, & 0, & 0 \\ 0, & -\frac{2c^2 p_E a_1 a_3}{a_1^2 + a_2^2}, & -\frac{2c^2 p_E a_2 a_3}{a_1^2 + a_2^2}, & 1, & 0 \end{pmatrix} \quad (170)$$

On the basis of this similarity transformation, $A_j^a a_j$ can then be multiply decomposed as

$$A^a = X \Lambda_n^{a+} X^{-1} + X \Lambda_n^{a-} X^{-1}, \quad \Lambda^a = \Lambda_n^{a+} + \Lambda_n^{a-} \quad (171)$$

where subscript n here denotes the number of non-zero eigenvalues within Λ_n^{a+} and Λ_n^{a-} . At least two specific decompositions of $A_j^a a_j$ can be considered, which respectively correspond to $n = 1$ and $n = 3$ and both lead to a conveniently simple bi-modal upstream approximation of $A_j^a a_j$. For $n = 1$, the expressions for Λ_n^{a+} and Λ_n^{a-} are:

$$\Lambda_1^{a+} \equiv \begin{pmatrix} c, & 0, & 0, & 0, & 0 \\ 0, & 0, & 0, & 0, & 0 \\ 0, & 0, & 0, & 0, & 0 \\ 0, & 0, & 0, & 0, & 0 \\ 0, & 0, & 0, & 0, & 0 \end{pmatrix}, \quad \Lambda_1^{a-} \equiv -\begin{pmatrix} 0, & 0, & 0, & 0, & 0 \\ 0, & c, & 0, & 0, & 0 \\ 0, & 0, & 0, & 0, & 0 \\ 0, & 0, & 0, & 0, & 0 \\ 0, & 0, & 0, & 0, & 0 \end{pmatrix} \quad (172)$$

the corresponding expressions for $n = 3$ are

$$\Lambda_3^{a+} \equiv \frac{1}{2} \begin{pmatrix} 2c, & 0, & 0, & 0, & 0 \\ 0, & 0, & 0, & 0, & 0 \\ 0, & 0, & c, & 0, & 0 \\ 0, & 0, & 0, & c, & 0 \\ 0, & 0, & 0, & 0, & c \end{pmatrix}, \quad \Lambda_3^{a-} \equiv -\frac{1}{2} \begin{pmatrix} 0, & 0, & 0, & 0, & 0 \\ 0, & 2c, & 0, & 0, & 0 \\ 0, & 0, & c, & 0, & 0 \\ 0, & 0, & 0, & c, & 0 \\ 0, & 0, & 0, & 0, & c \end{pmatrix} \quad (173)$$

For $n = 3$, the matrix product of $|A_j^a a_j|_3$ with the directional derivative $a_k \partial q / \partial x_k$ of q directly leads to the beautifully simple acoustic-field result

$$|A_j^a a_j|_3 a_k \frac{\partial q}{\partial x_k} = X c I X^{-1} a_k \frac{\partial q}{\partial x_k} = c a_k \frac{\partial q}{\partial x_k} \quad (174)$$

The similar results for $(a_1^{N_1}, a_2^{N_1}, a_3^{N_1})$ and $(a_1^{N_2}, a_2^{N_2}, a_3^{N_2})$ replacing (a_1, a_2, a_3) are

$$\left| A_j^a a_j^{N_1} \right|_3 a_k^{N_1} \frac{\partial q}{\partial x_k} = X_{N_1} c I X_{N_1}^{-1} a_k^{N_1} \frac{\partial q}{\partial x_k} = c a_k^{N_1} \frac{\partial q}{\partial x_k} \quad (175)$$

and

$$\left| A_j^a a_j^{N_2} \right|_3 a_k^{N_2} \frac{\partial q}{\partial x_k} = X_{N_2} c I X_{N_2}^{-1} a_k^{N_2} \frac{\partial q}{\partial x_k} = c a_k^{N_2} \frac{\partial q}{\partial x_k} \quad (176)$$

where I denotes the 5×5 identity matrix. For a vanishing M , therefore, all the eigenvalues of the streamline and crossflow absolute acoustic matrices approach $+c$.

D Upstream-Bias Stability Condition

In jacobian form, expression (88) becomes

$$\frac{\partial f_j^C}{\partial x_j} = \frac{\partial f_j}{\partial x_j} - \frac{\partial}{\partial x_i} \left[\varepsilon \psi \left(c \left(\alpha a_i a_j + \alpha^N \left(a_i^{N_1} a_j^{N_1} + a_i^{N_2} a_j^{N_2} \right) \right) I + a_i \frac{\partial f_j^q}{\partial q} + a_i \delta \frac{\partial f_j^p}{\partial q} \right) \frac{\partial q}{\partial x_j} \right] \quad (177)$$

By virtue of a non-singular (x_1, x_2, x_3) -space coordinate transformation

$$\eta_1 = x_j n_j - \lambda(q) t \quad , \quad \eta_2 = \eta_2(x_1, x_2, x_3, t) \quad , \quad \eta_3 = \eta_3(x_1, x_2, x_3, t) \quad (178)$$

analogous to (133), and the inverse $\{J^{-1}\}_{jk} \equiv \{e_{jk}\} / \det J$ of the associated coordinate - transformation jacobian $J \equiv \partial x / \partial \eta$, expression (177) for each t becomes²⁴

$$\frac{\partial f_j^C}{\partial x_j} = \frac{\partial f_j}{\partial x_j} - \frac{1}{\det J} \frac{\partial}{\partial \eta_\ell} \left[\varepsilon \psi e_{i\ell} \left(c \left(\alpha a_i a_j + \alpha^N \left(a_i^{N_1} a_j^{N_1} + a_i^{N_2} a_j^{N_2} \right) \right) I + a_i \frac{\partial f_j^q}{\partial q} + a_i \delta \frac{\partial f_j^p}{\partial q} \right) \frac{e_{jk}}{\det J} \frac{\partial q}{\partial \eta_k} \right] \quad (179)$$

where the coordinate-transformation metric data e_{jk} , within J , can be brought inside the partial differential operation because of the fundamental equality²⁴ $\partial e_{i\ell} / \partial \eta_\ell = 0$, for any i and with implied summation on ℓ . For each ℓ , moreover, the metric data $e_{i\ell}$ denote the components of a vector that is orthogonal to an $\eta_\ell = \text{constant}$ surface.

As delineated in Appendix A, wave-like solutions q depend upon η_1 only. For these solutions, therefore, $q = q(\eta_1)$ and (179) exhibits the upstream-bias expression

$$\mathcal{D} \equiv \frac{1}{\det J} \frac{\partial}{\partial \eta_1} \left[\varepsilon \psi e_{i1} \left(c \left(\alpha a_i a_j + \alpha^N \left(a_i^{N_1} a_j^{N_1} + a_i^{N_2} a_j^{N_2} \right) \right) I + a_i \frac{\partial f_j^q}{\partial q} + a_i \delta \frac{\partial f_j^p}{\partial q} \right) \frac{e_{j1}}{\det J} \frac{\partial q}{\partial \eta_1} \right] \quad (180)$$

for which $e_{i1} / \sqrt{(e_{\ell 1} e_{\ell 1})}$ denotes the component n_i of the wave-propagation unit vector \mathbf{n} . This expression now corresponds to a one-dimensional upstream-bias expression. This expression will, therefore, be stable when all the eigenvalues of the upstream-bias matrix

$$\mathcal{A} \equiv n_i \left(c \left(\alpha a_i a_j + \alpha^N \left(a_i^{N_1} a_j^{N_1} + a_i^{N_2} a_j^{N_2} \right) \right) I + a_i \frac{\partial f_j^q}{\partial q} + a_i \delta \frac{\partial f_j^p}{\partial q} \right) n_j \quad (181)$$

remain positive for all M and propagation directions \mathbf{n} .

E Crossflow Upstream Function α^N

For the determination of $\alpha^N = \alpha^N(M, \mathbf{n})$ from $\lambda_{3,4}(M, \mathbf{n}) \geq 0$ in (97), heed that $\mathbf{a} = \mathbf{v}$ remains perpendicular to both \mathbf{a}^{N_1} and \mathbf{a}^{N_2} . Moreover, the expressions $n_i a_i$, $n_i a_i^{N_1}$, and $n_i a_i^{N_2}$ respectively denote the vector “dot” products between the unit vector \mathbf{n} and the unit vectors \mathbf{a} , \mathbf{a}^{N_1} , and \mathbf{a}^{N_2} , hence

$$\mathbf{n} = n_i a_i \mathbf{a} + n_i a_i^{N_1} \mathbf{a}^{N_1} + n_i a_i^{N_2} \mathbf{a}^{N_2} \quad (182)$$

Accordingly,

$$\begin{aligned} n_i a_i &= \cos \bar{\theta} \\ \left(n_i a_i^{N_1} a_j^{N_1} n_j + n_i a_i^{N_2} a_j^{N_2} n_j \right)^2 &= \left[\mathbf{n} \cdot (n_i a_i^{N_1} \mathbf{a}^{N_1} + n_i a_i^{N_2} \mathbf{a}^{N_2}) \right]^2 = \\ = 1 \|n_i a_i^{N_1} \mathbf{a}^{N_1} + n_i a_i^{N_2} \mathbf{a}^{N_2}\|^2 \cos^2(90 - \bar{\theta}) &\Rightarrow n_i a_i^{N_1} a_j^{N_1} n_j + n_i a_i^{N_2} a_j^{N_2} n_j = \sin^2 \bar{\theta} \end{aligned} \quad (183)$$

where $\bar{\theta}$ denotes the angle between \mathbf{n} and \mathbf{a} .

For eigenvalue $\lambda_4 = \lambda_4(M, \mathbf{n})$ in (94), therefore, the condition $\lambda_4(M, \mathbf{n}) \geq 0$ yields

$$\alpha^N \geq g(\bar{\theta}, M) \equiv \frac{\cos \bar{\theta} \sqrt{\left(\frac{1-\delta}{2} p_E \cos \bar{\theta} M \right)^2 + \delta - \cos^2 \bar{\theta} \left(\alpha + \left(1 + \frac{1-\delta}{2} p_E \right) M \right)}}{1 - \cos^2 \bar{\theta}} \quad (184)$$

For supersonic flows with $M \geq 1 + \varepsilon_M$, $\alpha = 0$ and $\delta = 1$, hence (184) becomes

$$\alpha^N \geq g(\bar{\theta}, M) = \frac{\cos \bar{\theta} - M \cos^2 \bar{\theta}}{1 - \cos^2 \bar{\theta}} \quad (185)$$

and in particular $\alpha^N \geq g_{\max}(M)$, where $g_{\max}(M)$ denotes the maximum of $g = g(\bar{\theta}, M)$ with respect to $\bar{\theta}$, for each M . From (185), the determination of $g_{\max}(M)$ yields

$$\frac{\partial g}{\partial \bar{\theta}} = 0 \Rightarrow \cos^2 \bar{\theta} - 2M \cos \bar{\theta} + 1 = 0 \quad (186)$$

which leads to

$$\cos \bar{\theta} \Big|_{g=g_{\max}} = M - \sqrt{M^2 - 1} , \quad g_{\max}(M) = \frac{1}{2} (M - \sqrt{M^2 - 1}) \quad (187)$$

Significantly, the same solution for $g_{\max}(M)$ results from the condition $\lambda_3(M, \mathbf{n}) \geq 0$. Consequently,

$$\alpha^N \geq \frac{1}{2} (M - \sqrt{M^2 - 1}) , \quad M \geq M_M \equiv 1 + \varepsilon_M \quad (188)$$

and considering that $\lambda_4(1, \mathbf{u}) = \varepsilon_M/2$, an analogous equality is adopted for $\alpha^N(M_M)$, leading to $\alpha^N(M_M) = g_{\max}(M_M) + \varepsilon_M/2$.

For subsonic flows, a numerical analysis of $g = g(\bar{\theta}, M)$ from (185) reveals that $g(\bar{\theta}, M) < 0.3$ for all $\bar{\theta}$ and $M < M_M$. Additionally, for an isotropic acoustic upstream for vanishing M , $\alpha^N(0) = 1$ and $\partial \alpha^N / \partial M|_{M=0} = 0$, whereas for $M \geq M_M$ both α^N and its derivative with respect to M follow from (188). A smooth variation for $\alpha^N = \alpha^N(M)$ that satisfies all of these constraints is the composite spline

$$\alpha^N(M) \equiv \begin{cases} 1 + \left(\frac{3(\alpha^N(M_M) - 1)}{M_M^2} - \frac{\alpha^{N'}(M_M)}{M_M} \right) M^2 + \left(\frac{\alpha^{N'}(M_M)}{M_M^2} - \frac{2(\alpha^N(M_M) - 1)}{M_M^3} \right) M^3, & 0 \leq M < M_M; \\ \frac{1}{2} \left(1 + \frac{\varepsilon_M}{M_M - \sqrt{M_M^2 - 1}} \right) (M - \sqrt{M^2 - 1}) , & M_M \leq M \end{cases} \quad (189)$$

where superscript prime “ $'$ ” denotes differentiation with respect to M .

F Discrete Conservation

For a clear comparison between finite difference/volume schemes and the characteristics-bias finite element algorithm (109), the specific expressions for the several averages in (115)-(116) are

$$\overline{f_1}_{i+\frac{1}{2},j} \equiv \frac{f_{1,i,j+1} + 4f_{1,i,j} + f_{1,i,j-1} + f_{1,i,j+1} + 4f_{1,i,j} + f_{1,i,j-1}}{12} \quad (190)$$

and

$$\overline{f_2}_{i,j+\frac{1}{2}} \equiv \frac{f_{2,i+1,j} + 4f_{2,i,j} + f_{2,i-1,j} + f_{2,i+1,j+1} + 4f_{2,i,j+1} + f_{2,i-1,j+1}}{12} \quad (191)$$

for the flux averages,

$$\begin{aligned} & \overline{\left(\varepsilon \psi c \alpha a_1 a_\ell \frac{\Delta q}{\Delta x_\ell} \right)}_{i+\frac{1}{2},j} \equiv \\ & \frac{1}{12} \left[(q_{i+1,j+1} - q_{i,j+1}) \frac{(\ell \psi c \alpha a_1 a_1)_{i+1/2,j+1/2}}{\Delta x_1} + 2(q_{i+1,j} - q_{i,j}) \frac{(\ell \psi c \alpha a_1 a_1)_{i+1/2,j+1/2}}{\Delta x_1} \right] \\ & + \frac{1}{12} \left[(q_{i+1,j-1} - q_{i,j-1}) \frac{(\ell \psi c \alpha a_1 a_1)_{i+1/2,j-1/2}}{\Delta x_1} + 2(q_{i+1,j} - q_{i,j}) \frac{(\ell \psi c \alpha a_1 a_1)_{i+1/2,j-1/2}}{\Delta x_1} \right] \\ & + \frac{1}{12} \left[(q_{i+1,j} - q_{i+1,j-1}) \frac{3(\ell \psi c \alpha a_1 a_2)_{i+1/2,j-1/2}}{2\Delta x_2} + (q_{i+1,j+1} - q_{i+1,j}) \frac{3(\ell \psi c \alpha a_1 a_2)_{i+1/2,j+1/2}}{2\Delta x_2} \right] \\ & + \frac{1}{12} \left[(q_{i,j} - q_{i,j-1}) \frac{3(\ell \psi c \alpha a_1 a_2)_{i+1/2,j-1/2}}{2\Delta x_2} + (q_{i,j+1} - q_{i,j}) \frac{3(\ell \psi c \alpha a_1 a_2)_{i+1/2,j+1/2}}{2\Delta x_2} \right] \end{aligned} \quad (192)$$

and

$$\begin{aligned} & \overline{\left(\varepsilon \psi c \alpha a_2 a_\ell \frac{\Delta q}{\Delta x_\ell} \right)}_{i,j+\frac{1}{2}} \equiv \\ & \frac{1}{12} \left[(q_{i,j+1} - q_{i-1,j+1}) \frac{3(\ell \psi c \alpha a_2 a_1)_{i-1/2,j+1/2}}{2\Delta x_1} + (q_{i+1,j+1} - q_{i,j+1}) \frac{3(\ell \psi c \alpha a_2 a_1)_{i+1/2,j+1/2}}{2\Delta x_1} \right] \\ & + \frac{1}{12} \left[(q_{i,j} - q_{i-1,j}) \frac{3(\ell \psi c \alpha a_2 a_1)_{i-1/2,j+1/2}}{2\Delta x_1} + (q_{i+1,j} - q_{i,j}) \frac{3(\ell \psi c \alpha a_2 a_1)_{i+1/2,j+1/2}}{2\Delta x_1} \right] \\ & + \frac{1}{12} \left[(q_{i+1,j+1} - q_{i+1,j}) \frac{(\ell \psi c \alpha a_2 a_2)_{i+1/2,j+1/2}}{\Delta x_2} + 2(q_{i,j+1} - q_{i,j}) \frac{(\ell \psi c \alpha a_2 a_2)_{i+1/2,j+1/2}}{\Delta x_2} \right] \\ & + \frac{1}{12} \left[(q_{i-1,j+1} - q_{i-1,j}) \frac{(\ell \psi c \alpha a_2 a_2)_{i-1/2,j+1/2}}{\Delta x_2} + 2(q_{i,j+1} - q_{i,j}) \frac{(\ell \psi c \alpha a_2 a_2)_{i-1/2,j+1/2}}{\Delta x_2} \right] \end{aligned} \quad (193)$$

for the average streamwise acoustics contributions to $F_{1,i+\frac{1}{2},j}$ and $F_{2,i,j+\frac{1}{2}}$. The corresponding cross-flow acoustics contributions directly follow from these expressions by replacing (α, a_1, a_2) with (α^N, a_1^N, a_2^N) . The flux divergence averages are then expressed as

$$\begin{aligned} & \overline{\left(\varepsilon \psi a_1 \frac{\Delta f_\ell^q}{\Delta x_\ell} \right)}_{i+\frac{1}{2},j} \equiv \\ & \frac{1}{12} \left[(f_{1,i+1,j+1}^q - f_{1,i,j+1}^q) \frac{(\ell \psi a_1)_{i+1/2,j+1/2}}{\Delta x_1} + 2(f_{1,i+1,j}^q - f_{1,i,j}^q) \frac{(\ell \psi a_1)_{i+1/2,j+1/2}}{\Delta x_1} \right] \end{aligned}$$

$$\begin{aligned}
& + \frac{1}{12} \left[(f_{1,i+1,j-1}^q - f_{1,i,j-1}^q) \frac{(\ell\psi a_1)_{i+1/2,j-1/2}}{\Delta x_1} + 2(f_{1,i+1,j}^q - f_{1,i,j}^q) \frac{(\ell\psi a_1)_{i+1/2,j-1/2}}{\Delta x_1} \right] \\
& + \frac{1}{12} \left[(f_{2,i+1,j}^q - f_{2,i+1,j-1}^q) \frac{3(\ell\psi a_1)_{i+1/2,j-1/2}}{2\Delta x_2} + (f_{2,i+1,j+1}^q - f_{2,i+1,j}^q) \frac{3(\ell\psi a_1)_{i+1/2,j+1/2}}{2\Delta x_2} \right] \\
& + \frac{1}{12} \left[(f_{2,i,j}^q - f_{2,i,j-1}^q) \frac{3(\ell\psi a_1)_{i+1/2,j-1/2}}{2\Delta x_2} + (f_{2,i,j+1}^q - f_{2,i,j}^q) \frac{3(\ell\psi a_1)_{i+1/2,j+1/2}}{2\Delta x_2} \right] \quad (194)
\end{aligned}$$

and

$$\begin{aligned}
& \overline{\left(\varepsilon\psi a_2 \frac{\Delta f_\ell^q}{\Delta x_\ell} \right)}_{i,j+\frac{1}{2}} = \\
& \frac{1}{12} \left[(f_{1,i,j+1}^q - f_{1,i-1,j+1}^q) \frac{3(\ell\psi a_2)_{i-1/2,j+1/2}}{2\Delta x_1} + (f_{1,i+1,j+1}^q - f_{1,i,j+1}^q) \frac{3(\ell\psi a_2)_{i+1/2,j+1/2}}{2\Delta x_1} \right] \\
& + \frac{1}{12} \left[(f_{1,i,j}^q - f_{1,i-1,j}^q) \frac{3(\ell\psi a_2)_{i-1/2,j+1/2}}{2\Delta x_1} + (f_{1,i+1,j}^q - f_{1,i,j}^q) \frac{3(\ell\psi a_2)_{i+1/2,j+1/2}}{2\Delta x_1} \right] \\
& + \frac{1}{12} \left[(f_{2,i+1,j+1}^q - f_{2,i+1,j}^q) \frac{(\ell\psi a_2)_{i+1/2,j+1/2}}{\Delta x_2} + 2(f_{2,i,j+1}^q - f_{2,i,j}^q) \frac{(\ell\psi a_2)_{i+1/2,j+1/2}}{\Delta x_2} \right] \\
& + \frac{1}{12} \left[(f_{2,i-1,j+1}^q - f_{2,i-1,j}^q) \frac{(\ell\psi a_2)_{i-1/2,j+1/2}}{\Delta x_2} + 2(f_{2,i,j+1}^q - f_{2,i,j}^q) \frac{(\ell\psi a_2)_{i-1/2,j+1/2}}{\Delta x_2} \right] \quad (195)
\end{aligned}$$

which provide the contributions to $F_{1,i+\frac{1}{2},j}$ and $F_{2,i,j+\frac{1}{2}}$ from the average divergence of the flux f_ℓ^q . The corresponding contributions from the divergence of the flux f_ℓ^p are then directly obtained from these expressions by replacing f_ℓ^q with f_ℓ^p and (a_1, a_2) with $(a_1\delta, a_2\delta)$. In all these averages, the ratios $(\ell)_e/\Delta x_1$ and $(\ell)_e/\Delta x_2$ are positive numbers of order 1, for $(\ell)_e$ remains commensurate with $\sqrt{(\Delta x_1)^2 + (\Delta x_2)^2}$.

Equation (113) along with expressions (115)- (116), (190)-(195) can also be rearranged as a linear combination of two-point upstream and downstream flux differences. For instance, the linear combination $L_{1,i,j}^q$ of the differences of f_1^q along the segment $i-1, i, i+1$ on level j of elements $i - \frac{1}{2}, j - \frac{1}{2}$ and $i + \frac{1}{2}, j - \frac{1}{2}$ in Figure 11, becomes

$$\begin{aligned}
L_{1,i,j}^q = & \left[\left(f_{1,i,j}^q - f_{1,i-1,j}^q \right) \left(1 + \frac{(\ell\psi a_1)_{i-1/2,j-1/2}}{\Delta x_1} + \frac{3(\ell\psi a_2)_{i-1/2,j-1/2}}{4\Delta x_1} \right) \right. \\
& \left. \left(f_{1,i+1,j}^q - f_{1,i,j}^q \right) \left(1 - \frac{(\ell\psi a_1)_{i+1/2,j-1/2}}{\Delta x_1} + \frac{3(\ell\psi a_2)_{i+1/2,j-1/2}}{4\Delta x_1} \right) \right] \quad (196)
\end{aligned}$$

In this and the analogous linear combinations of flux differences, the numerical values of the controller ψ^h determine the combination weights of the downstream and upstream expressions. Since ψ^h remains non-negative, these equations induce an upstream bias on the appropriate flux differences, for the weight on the upstream flux difference is greater than the weight on the downstream difference. For example, for $a_2 = 0$ and $a_1 = 1$ then $(\ell)_e = \Delta x_1$ and the weight on the downstream flux difference vanishes altogether for $\psi = 1$. As a result, the finite element weak statement (112) generates consistent variable-upstream-bias discrete equations that correspond to an upstream-bias discretization of the original Euler system (1).

A CFD Euler Solver from a Physical Acoustics-Convection Flux Jacobian Decomposition

JOE IANNELLI*

Department of Mechanical & Aerospace Engineering and Engineering Science
The University of Tennessee, 315 Perkins Hall, Knoxville, TN 37996-2030, U.S.A.

SUMMARY

This paper introduces a continuum, i.e. non-discrete, upstream-bias formulation that rests on the physics and mathematics of acoustics and convection. The formulation induces the upstream bias at the differential-equation level, within a characteristics-bias system associated with the Euler equations with general equilibrium equations of state. For low subsonic Mach numbers, this formulation returns a consistent upstream-bias approximation for the non-linear acoustics equations. For supersonic Mach numbers, the formulation smoothly becomes an upstream-bias approximation of the entire Euler flux. With the objective of minimizing induced artificial diffusion, the formulation non-linearly induces upstream-bias essentially locally in regions of solution discontinuities, whereas it decreases the upstream-bias in regions of solution smoothness. The discrete equations originate from a finite element discretization of the characteristic-bias system and are integrated in time within a compact block tri-diagonal matrix statement by way of an implicit non-linearly stable Runge-Kutta algorithm for stiff systems. As documented by several computational results that reflect available exact solutions, the acoustics-convection solver induces low artificial diffusion and generates essentially non-oscillatory solutions that automatically preserve a constant enthalpy as well as smoothness of both enthalpy and mass flux across normal shocks.

No. of Figures: 24. No. of Tables: 1. No. of References: 13.

KEY WORDS: CFD; upwind; artificial diffusion; acoustics; convection; finite elements; implicit integration

1 Introduction

This paper introduces for the Euler equations, with general equilibrium equations of state, a stable and consistent upstream-bias algorithm that rests on a new Flux Jacobian Decomposition (FJD) formulation, features the simplicity of a flux vector splitting formulation and accommodates an implicit solver. The algorithm induces minimal diffusion, naturally incorporates a finite element discretization and uniquely generates the upstream bias directly at the differential equation level before and independently of any discrete approximation on specified grids. As one of its important features, the algorithm combines the mathematics of upwind algorithms with the physics of acoustics and convection, the wave propagation mechanisms within gas dynamic flows.

Most finite element, difference, and volume algorithms have remained largely independent from the physics of acoustics and convection. The dissipation mechanisms within these algorithms, furthermore, have been developed at the discrete level in connection with a specific grid.

Several finite element Euler solvers have either utilized modifications of the test space, e.g. SUPG¹, or introduced Taylor's series based dissipation terms, e.g. TWS², to generate stable algorithms. The mathematical developments in these fundamental contributions have remained independent from characteristics theory.

Most characteristics upwind schemes have been implemented through finite difference and finite volume discrete approximations³. Roe's approximate Riemann solver⁴ remains an upwind procedure with a significant physics content. The associated operation count, on the other hand, exceeds that of a flux vector splitting formulation.

* Associate Professor, jiannell@utk.edu. Joe Iannelli, Dept. of Mechanical & Aerospace Engineering and Engineering Science, The University of Tennessee, 315 Perkins Hall, Knoxville, TN 37996-2030, U.S.A.

VanLeer's original simple flux vector splitting and the many variants developed thereafter⁵ essentially rely on Mach-number dependent polynomials to generate flux components, each featuring jacobian eigenvalues with uniform algebraic signs. As such, these fundamental mathematical developments remain independent from the physics of acoustics and convection.

As a spin-off from these studies and presented as a new perfect-gas flux vector splitting, Liou's and Steffen's procedure⁶ employs an ad-hoc advection velocity along with flux components with convection and pressure physical meanings. An analogous method was introduced earlier by this author⁷ and the essentially non-oscillatory results from both methods bear out the advantages of employing flux components with clear physical significance.

The eigenvalues of the various convection and pressure fluxes in these methods, however, either approach zero or remain substantially less than the speed of sound for decreasing Mach number. Neither method has therefore generated a physically consistent upstream-bias approximation of the acoustics limit of the Euler equations in the low-Mach number regime. No single decomposition of the Euler flux, in fact, contains separate components that respectively correspond to the physics of acoustics and convection.

In this paper, a new upstream-bias formulation is developed that is based on a decomposition of the Euler flux vector jacobian into matrix components. This formulation encompasses, unifies and generalizes upwind algorithms, including Flux Vector Splitting and Flux Difference Splitting developments. This formulation develops the upstream-bias approximation directly at the differential equation level, before any discretization. The method results in a "companion" characteristics-bias system that is associated with the Euler equations and contains an upstream-bias differential expression. The characteristics-bias system features a characteristics flux that generalizes in the continuum the traditional numerical fluxes of upwind schemes. The acoustic-convection upstream algorithm then results from a specific decomposition of the flux vector jacobian into genuine acoustics and convection components, for a physically consistent upstream approximation of coupled acoustic and convection wave propagation.

A traditional centered discretization of the acoustics-convection characteristics-bias system then automatically generates a coherent upstream discrete approximation of the governing Euler equations. This approximation, moreover, reduces to a consistent upstream approximation of the acoustics equations, for vanishing Mach number, which addresses the challenging problem of calculating low-Mach-number flows. Finite difference, volume, or element procedures can be used to discretize the characteristics-bias system. The algorithm in this paper has used a finite element discretization, which also leads naturally and automatically to consistent boundary differential equations and a new outlet pressure boundary condition that does not require any algebraic extrapolation of variables. The resulting discrete equations correspond to an essentially centered discretization in the form of a non-linear combination of upstream diffusive and downstream anti-diffusive flux differences, with greater bias on the upstream diffusive flux difference. This formulation, furthermore, directly accommodates an implicit solver, for it is very easy to determine the required jacobian matrices.

With the objective of minimizing induced artificial diffusion, the characteristics-bias flux non-linearly induces upstream-bias essentially locally in regions of solution discontinuities, whereas it decreases the upstream-bias in regions of solution smoothness. This variable diffusion is automatically adjusted at each discretization node by a new controller, also introduced in this paper. This controller depends on local solution-slope jumps and varies the combination weights on the upstream and downstream fluxes, within the discrete equations.

The operation count for this algorithm is comparable to that of a simple flux vector splitting algorithm. The developments in this study have employed basic two-noded cells, which has thus led to a block tridiagonal matrix system, for the implicit formulation. To determine the ultimate accuracy of linear approximations of fluxes within two-noded cells, for a computationally efficient

implementation, this study employs no MUSCL-type local extrapolation of dependent variables.

This paper is organized in 9 sections. After the introductory remarks in Section 1, Section 2 presents the governing equations and Sections 3 develops the Flux Jacobian Decomposition formulation. Section 4 presents the decomposition of the Euler flux jacobian into genuinely physical acoustic and convection components, followed in Section 5 by the determination of the corresponding upstream-bias stability eigenvalues. Section 6 details the finite element spatial discretization, along with the new pressure boundary condition and solution dependent control of upstream diffusion, and Section 7 delineates the non-linearly stable implicit Runge-Kutta time integration. The computational results are discussed in Section 8, with concluding remarks presented in Section 9.

2 Governing Equations

2.1 Euler System

With respect to an inertial reference frame, the quasi-1D Euler conservation law system³ is:

$$\frac{\partial q}{\partial t} + \frac{\partial f(q)}{\partial x} = \phi \quad (1)$$

where the independent variable (x, t) varies in the domain $D \equiv \Omega \times [t_o, T]$, $\Omega \equiv [a, b]$. This system consists of the continuity, momentum and total-energy equations, and the arrays $q = q(x, t)$, $f = f(q)$ and $\phi = \phi(x, q)$ are defined as

$$q \equiv \begin{Bmatrix} \rho \\ m \\ E \end{Bmatrix}, \quad f(q) \equiv \begin{Bmatrix} m \\ \frac{m^2}{\rho} + p \\ \frac{m}{\rho}(E + p) \end{Bmatrix}, \quad \phi \equiv -\frac{m}{\rho A/A_*} \frac{dA/A_*}{dx} \begin{Bmatrix} \rho \\ m \\ E + p \end{Bmatrix} \quad (2)$$

where ρ , m , E respectively denote static density and volume-specific linear momentum and total energy; the eulerian flow velocity u is then defined as $u \equiv m/\rho$. The terms p , $A = A(x)$ and A_* respectively indicate static pressure, area of the flow duct cross-section, and constant upstream-flow reference throat area.

2.2 Equilibrium Equation of State, Pressure Derivatives, Speed of Sound

For any homogeneous equilibrium gas, pressure depends upon two other thermodynamic variables.⁸ They are density ρ and mass-specific internal energy ϵ , in this case, since they are readily available from the Euler system (1): ρ directly from the continuity equation in the system, and ϵ from q as

$$\epsilon \equiv \frac{E}{\rho} - \frac{1}{2\rho^2}m^2 \quad (3)$$

The pressure equation of state thus becomes

$$p = p(\rho, \epsilon) = p \left(\rho, \frac{E}{\rho} - \frac{1}{2\rho^2}m^2 \right) \quad (4)$$

The jacobian derivatives of p with respect to q , for the jacobian $\partial f / \partial q$ of $f(q)$, are not all independent of one another. The derivatives of (4) with respect to m and E in fact satisfy the constraint

$$\frac{\partial p}{\partial m} \Big|_{\rho, E} = -\frac{m}{\rho} \frac{\partial p}{\partial E} \Big|_{\rho, m} \quad (5)$$

as obtained by expressing the derivatives of p with respect to m and E in terms of the thermodynamic derivative of p with respect to ϵ , from the first expression in (4). In the following sections, for simplicity, the abridged notation

$$p_\rho \equiv \left. \frac{\partial p}{\partial \rho} \right|_{m,E} , \quad p_m \equiv \left. \frac{\partial p}{\partial m} \right|_{\rho,E} , \quad p_E \equiv \left. \frac{\partial p}{\partial E} \right|_{\rho,m} \quad (6)$$

will denote the jacobian derivatives of pressure. The particular perfect-gas expressions for (4) follow from the internal energy and equation of state

$$\epsilon = c_v T = \frac{R}{\gamma - 1} T , \quad p = \rho R T \quad (7)$$

for this type of gas, where c_v , T , R and γ respectively denote the constant-volume specific heat, static temperature, gas constant and specific-heat ratio. The elimination of T from these two expressions and use of (3) leads to the following familiar expressions for the equation of state for p in terms of q

$$p = (\gamma - 1) \rho \epsilon = (\gamma - 1) \left(E - \frac{1}{2\rho} m^2 \right) \quad (8)$$

The square of the speed of sound c for general equilibrium equations of state can be expressed⁹ as

$$c^2 \equiv \left. \frac{\partial p}{\partial \rho} \right|_S = p_\rho + p_E \left(\frac{E + p}{\rho} - \frac{m^2}{\rho^2} \right) \quad (9)$$

in terms of the jacobian partial derivatives of p . With this result, the mass-specific total enthalpy H depends on q as

$$H \equiv \frac{E + p}{\rho} = \frac{1}{p_E} \left(c^2 \left(1 + p_E M^2 \right) - p_\rho \right) \quad (10)$$

where $M \equiv \|u\|/c$ denotes the Mach number.

2.3 Characteristics Analysis

For general equilibrium pressure equations of state (4), the characteristic speeds associated with the Euler equations, that is the eigenvalues of the flux vector jacobian

$$\frac{\partial f(q)}{\partial q} = \begin{pmatrix} 0 & 1 & 0 \\ -\frac{m^2}{\rho^2} + p_\rho & \frac{2m}{\rho} + p_m & p_E \\ -\frac{m}{\rho^2} (E + p) + \frac{m}{\rho} p_\rho & \frac{E + p}{\rho} + \frac{m}{\rho} p_m & \frac{m}{\rho} (1 + p_E) \end{pmatrix} \quad (11)$$

have been exactly determined in closed form as

$$\lambda_1 = u , \quad \lambda_{2,3} = u \pm \left(p_\rho + p_E \left(\frac{E + p}{\rho} - \frac{m^2}{\rho^2} \right) \right)^{1/2} \quad (12)$$

These eigenvalues correspond to the slopes of the characteristics, as portrayed in Figure 1 for representative hypersonic, supersonic, sonic, and subsonic

Of interest, eigenvalues $\lambda_{2,3}$ directly incorporate a sound speed expression that coincides with the isentropic partial derivative of pressure (9). Through (9), therefore, these equilibrium-gas eigenvalues become

$$\lambda_1^E = u , \quad \lambda_{2,3}^E = u \pm c \quad (13)$$

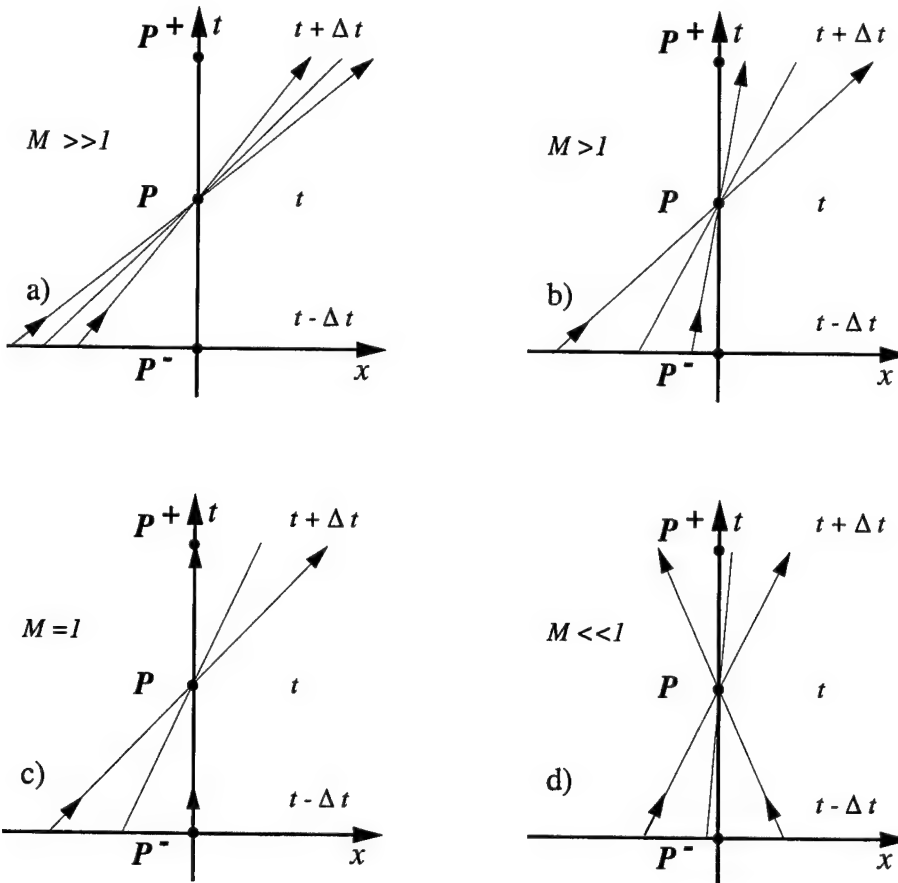


Figure 1: Characteristics: a) Hypersonic, b) Supersonic, c) Sonic, d) Subsonic

which have the same familiar form as the perfect-gas eigenvalues.

Figure 1 shows the characteristics in a suitable neighborhood of a flow field point P in a (t, x) plane. An interesting geometric difference among supersonic, sonic, and subsonic flows is that a time axis through P is respectively outside, on the boundary, and inside the domain of dependence and range of influence of point P . Wave propagation for supersonic flows essentially occurs by convection, mono-axially from upstream to downstream of P ; the sonic case becomes a limiting case; for subsonic flows, instead, wave propagation occurs by both convection and acoustics, bi-modally from both upstream and downstream toward P ; for vanishing Mach number, wave propagation is essentially acoustic.

Since gas dynamic wave propagation physically occurs by acoustics and convection, the upstream CFD algorithm in this paper mathematically models this coupled acoustic-convection wave propagation. The algorithm identifies the genuine convection and acoustics components within the flux jacobian and then establishes a physically consistent upstream approximation for each of these components.

2.4 Non-Linear Acoustics Equations

The Euler equations contain the acoustics equations for vanishing Mach numbers. Identification of these equations yields the acoustics component of the Euler flux jacobian for any Mach number. Upon writing momentum m in terms of the Mach number M as $m = \rho c M u / |u|$ and using the

energy pressure derivative identity (5), the Euler system (1) becomes

$$\begin{aligned} \frac{\partial \rho}{\partial t} + \frac{\partial m}{\partial x} + cM \frac{u}{|u|} \frac{\rho}{A} \frac{dA}{dx} &= 0 \\ \frac{\partial m}{\partial t} + p_\rho \frac{\partial \rho}{\partial x} + p_E \frac{\partial E}{\partial x} + cM \frac{u}{|u|} \left[(2 - p_E) \frac{\partial m}{\partial x} - \frac{m}{\rho} \frac{\partial \rho}{\partial x} + \frac{m}{A} \frac{dA}{dx} \right] &= 0 \\ \frac{\partial E}{\partial t} + \frac{E + p}{\rho} \frac{\partial m}{\partial x} + cM \frac{u}{|u|} \left[\rho \frac{\partial}{\partial x} \left(\frac{E + p}{\rho} \right) + \frac{E + p}{A} \frac{dA}{dx} \right] &= 0 \end{aligned} \quad (14)$$

and for a vanishing Mach number, these equations reduce to the non-linear acoustics system

$$\frac{\partial}{\partial t} \begin{pmatrix} \rho \\ m \\ E \end{pmatrix} + \begin{pmatrix} 0 & 1 & 0 \\ p_\rho & 0 & p_E \\ 0 & \frac{E + p}{\rho} & 0 \end{pmatrix} \frac{\partial}{\partial x} \begin{pmatrix} \rho \\ m \\ E \end{pmatrix} = 0 \Rightarrow \frac{\partial q}{\partial t} + A^{a_0} \frac{\partial q}{\partial x} = 0 \quad (15)$$

where A^{a_0} denotes the zero-Mach-number acoustics matrix. The dependent variables in these equations correspond to those in a flow field that originates from slight perturbations to an otherwise quiescent field.

Heed that the energy equation toward steady state, in this case, is no longer linearly independent from the continuity equation. This phenomenon directly explains the widely reported convergence difficulties experienced in the CFD simulation of incompressible, i.e. low-Mach-number, flows with a compressible flow formulation.

By virtue of the total enthalpy expression (10), the matrix A^{a_0} becomes

$$A^{a_0} = \begin{pmatrix} 0 & 1 & 0 \\ p_\rho & 0 & p_E \\ 0 & \frac{c^2 - p_\rho}{p_E} & 0 \end{pmatrix} \quad (16)$$

with eigenvalues

$$\lambda_1^{a_0} = 0, \quad \lambda_{2,3}^{a_0} = \pm c \quad (17)$$

Where c corresponds to the zero-Mach-number isentropic speed of sound (9). With $\lambda_1^{a_0} = 0$, the propagation of (acoustic) waves governed by this system, therefore, corresponds to an isentropic process with negligible flow kinetic energy.

Equations (15) contain the important expressions

$$\frac{\partial E}{\partial x} = \frac{c^2 - p_\rho}{p_E} \frac{\partial \rho}{\partial x}, \quad \frac{\partial \rho}{\partial x} \frac{p_E}{c^2 - p_\rho} \frac{\partial E}{\partial x} \quad (18)$$

which result from the momentum equation by expressing p_ρ therein using (9) as

$$\begin{aligned} \frac{\partial m}{\partial t} &= -\frac{\partial p}{\partial x} = -p_\rho \frac{\partial \rho}{\partial x} - p_E \frac{\partial E}{\partial x} = \\ &= -\left(\frac{\partial p}{\partial \rho} \Big|_S - p_E \frac{E + p}{\rho} \right) \frac{\partial \rho}{\partial x} - p_E \frac{\partial E}{\partial x} = -\frac{\partial p}{\partial \rho} \Big|_S \frac{\partial \rho}{\partial x} - p_E \left(\frac{\partial E}{\partial x} - \frac{E + p}{\rho} \frac{\partial \rho}{\partial x} \right) \end{aligned} \quad (19)$$

For an isentropic flow $p = p(\rho)$, hence the first rhs term in (19) equals $\frac{\partial p}{\partial x}$. The second rhs term must consequently vanish, which returns results (18), after using (10). These results will conveniently simplify the acoustics-convection upstream formulation in Sections 4.2-4.3.

3 Non-Discrete Upstream-Bias Approximation

The non-discrete, i.e. continuum or before discretization, upstream-bias approximation of the Euler equations derives from a characteristics-bias integral statement associated with (1). The prototype integral statement is

$$\int_{\hat{\Omega}} \hat{w} \left(\frac{\partial q}{\partial t} - \phi + \frac{\partial f(q)}{\partial x} \right) d\Omega = 0 \quad (20)$$

which is equivalent to the governing system (1) for arbitrary subdomains $\hat{\Omega} \subset \Omega$ and arbitrary test functions \hat{w} with compact support in $\hat{\Omega}$. The characteristic-bias integral is then defined as

$$\int_{\hat{\Omega}} \hat{w} \left(\frac{\partial q}{\partial t} - \phi + \frac{\partial f^C}{\partial x} \right) d\Omega = 0 \quad (21)$$

where f^C corresponds to a characteristics-bias flux that automatically induces within (21) an upstream-bias approximation for the Euler flux divergence $\frac{\partial f}{\partial x}$.

3.1 Flux Jacobian Decomposition and Upstream-Bias Integral Average

To develop the flux f^C , consider first the flux jacobian decomposition (FJD) into L contributions

$$\frac{\partial f}{\partial q} = \sum_{\ell=1}^L \alpha_{\ell} A_{\ell} \quad \Rightarrow \quad \frac{\partial f}{\partial x} = \sum_{\ell=1}^L \alpha_{\ell} A_{\ell} \frac{\partial q}{\partial x} \quad (22)$$

where A_{ℓ} corresponds to a flux-jacobian matrix component with uniform-sign eigenvalues and α_{ℓ} denotes a linear-combination function, possibly depending upon q .

An integral average of the Euler flux divergence $\frac{\partial f}{\partial x}$ as expressed through decomposition (22) becomes

$$\int_{\hat{\Omega}} \hat{w} \frac{\partial f}{\partial x} d\Omega = \int_{\hat{\Omega}} \sum_{\ell=1}^L \hat{w} \alpha_{\ell} A_{\ell} \frac{\partial q}{\partial x} d\Omega \quad (23)$$

The flux f^C is therefore defined by way of an upstream-bias integral average as

$$\int_{\hat{\Omega}} \hat{w} \frac{\partial f^C}{\partial x} d\Omega = \int_{\hat{\Omega}} \sum_{\ell=1}^L (\hat{w} + \psi \delta_{\ell} \hat{w}) \alpha_{\ell} A_{\ell} \frac{\partial q}{\partial x} d\Omega \quad (24)$$

where the rhs integral provides an upstream bias for each matrix component within the FJD in (22).

The positive ψ in (24), $0 < \psi < 1$, stands for a new “upstream-bias” controller, which automatically adjusts the amount of induced upstream-bias diffusion, depending on local solution non-smoothness, as introduced and detailed in Section 6.3. The variation $\delta_{\ell} \hat{w}$ induces the appropriate upstream-bias for the test function \hat{w} for each “ ℓ ” component within (24). Depending on the physical significance, magnitude and algebraic sign of the eigenvalues of A_{ℓ} , the variation $\delta_{\ell} \hat{w}$ can vanish or become algebraically positive or negative, which corresponds to an upstream bias respectively in the negative or positive sense of the x -axis.

3.2 Characteristics-Bias Flux

The variation $\delta_{\ell} \hat{w}$ in (24) becomes

$$\delta_{\ell} \hat{w} = \frac{\partial \hat{w}}{\partial x} \delta_{\ell} x = \frac{\partial \hat{w}}{\partial x} a_{\ell} \varepsilon \quad , \quad a_{\ell} \varepsilon = \delta_{\ell} x \quad (25)$$

where ε denotes a local positive length scale, while the direction cosine a_ℓ can equal 0 or $+1, -1$, possibly also depending upon q .

With these specifications, the upstream-bias integral average (24) becomes

$$\int_{\widehat{\Omega}} \widehat{w} \frac{\partial f^C}{\partial x} d\Omega = \int_{\widehat{\Omega}} \widehat{w} \frac{\partial f}{\partial x} d\Omega + \int_{\widehat{\Omega}} \varepsilon \psi \frac{\partial \widehat{w}}{\partial x} \sum_{\ell=1}^L a_\ell \alpha_\ell A_\ell \frac{\partial q}{\partial x} d\Omega \quad (26)$$

Considering that \widehat{w} has compact support in $\widehat{\Omega}$, it vanishes on the boundary $\partial\widehat{\Omega}$ of $\widehat{\Omega}$. As a result, integrating (26) by parts generates

$$\int_{\widehat{\Omega}} \widehat{w} \left[\frac{\partial f^C}{\partial x} - \frac{\partial f}{\partial x} + \frac{\partial}{\partial x} \left(\varepsilon \psi \sum_{\ell=1}^L a_\ell \alpha_\ell A_\ell \frac{\partial q}{\partial x} \right) \right] d\Omega = 0 \quad (27)$$

which contains no boundary integrals. Since this integral must vanish for arbitrary test functions \widehat{w} and domains $\widehat{\Omega}$, its integrand must identically equal zero, which generates the following expression for the divergence of the characteristics-bias flux f^C

$$\frac{\partial f^C}{\partial x} = \frac{\partial f}{\partial x} - \frac{\partial}{\partial x} \left(\varepsilon \psi \sum_{\ell=1}^L a_\ell \alpha_\ell A_\ell \frac{\partial q}{\partial x} \right) \quad (28)$$

This expression exhibits an upstream-bias artificial diffusion, in the form of a second-order differential expression with matrix

$$\mathcal{A} \equiv \sum_{\ell=1}^L a_\ell \alpha_\ell A_\ell \quad (29)$$

For physical consistency of the upstream bias in (24)-(28) and associated mathematical stability of the corresponding second-order differential expression, all the eigenvalues of this upstream matrix must be positive. This requirement becomes a fundamental upstream-bias stability condition.

For 2-D and 3-D flows, the version of the characteristics-bias flux follows as a multi-dimensional generalization of (22)-(29) as

$$\frac{\partial f_j}{\partial x_j} = \sum_{\ell=1}^L \alpha_\ell A_{\ell j} \frac{\partial q}{\partial x_j} \quad , \quad \delta_\ell \widehat{w} = \frac{\partial \widehat{w}}{\partial x_j} \delta_\ell x_j = \frac{\partial \widehat{w}}{\partial x_j} a_{j\ell} \varepsilon \quad (30)$$

and

$$\frac{\partial f_j^C}{\partial x_j} = \frac{\partial f_j}{\partial x_j} - \frac{\partial}{\partial x_i} \left(\varepsilon \psi \sum_{\ell=1}^L a_{i\ell} \alpha_\ell A_{\ell j} \frac{\partial q}{\partial x_j} \right) \quad , \quad \mathcal{A} \equiv \omega_i \left(\sum_{\ell=1}^L a_{i\ell} \alpha_\ell A_{\ell j} \right) \omega_j \quad (31)$$

with $1 \leq i, j \leq 2$, for 2-D, and $1 \leq i, j \leq 3$, for 3-D. In these expressions, $a_{i\ell}$ now denotes the i^{th} direction cosine of a unit vector \mathbf{a}_ℓ along the principal wave-propagation direction of wave “ ℓ ”, and ω_i indicates the i^{th} direction cosine of a unit vector $\boldsymbol{\omega}$ along an arbitrary wave-propagation direction. The multi-dimensional acoustics-convection form of (31) is being completed, but will be detailed soon in a companion paper, to keep the length of each of these two papers within an appropriate size.

The continuum expression (28), or (31), for the divergence of the characteristics-bias flux constitutes a non-discrete generalization of the various numerical-flux formulae employed in several CFD upwind schemes. It encompasses, generalizes, and unifies flux-vector and flux-difference schemes as shown by the following representative examples.

3.2.1 van Leer's Formulation and Flux Vector Splitting

Consider the van Leer's formulation as a representative Flux Vector Splitting (FVS). In this formulation, the inviscid flux f is "split" as

$$f = f^{VL+} + f^{VL-} \quad (32)$$

where the jacobian matrices of f^{VL+} and f^{VL-} respectively possess non-negative and non-positive eigenvalues.

The FJD expression (22) encompasses (32) with $L = 2$ as

$$\sum_{\ell=1}^L \alpha_{\ell} A_{\ell} = \frac{\partial f^{VL+}}{\partial q} + \frac{\partial f^{VL-}}{\partial q} , \quad \alpha_1 = 1 , \quad \alpha_2 = 1 \quad (33)$$

The corresponding characteristics-bias flux divergence for van Leer's FVS accrues from (28) with $\psi = 1$, $a_1 = 1$, $a_2 = -1$ as

$$\frac{\partial f^C}{\partial x} = \frac{\partial f}{\partial x} - \frac{\partial}{\partial x} \left(\varepsilon \left(\frac{\partial f^{VL+}}{\partial q} - \frac{\partial f^{VL-}}{\partial q} \right) \frac{\partial q}{\partial x} \right) = \frac{\partial f}{\partial x} - \frac{\partial}{\partial x} \left(\varepsilon \left(\frac{\partial f^{VL+}}{\partial x} - \frac{\partial f^{VL-}}{\partial x} \right) \right) \quad (34)$$

which generalizes in the continuum the traditional numerical flux formulae for FVS constructions.

The associated upstream matrix \mathcal{A} is

$$\mathcal{A} = \frac{\partial f^{VL+}}{\partial q} - \frac{\partial f^{VL-}}{\partial q} \quad (35)$$

The upstream-bias stability condition, however, is not automatically satisfied, even though each of the two matrices $\left(\frac{\partial f^{VL+}}{\partial q} \right)$ and $\left(-\frac{\partial f^{VL-}}{\partial q} \right)$ has positive eigenvalues. This stability condition is not unconditionally satisfied because the sum of two positive-eigenvalue matrices does not necessarily yield a matrix with positive eigenvalues. As an example consider the following matrix sum of two positive-eigenvalue matrices

$$\begin{pmatrix} 2 & \sigma \\ 3 & 6 \end{pmatrix} = \begin{pmatrix} 1 & 0 \\ 3 & 2 \end{pmatrix} + \begin{pmatrix} 1 & \sigma \\ 0 & 4 \end{pmatrix} \quad (36)$$

where σ is a real number. One of the eigenvalues of this matrix sum is negative for $\sigma > 4$. For instance, for $\sigma = 7$ the eigenvalues are $+9$ and -1 .

Most likely, however, (35) satisfies the upstream-bias stability condition for most of the flow conditions considered in the technical literature, in view of the stable results reported. For subsonic flows, each of the two flux vector components in (32) remains unrelated to the physics of acoustics or convection. On the other hand, (32) is computationally advantageous, for it calls for the discretization of simple flux-vector components.

3.2.2 Roe's Formulation and Flux Difference Splitting

Consider next Roe's formulation as a representative Flux Difference Splitting (FDS) development. In this formulation, the inviscid flux jacobian of f is "split" as

$$\frac{\partial f}{\partial q} = X \Lambda^+ X^{-1} + X \Lambda^- X^{-1} \quad (37)$$

where X and $\Lambda = \Lambda^+ + \Lambda^-$ denote the right eigenvector matrix and eigenvalue diagonal matrix of the jacobian, all evaluated at special average values of q , with Λ^+ and Λ^- respectively containing non-negative and non-positive eigenvalues. The matrices at the rhs of (37), therefore, will respectively possess non-negative and non-positive eigenvalues.

The FJD expression (22) encompasses (37) with $L = 2$ as

$$\sum_{\ell=1}^L \alpha_\ell A_\ell = X \Lambda^+ X^{-1} + X \Lambda^- X^{-1} , \quad \alpha_1 = 1 , \quad \alpha_2 = 1 \quad (38)$$

The corresponding characteristics-bias divergence for Roe's formulation accrues from (28) with $\psi = 1$, $a_1 = 1$, $a_2 = -1$ as

$$\frac{\partial f^C}{\partial x} = \frac{\partial f}{\partial x} - \frac{\partial}{\partial x} \left(\varepsilon \left(X \Lambda^+ X^{-1} - X \Lambda^- X^{-1} \right) \frac{\partial q}{\partial x} \right) = \frac{\partial f}{\partial x} - \frac{\partial}{\partial x} \left(\varepsilon X \left(\Lambda^+ - \Lambda^- \right) X^{-1} \frac{\partial q}{\partial x} \right) \quad (39)$$

which generalizes in the continuum the traditional numerical flux formulae for FDS constructions.

The associated upstream matrix \mathcal{A} is

$$\mathcal{A} = X \left(\Lambda^+ - \Lambda^- \right) X^{-1} \quad (40)$$

which has non-negative eigenvalues and therefore automatically satisfies the upstream-bias stability condition for any flow state for which no eigenvalue vanishes. The discretization of (39) calls for more computational operations than (34), while each of the two rhs components in (37) lumps into one matrix the matrices representative of the distinct acoustics and convection wave propagation mechanisms. On the other hand, numerous numerical results bear out the accuracy of an FDS formulation.

4 Acoustics-Convection Flux Jacobian Decomposition

The acoustics-convection flux jacobian decomposition consists of components that genuinely model the physics of acoustics and convection. These components combine the computational simplicity of FVS with the accuracy and stability of FDS and also feature eigenvalues with uniform algebraic sign. This formulation eliminates the unstable linear-dependence problem in steady low-Mach-number flows and satisfies by design the upstream-bias stability condition. As the Mach number increases, the formulation smoothly approaches and then becomes an upstream-bias approximation of the entire flux divergence, along one single direction.

4.1 Convection and Pressure-Gradient Components

The flux divergence $\frac{\partial f}{\partial x}$ can be decomposed into convection and pressure-gradient components as

$$\frac{\partial f}{\partial x} = \frac{\partial f^q}{\partial x} + \frac{\partial f^p}{\partial x} \quad (41)$$

where f^q and f^p respectively denote the convection and pressure fluxes, defined as

$$f^q(q) \equiv \begin{Bmatrix} m \\ \frac{m^2}{\rho} \\ \frac{m}{\rho} (E + p) \end{Bmatrix} = \frac{m}{\rho} \cdot \begin{Bmatrix} \rho \\ m \\ E + p \end{Bmatrix} , \quad f^p \equiv \begin{Bmatrix} 0 \\ p \\ 0 \end{Bmatrix} \quad (42)$$

For supersonic flows, the Euler eigenvalues (13), associated with $\frac{\partial f}{\partial x}$ all have the same algebraic sign and the entire flux divergence can be upstream approximated along one single direction. For subsonic flows these eigenvalues have mixed algebraic sign and an upstream approximation for the flux divergence along one single direction remains inconsistent with the two-way propagation of acoustic waves. Without the pressure gradient in the momentum equation, however, the corresponding flux-jacobian eigenvalues all have the same algebraic sign⁹ and the resulting convection flux divergence can then be upstream approximated along one single direction. The flux divergence can thus be decomposed as the linear combination

$$\frac{\partial f}{\partial x} = \left[\frac{\partial f^q}{\partial x} + \beta \frac{\partial f^p}{\partial x} \right] + \left[(1 - \beta) \frac{\partial f^p}{\partial x} \right], \quad 0 \leq \beta \leq 1 \quad (43)$$

where the positive pressure-gradient partition function β can be chosen in such a way that all the eigenvalues of each of the two components between brackets in (43) keep the same algebraic sign for all Mach numbers. In this manner, these entire components can be upstream approximated along single directions. This choice for β is possible because the eigenvalues of a matrix are continuous functions of the matrix entries¹⁰ and hence all the eigenvalues for the components in (43) will continuously depend upon β . The function β will gradually increase toward 1 for increasing Mach number, so that an upstream approximation for the components in (43) smoothly approaches and then becomes an upstream approximation for the entire $\frac{\partial f}{\partial x}$ along one single direction. Decomposition (43) is thus used for an upstream approximation of the flux divergence for subsonic and supersonic flows.

For low and vanishing Mach numbers, decomposition (43), however, is insufficient for an accurate upstream modeling of acoustic waves. For a Mach number that approaches zero, the Euler eigenvalues (13) can all keep the same algebraic sign only if the sound speed contribution vanishes, which corresponds to a vanishing pressure gradient contribution and hence β approaching zero.⁹ But for β approaching zero, the eigenvalues associated with the components in (43) approach the eigenvalues of the jacobians

$$\frac{\partial f^q(q)}{\partial q} = \begin{pmatrix} 0 & , & 1 & , & 0 \\ -\frac{m^2}{\rho^2} & , & \frac{2m}{\rho} & , & 0 \\ -\frac{m}{\rho^2} (E + p) + \frac{m}{\rho} p_\rho & , & \frac{E + p}{\rho} + \frac{m}{\rho} p_m & , & \frac{m}{\rho} (1 + p_E) \end{pmatrix} \quad (44)$$

and

$$\frac{\partial f^p}{\partial q} = \begin{pmatrix} 0 & , & 0 & , & 0 \\ p_\rho & , & p_m & , & p_E \\ 0 & , & 0 & , & 0 \end{pmatrix} \quad (45)$$

Using the pressure-derivative identity (5) the eigenvalues of these jacobians respectively are

$$\lambda_{1,2}^q = \frac{m}{\rho}, \quad \lambda_3^q = \frac{m}{\rho} (1 + p_E) \quad (46)$$

and

$$\lambda_{1,2}^p = 0, \quad \lambda_3^p = p_m = -\frac{m}{\rho} p_E \quad (47)$$

which certainly all keep the same algebraic sign, but for vanishing Mach number remain far less than the dominant speed of sound c . For low Mach numbers, therefore, an upstream approximation for the components in (43) would inaccurately model the physics of acoustics. This difficulty is resolved by further decomposing the pressure gradient in (43) in terms of a genuine acoustic component, for accurate upstream modeling of acoustic waves.

4.2 Acoustic Components

Following the acoustic equations (15), the flux divergence $\frac{\partial f}{\partial x}$ can be alternatively decomposed for arbitrary Mach numbers and corresponding dependent variables ρ , m , and E as

$$\frac{\partial f}{\partial x} = \frac{\partial f^q}{\partial x} + \frac{\partial f^p}{\partial x} = \frac{\partial f^q}{\partial x} + (A^a + A^{nc}) \frac{\partial q}{\partial x} \quad (48)$$

In this decomposition, the matrices A^a and A^{nc} are defined as

$$A^a \equiv \begin{pmatrix} 0 & 1 & 0 \\ p_\rho & 0 & p_E \\ 0 & \frac{c^2 - p_\rho}{p_E} & 0 \end{pmatrix}, \quad A^{nc} \equiv \begin{pmatrix} 0 & -1 & 0 \\ 0 & \frac{p_m}{c^2 - p_\rho} & 0 \\ 0 & -\frac{c^2 - p_\rho}{p_E} & 0 \end{pmatrix} \quad (49)$$

Indeed, in particular, that no flux component of $f(q)$ exists, of which the jacobian equals A^a . The eigenvalues of the matrix A^{nc} have been determined in closed form as

$$\lambda_{1,2}^{nc} = 0, \quad \lambda_3^{nc} = -cM p_E u / |u| \quad (50)$$

which become infinitesimal for vanishing M . The matrix A^{nc} can be termed a “non-linear coupling” matrix, for it completes the non-linear coupling between convection and acoustics within (48) so that the two Euler eigenvalues $\lambda_{2,3}^E$ in (13) do correspond to the sum of convection and acoustic speeds. Since decomposition (48) will be used in the upstream-bias formulation for small Mach numbers only and considering that the eigenvalues in (50) vanish for these Mach numbers, no need exists to involve A^{nc} in the upstream-bias approximation of the flux jacobian (11).

The eigenvalues of A^a are exactly determined in closed form as

$$\lambda_1^a = 0, \quad \lambda_{2,3}^a = \pm c \quad (51)$$

The matrix A^a , therefore, can be termed the “acoustics” matrix, for its eigenvalues, unlike (46)-(47), equal the speed of sound c for any Mach number. Despite its zero eigenvalue, A^a features a complete set of eigenvectors and thus possesses the similarity form

$$A^a \equiv X \Lambda^a X^{-1} = X \Lambda^{a+} X^{-1} + X \Lambda^{a-} X^{-1}, \quad \Lambda^a = \Lambda^{a+} + \Lambda^{a-} \quad (52)$$

where Λ^{a+} and Λ^{a-} respectively contain non-negative and non-positive eigenvalues. The Euler flux divergence decomposition (48) thus becomes

$$\frac{\partial f}{\partial q} = X \Lambda^{a+} X^{-1} + X \Lambda^{a-} X^{-1} + \frac{\partial f^q}{\partial q} + A^{nc} \quad (53)$$

Since the two acoustics matrices at the rhs of this expression respectively possess non-negative and non-positive eigenvalues, a characteristics-bias approximation of these matrices involves an upstream approximation of the first matrix and a downstream approximation of the second matrix. These approximations naturally lead to the following absolute acoustics-matrix upstream expression

$$|A^a| \frac{\partial q}{\partial x} \equiv X (\Lambda^{a+} - \Lambda^{a-}) X^{-1} \frac{\partial q}{\partial x} = \begin{pmatrix} p_\rho/c & 0 & p_E/c \\ 0 & c & 0 \\ (c^2 - p_\rho) p_\rho / (c p_E) & 0 & (c^2 - p_\rho) / c \end{pmatrix} \frac{\partial q}{\partial x} \quad (54)$$

Upon imposing the condition that the continuity and energy components in this matrix product should also satisfy the acoustic-field results (18), leads to the beautifully simple result

$$|A^a| \frac{\partial q}{\partial x} = c I \frac{\partial q}{\partial x} = c I \frac{\partial q}{\partial x}, \quad I \equiv \text{identity matrix} \quad (55)$$

which indicates for this matrix product the equivalence of replacing $|A^a|$ with the matrix cI , of which all eigenvalues approach $+c$. For acoustic flows and related dependent variables E and ρ , (55) is exact. For non-acoustic flows and related arbitrary-Mach-number dependent variables E and ρ (55) is approximate. This computationally advantageous approximation on the acoustics upstream-bias, not on the flux divergence itself, therefore, will be used essentially in the low subsonic-flow Mach number regime.

4.3 Acoustics Convection Characteristics-Flux Divergence

The previous sections have shown that the flux jacobian (11) can be equivalently expressed as

$$\frac{\partial f}{\partial q} = \begin{cases} \left[\frac{\partial f^q}{\partial q} + \beta \frac{\partial f^p}{\partial q} \right] + \left[(1 - \beta) \frac{\partial f^p}{\partial q} \right] \\ X \Lambda^{a+} X^{-1} + X \Lambda^{a-} X^{-1} + \frac{\partial f^q}{\partial q} + A^{nc} \end{cases} \quad (56)$$

where the first expression is convenient for a characteristics-bias approximation for high-subsonic and supersonic Mach numbers and the second expression is convenient for low-subsonic Mach numbers.

A flux jacobian decomposition for all Mach numbers can thus be cast as the linear combination

$$\frac{\partial f}{\partial q} = (1 - \alpha) \left\{ \left[\frac{\partial f^q}{\partial q} + \beta \frac{\partial f^p}{\partial q} \right] + \left[(1 - \beta) \frac{\partial f^p}{\partial q} \right] \right\} + \alpha \left\{ X \Lambda^{a+} X^{-1} + X \Lambda^{a-} X^{-1} + \frac{\partial f^q}{\partial q} + A^{nc} \right\} \quad (57)$$

with $0 \leq \alpha \leq 1$, which leads to the following acoustics-convection decomposition of the flux jacobian

$$\frac{\partial f}{\partial q} = \alpha X \Lambda^{a+} X^{-1} + \alpha X \Lambda^{a-} X^{-1} + \left[\frac{\partial f^q}{\partial q} + (1 - \alpha) \beta \frac{\partial f^p}{\partial q} \right] + (1 - \alpha)(1 - \beta) \frac{\partial f^p}{\partial q} + \alpha A^{nc} \quad (58)$$

As mentioned in Section 4.2, an upstream approximation to the Euler-flux jacobian will be developed by establishing upstream approximations only for the first four terms in (58), where the jacobian matrix $\left[\frac{\partial f^q}{\partial q} + (1 - \alpha) \beta \frac{\partial f^p}{\partial q} \right]$ is counted as one term. The reason for this coupling is that, with reference to (43), the eigenvalues of this jacobian matrix will all keep the same algebraic sign, because $(1 - \alpha)\beta \leq \beta$.

One justification for this selective upstream formulation rests on the physical acoustics and convection significance of these terms. For any magnitude of both pressure and pressure gradient, the convection field uniformly carries information along streamlines; hence, the entire $\frac{\partial f^q}{\partial q}$ can receive an upstream bias along one single direction. The matrices $X \Lambda^{a+} X^{-1}$ and $X \Lambda^{a-} X^{-1}$ account for the bi-modal propagation of acoustic waves; these matrices are thus used for an acoustics upstream approximation, for low Mach numbers. The pressure flux f^p too accounts for the bi-modal propagation of acoustic waves, but in conjunction with $\frac{\partial f^q}{\partial q}$. As the Mach number increases from zero, a larger and larger fraction $(1 - \alpha)\beta \frac{\partial f^p}{\partial q}$ of the pressure flux jacobian can thus be upstreamed in the same direction as and along with $\frac{\partial f^q}{\partial q}$, while $(1 - \alpha)(1 - \beta) \frac{\partial f^p}{\partial q}$ is upstreamed in the opposite direction. As the Mach number increases, therefore, a smaller and smaller fraction $\alpha(X \Lambda^{a+} X^{-1} + X \Lambda^{a-} X^{-1})$ of $(X \Lambda^{a+} X^{-1} + X \Lambda^{a-} X^{-1})$ is upstreamed. The upstream-bias function α will decrease and β will increase as the Mach number increases, so as to ensure physical significance of the overall upstream-bias approximation to the first four terms in (58). The function β , in turn, depends on another function δ that leads to simpler expressions.

Given the algebraic sign of the eigenvalue set of each matrix term in (58), the associated direction cosines a_ℓ for the upstream-bias expression (28) are

$$a_1 = +1, \quad a_2 = -1, \quad a_3 = s = \text{sgn}(u), \quad a_4 = -s = -\text{sgn}(u), \quad a_5 = 0 \quad (59)$$

where $s = \text{sgn}(u)$ denotes the algebraic sign of u . With (58), (59), approximation (55), and $\delta \equiv (1 - \alpha)(2\beta - 1)$, the general expression (28) leads to the acoustics-convection characteristics flux divergence

$$\frac{\partial f^C}{\partial x} = \frac{\partial f}{\partial x} - \frac{\partial}{\partial x} \left[\varepsilon \psi \left(\alpha c I + s \frac{\partial f^q}{\partial q} + s \delta \frac{\partial f^p}{\partial q} \right) \frac{\partial q}{\partial x} \right] = \frac{\partial f}{\partial x} - \frac{\partial}{\partial x} \left[\varepsilon \psi \left(\alpha c \frac{\partial q}{\partial x} + s \frac{\partial f^q}{\partial x} + s \delta \frac{\partial f^p}{\partial x} \right) \right] \quad (60)$$

where I denotes the identity matrix of appropriate size. In particular, the coupling of an upstream approximation for $(1 - \alpha)\beta \frac{\partial f^p}{\partial q}$, via a_3 , with a downstream approximation for $(1 - \alpha)(1 - \beta) \frac{\partial f^p}{\partial q}$, via a_4 results in an overall upstream approximation of the pressure gradient, but with variable weight δ . The operation count for expression (60) is then comparable to that of an FVS formulation. The terms in this expression, furthermore, directly correspond to the physics of acoustics and convection. For low Mach numbers, $\delta = 0$ and (60) reduces to

$$\frac{\partial f^C}{\partial x} = \frac{\partial f}{\partial x} - \frac{\partial}{\partial x} \left[\varepsilon \psi \left(\alpha c \frac{\partial q}{\partial x} + s \frac{\partial f^q}{\partial x} \right) \right] \quad (61)$$

which essentially induces only an acoustics upstream. Heed that the components within f^C remain linearly independent of one another, which avoids the linear-dependence instability in the steady low-Mach-number Euler equations. For supersonic flow, $\alpha = 0$ and $\delta = 1$. Expression (60) in this case becomes

$$\frac{\partial f^C}{\partial x} = \frac{\partial f}{\partial x} - \frac{\partial}{\partial x} \left[\varepsilon \psi \left(s \frac{\partial f}{\partial x} \right) \right] \quad (62)$$

which corresponds to an upstream approximation of the entire Euler flux divergence.

5 Upstream-Bias Eigenvalues and Functions

The acoustics-convection upstream functions α and δ depend on the Mach number. They are determined by enforcing the upstream stability condition on the upstream matrix for (60). The divergence of the characteristics flux f^C in (60) becomes

$$\frac{\partial f^C}{\partial x} = \frac{\partial f}{\partial x} + \frac{\partial}{\partial x} \left[\varepsilon \psi \left(\alpha c I + s \frac{\partial f^q}{\partial q} + s \delta \frac{\partial f^p}{\partial q} \right) \frac{\partial q}{\partial x} \right] \quad (63)$$

The terms between parentheses collectively constitute the upstream-bias dissipation matrix

$$\mathcal{A} \equiv \alpha c I + s \frac{\partial f^q}{\partial q} + s \delta \frac{\partial f^p}{\partial q} \quad (64)$$

Despite the formidable algebraic complexity of \mathcal{A} , all of its eigenvalues have been analytically determined exactly in closed form. Dividing through by the speed of sound c , the non-dimensional form of these eigenvalues is

$$\lambda_1 = \alpha + M, \quad \lambda_{2,3} = \alpha + \left(1 + \frac{1 - \delta}{2} p_E \right) M \pm \left(\left(\frac{1 - \delta}{2} p_E M \right)^2 + \delta \right)^{1/2} \quad (65)$$

In order to ensure physical significance for the characteristics-bias flux within (60), hence for the upstream-bias approximation to decomposition (58), the upstream bias functions α and δ will

therefore be determined by forcing the upstream-bias eigenvalues (65) to remain positive for all Mach numbers. Following the considerations after (55), in particular, all these eigenvalues must converge to 1 for vanishing Mach number. Rather than prescribing some expressions for α and δ and accepting the resulting variations for these eigenvalues, physically reasonable expressions for these eigenvalues are instead prescribed and the corresponding functions for α and δ determined.

5.1 Eigenvalue λ_3

This eigenvalue will correlate with the absolute-value Euler eigenvalue $|M - 1|$. As a consequence, λ_3 will vary between 1 and $1 - M$ for $0 \leq M \leq 1 - \varepsilon_M$ and smoothly shift from $1 - M$ to $M - 1$ within the sonic transition layer $1 - \varepsilon_M \leq M \leq 1 + \varepsilon_M$, where ε_M denotes a transition-layer parameter; in this work $\varepsilon_M = \frac{1}{5}$. One expression for λ_3 that remains smooth and meets these requirements is the composite spline

$$\lambda_3(M) \equiv \begin{cases} 1 - M & , \quad 0 \leq M \leq 1 - \varepsilon_M \\ \frac{(M-1)^2}{2\varepsilon_M} + \frac{\varepsilon_M}{2} & , \quad 1 - \varepsilon_M < M < 1 + \varepsilon_M \\ M - 1 & , \quad 1 + \varepsilon_M \leq M \end{cases} \quad (66)$$

5.2 Eigenvalue λ_1

This eigenvalue correlates with the non-dimensional Euler eigenvalue M , but it too has to equal 1 for $M = 0$; it then must coincide with M for $M > 1$ and also remain greater than λ_3 , as expressed through (66), for consistency with the Euler eigenvalues (13). This condition in particular implies $\lambda_1 \geq \frac{1}{2}$. It thus follows that λ_1 will vary between 1 and M for $0 \leq M \leq \frac{1}{2} + \varepsilon_M$. An expression for $\lambda_1 = \lambda_1(M)$ that remains smooth and meets all of these requirements is the composite spline

$$\lambda_1(M) \equiv \begin{cases} 1 - M & , \quad 0 \leq M \leq \frac{1}{2} - \varepsilon_M \\ \frac{(M - \frac{1}{2})^2}{2\varepsilon_M} + \frac{1 + \varepsilon_M}{2} & , \quad \frac{1}{2} - \varepsilon_M < M < \frac{1}{2} + \varepsilon_M \\ M & , \quad \frac{1}{2} + \varepsilon_M \leq M \end{cases} \quad (67)$$

5.3 Upstream-Bias Functions α and δ and Eigenvalues

From λ_1 and λ_3 in (65), the corresponding expressions for both $\alpha = \alpha(M)$ and $\delta = \delta(M)$ have been exactly determined as

$$\alpha(M) = \lambda_1(M) - M , \quad \delta(M) = \frac{(\lambda_1(M) - \lambda_3(M))(\lambda_1(M) - \lambda_3(M) + p_E M)}{1 + p_E M (\lambda_1(M) - \lambda_3(M))} \quad (68)$$

The variations of the upstream-bias functions $\alpha = \alpha(M)$ and $\delta = \delta(M)$ and the corresponding eigenvalues from (65) are presented in Figures 2, 3, respectively.

Figure 2 indicates that the upstream-bias functions as well as their slopes remain continuous for all Mach numbers, with $0 \leq \alpha \leq 1$, $0 \leq \delta \leq 1$ and $\alpha \equiv 0$ for $M > \frac{1}{2} + \varepsilon_M$, $\delta(M) \equiv 1$, for $M > 1 + \varepsilon_M$. As $\delta = \delta(M)$ rises, the upstream-bias contribution from the acoustics matrix decreases rapidly, reducing to less than 25% of its maximum at $M = 0.39$ with, therefore, concurrent reduction of the

effect of the acoustic-flow formula (55). The variation of $\delta = \delta(M)$ shows that the pressure-gradient contribution to this upstream-bias formulation increases monotonically, while remaining less than 25% of its maximum, for $0 \leq M \leq 0.7$. When $\delta(M) \equiv 1$ for supersonic Mach numbers, the entire pressure-gradient is upstreamed with the same weight as in the convection flux, in complete agreement with the physical mono-axial wave propagation within supersonic flows.

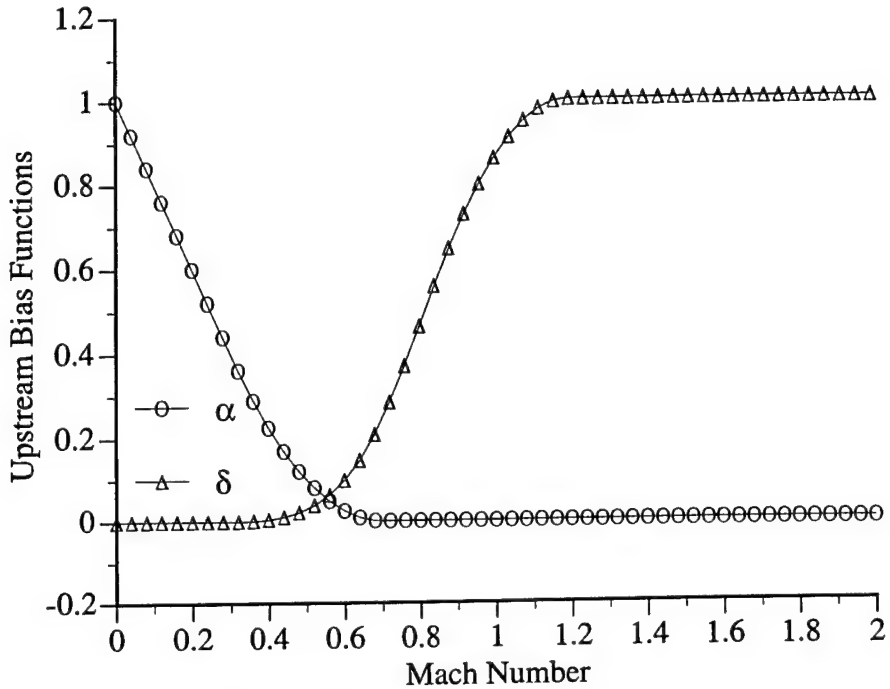


Figure 2: Upstream-Bias Functions

Figure 3 shows that within $0 \leq M \leq 1 + \varepsilon_M$, the eigenvalues $\lambda_1, \lambda_2, \lambda_3$ smoothly approach 1

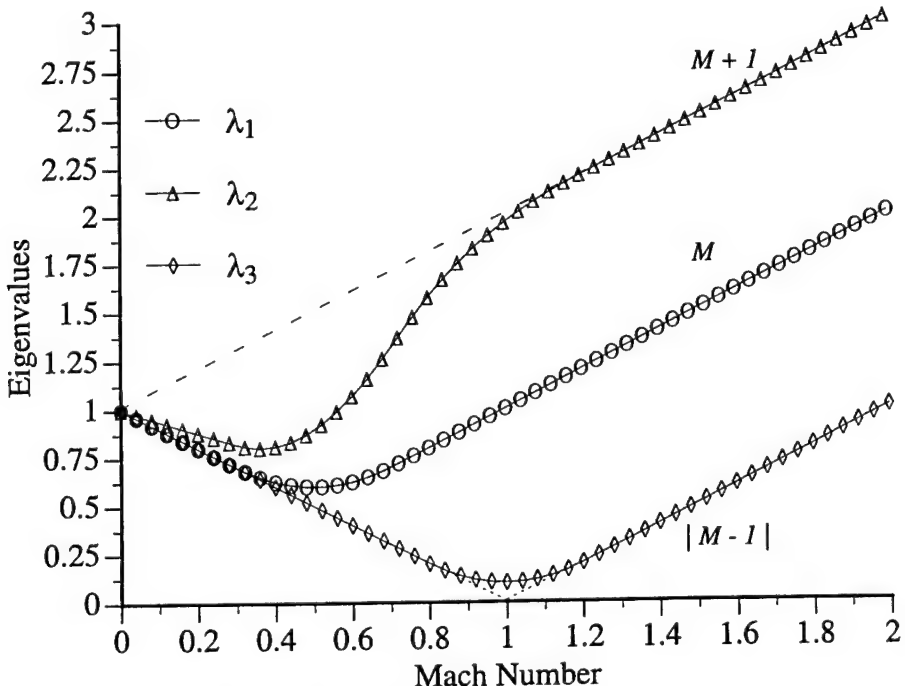


Figure 3: Upstream-Bias Eigenvalues

for vanishing M , indicating a physically consistent upstream-bias approximation of the acoustic equations embedded within the Euler equations. For $M > 1 + \varepsilon_M$, the eigenvalues (65) respectively coincide with the Euler flux jacobian eigenvalues M , $M + 1$, $M - 1$, which corresponds to an upstream-bias approximation of the entire flux vector, for supersonic flows.

6 Finite Element Weak Statement

With reference to (21), the divergence (60) of the characteristics-bias flux f^C leads to the following characteristics-bias integral statement

$$\int_{\Omega} w \left[\frac{\partial q}{\partial t} - \phi + \frac{\partial f}{\partial x} - \frac{\partial}{\partial x} \left(\varepsilon \psi \left(\alpha c \frac{\partial q}{\partial x} + s \frac{\partial f^q}{\partial x} + s \delta \frac{\partial f^p}{\partial x} \right) \right) \right] d\Omega = 0 \quad (69)$$

An integration by parts of the upstream-bias expression then generates the weak statement

$$\int_{\Omega} \left[w \left(\frac{\partial q}{\partial t} - \phi + \frac{\partial f}{\partial x} \right) + \frac{\partial w}{\partial x} \varepsilon \psi \left(\alpha c \frac{\partial q}{\partial x} + s \frac{\partial f^q}{\partial x} + s \delta \frac{\partial f^p}{\partial x} \right) \right] d\Omega = 0 \quad (70)$$

where the surface integral on $\partial\Omega$ corresponding to the upstream-bias expression vanishes because of the boundary condition $\psi(x_{\partial\Omega}) = 0$, imposed to eliminate unnecessary boundary upstream bias. The discrete equations then result from a finite element discretization of this weak statement.

6.1 Galerkin Finite Element Equations

The finite element weak statement^{2,7,9} associated with (70) is

$$\int_{\Omega^h} \left[w^h \left(\frac{\partial q^h}{\partial t} - \phi^h + \frac{\partial f^h}{\partial x} \right) + \frac{\partial w^h}{\partial x} \varepsilon^h \psi^h \left(\alpha^h c^h \frac{\partial q^h}{\partial x} + s^h \frac{\partial f^{q^h}}{\partial x} + s^h \delta^h \frac{\partial f^{p^h}}{\partial x} \right) \right] d\Omega = 0 \quad (71)$$

where superscript “ h ” signifies spatial discrete approximation. The approximation q^h exists on a partition Ω^h , $\Omega^h \subseteq \Omega$, of Ω . This partition Ω^h has its boundary nodes on the boundary $\partial\Omega$ of Ω and results from the union of N_e non-overlapping elements Ω_e , $\Omega^h = \bigcup_{e=1}^{N_e} \Omega_e$. For N mesh nodes within Ω^h , there exist clusters of “master” elements Ω_i^m , each comprising only those adjacent elements that share a mesh node x_i , which implies existence of exactly N master elements. As Figure 4 shows, on each master element Ω_i^m , the discrete test function $w^h \equiv w_i = w_i(x)$, $1 \leq i \leq N$, will coincide with the “pyramid” basis function with compact support on Ω_i^m . Such a function equals one at node x_i , zero at all other mesh nodes, and also identically vanishes both on the boundary segments of Ω_i^m not containing x_i , and elsewhere within the computational domain outside Ω_i^m .

Note that Ω_i^m represents a “finite volume” as used in finite volume schemes, which, however, do not employ pyramid test functions. The following developments are based on a linear pyramid test function w_i , which can be expressed as

$$w_i(x) \equiv \begin{cases} \frac{x - x_{i-1}}{\Delta x_{i-\frac{1}{2}}} & , \quad x_{i-1} \leq x \leq x_i \\ \frac{x_{i+1} - x}{\Delta x_{i+\frac{1}{2}}} & , \quad x_i \leq x \leq x_{i+1} \end{cases} \quad (72)$$

The discrete solution q^h at each time t assumes the form of the following linear combination

$$q^h(x, t) \equiv \sum_{j=1}^N w_j(x) \cdot q^h(x_j, t) \quad (73)$$

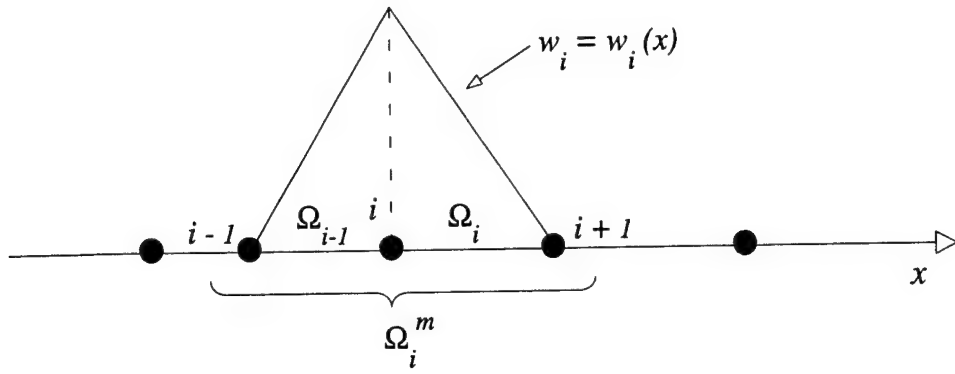


Figure 4: Master Element Ω_i^m and Test Function $w_i = w_i(x)$

of nodal solution values and trial functions, which coincide with the test functions $w_j(x)$ for a Galerkin formulation. Similarly, the source $\phi = \phi(x, q(x, t))$ and fluxes $f = f(q(x, t))$, $f^q = f^q(q(x, t))$ and $f^p = f^p(q(x, t))$ are discretized through the group expressions

$$\begin{aligned} \phi^h(x, t) &\equiv \sum_{j=1}^N w_j(x) \cdot \phi(x_j, q^h(x_j, t)) , \quad f^h(x, t) \equiv \sum_{j=1}^N w_j(x) \cdot f(q^h(x_j, t)) \\ f^{q^h}(x, t) &\equiv \sum_{j=1}^N w_j(x) \cdot f^q(q^h(x_j, t)) , \quad f^{p^h}(x, t) \equiv \sum_{j=1}^N w_j(x) \cdot f^p(q^h(x_j, t)) \end{aligned} \quad (74)$$

The notation for the discrete nodal variable and fluxes is then simplified as $q_j(t) \equiv q^h(x_j, t)$, $\phi_j(t) \equiv \phi^h(x_j, t)$, $f_j \equiv f^h(x_j, t)$, $f_j^q \equiv f^{q^h}(x_j, t)$, $f_j^p \equiv f^{p^h}(x_j, t)$ and expansions (73)-(74) are then inserted into (71), which yields the discrete finite element weak statement

$$\int_{\Omega^h} w_i \left[w_j \left(\frac{dq_j}{dt} - \phi_j \right) + \frac{\partial w_j}{\partial x} f_j \right] d\Omega + \int_{\Omega^h} \frac{\partial w_i}{\partial x} \frac{\partial w_j}{\partial x} \varepsilon^h \psi^h \left[\alpha^h c^h q_j + s^h f_j^q + s^h \delta^h f_j^p \right] d\Omega = 0 \quad (75)$$

for $1 \leq i \leq N$, with ε set equal to a reference length within each element, typically a measure of the element size. While an expression like (73) for ψ^h , α^h , c^h , s^h , and δ^h can be directly accommodated within (75), each of these variables in this study has been set equal to a piece wise constant for computational simplicity, one centroidal constant value per element. Since the test and trial functions w_i are prescribed functions of x , the spatial integrations in (75) are then exactly carried out, which transforms (75) into a system of ordinary differential equations (ODE) in continuum time for determining at each time level t the unknown nodal values $q^h(x_j, t)$.

For a clear comparison between traditional finite difference/volume schemes³ and the acoustics-convection finite element algorithm (75), at any interior node “ i ” of the representative grid in Figure 4, equations (75) with $\varepsilon^h \equiv (\Delta x_{i+\frac{1}{2}})/2$ can be equivalently recast in difference notation as

$$\begin{aligned} \frac{\Delta x_{i-\frac{1}{2}}}{6} \left(\frac{dq_{i-1}}{dt} + 2 \frac{dq_i}{dt} - \phi_{i-1} - 2\phi_i \right) + \frac{\Delta x_{i+\frac{1}{2}}}{6} \left(2 \frac{dq_i}{dt} + \frac{dq_{i+1}}{dt} - 2\phi_i - \phi_{i+1} \right) = \\ = -(\psi \alpha c)_{i-\frac{1}{2}} (q_i - q_{i-1}) + (\psi \alpha c)_{i+\frac{1}{2}} (q_{i+1} - q_i) + \\ -\frac{1}{2} \left((f_i^q - f_{i-1}^q) \cdot (1 + (s\psi)_{i-\frac{1}{2}}) + (f_{i+1}^q - f_i^q) \cdot (1 - (s\psi)_{i+\frac{1}{2}}) \right) + \\ -\frac{1}{2} \left((f_i^p - f_{i-1}^p) \cdot (1 + (s\psi\delta)_{i-\frac{1}{2}}) + (f_{i+1}^p - f_i^p) \cdot (1 - (s\psi\delta)_{i+\frac{1}{2}}) \right) \end{aligned} \quad (76)$$

which uniquely couples several time derivatives at each node “ i ” and features a linear combination of two-point upstream and downstream flux differences. In these finite element equations, the values of the controller ψ^h determines the combination weights of the downstream and upstream expressions, and since ψ^h remains non-negative, these equations induce the appropriate upstream bias, since the upstream weight $1 + \psi_{i-\frac{1}{2}}$ always exceeds the downstream weight $1 - \psi_{i+\frac{1}{2}}$. As a result, the finite element weak statement (75) generates consistent variable-upstream-bias discrete equations that correspond to an upstream-bias discretizations for the original Euler system (1), within a compact block tri-diagonal matrix statement.

For smooth solutions, these equations will still couple upstream and downstream points even for supersonic flows. The potential objection that one such algorithm would violate the physics of mono-directional wave propagation for supersonic flows is easily addressed with Courant's and Hilbert's classical developments¹¹ for non-linear hyperbolic systems. They in fact concluded that while waves propagate along characteristics, smooth solutions can be expanded in Taylor's series within arbitrary regions encircling any given point and along any direction radiating upstream or downstream from the point.

For a closer comparison with upwind finite-volume schemes³, the finite element equations (76) can be rearranged to generate the “numerical flux”

$$F_{i+\frac{1}{2}} \equiv \frac{f_i + f_{i+1}}{2} - \psi_{i+\frac{1}{2}} \left[(\alpha c)_{i+\frac{1}{2}} (q_{i+1} - q_i) + \frac{s_{i+\frac{1}{2}}}{2} (f_{i+1}^q - f_i^q) + \frac{(s\delta)_{i+\frac{1}{2}}}{2} (f_{i+1}^p - f_i^p) \right] \quad (77)$$

which corresponds to the discrete counterpart of the characteristics-bias flux within (60). By virtue of this numerical flux, equations (76) are recast as

$$\begin{aligned} \frac{\Delta x_{i-\frac{1}{2}}}{6} \left(\frac{dq_{i-1}}{dt} + 2 \frac{dq_i}{dt} - \phi_{i-1} - 2\phi_i \right) + \frac{\Delta x_{i+\frac{1}{2}}}{6} \left(2 \frac{dq_i}{dt} + \frac{dq_{i+1}}{dt} - 2\phi_i - \phi_{i+1} \right) = \\ = - \left(F_{i+\frac{1}{2}} - F_{i-\frac{1}{2}} \right) \end{aligned} \quad (78)$$

which shows that the finite element weak statement (75) naturally leads to a discretely conservative algorithm.

6.2 Boundary Equations and Pressure Boundary Condition

The integral statement (70) directly yields a set of consistent boundary differential equations, for both unconstrained boundary variables and for pressure, to enforce a pressure boundary condition at a subsonic outlet. These equations do not require any algebraic extrapolation of variables, but rather couple the time derivatives of boundary- and interior-node variables within the boundary cell.

For the linear elements in this study, let N and $N - 1$ denote the nodes within the outlet boundary element, with N corresponding to the outlet node. For the discrete finite element equation associated with boundary node x_N , the controller ψ and test function w satisfy the conditions $\psi = 0$ and $w(x_{N-1}) = 0$, $w(x_N) = 1$.

The boundary differential equation from (75) corresponding to an outlet node becomes

$$\frac{\Delta x_{N-\frac{1}{2}}}{3} \left(\frac{dq_{N-1}}{dt} + 2 \frac{dq_N}{dt} - \phi_{N-1} - 2\phi_N \right) = - (f_N - f_{N-1}) \quad (79)$$

This equation directly couples the time derivatives of the solution q at the adjacent boundary and interior nodes x_N and x_{N-1} . A similar equation is then obtained at an inlet, mutatis mutandis. Furthermore, no upstream bias is necessary within a boundary equation, hence $\psi = 0$, because as

(79) shows, this finite element boundary equation directly yields an upwind approximation for the divergence of f .

Concerning the pressure outlet boundary condition, this is naturally enforced within the surface integral that emerges in the momentum-equation weak statement. The convection and pressure flux decomposition

$$f(q) = f^q(q) + f^p(q) \quad (80)$$

is first inserted into the non-discrete integral statement (70); subsequent integration by parts of the pressure gradient therein, generates the weak statement

$$\int_{\Omega} w \left(\frac{\partial q}{\partial t} - \phi + \frac{\partial f^q}{\partial x} \right) d\Omega - \int_{\Omega} \frac{\partial w}{\partial x} f^p d\Omega + \left[w(x) f^p \right]_{x=x_{N-1}}^{x=x_N} = 0 \quad (81)$$

A subsequent linear finite element discretization of (81) yields

$$\frac{\Delta x_{N-\frac{1}{2}}}{3} \left(\frac{dq_{N-1}}{dt} + 2 \frac{dq_N}{dt} - \phi_{N-1} - 2\phi_N \right) = - \left(f_N^q - f_{N-1}^q \right) - \left((2f_{\text{out}}^p - f_N^p) - f_{N-1}^p \right) \quad (82)$$

In this equation, f_N^p denotes the outlet-node pressure, as calculated through the equation of state (8), whereas, quite significantly, f_{out}^p can correspond to the specified outlet pressure boundary condition. This strategy for imposing an outlet pressure boundary condition remains intrinsically stable. Suppose, for instance, that some numerical perturbation forces f_N^p to decrease below the imposed f_{out}^p . In this case the outlet boundary equation (82) induces a negative time rate of change for m_N , which leads to a corresponding reduction in m_N . From the equation of state (8), this reduction then leads to an increase in f_N^p , which corresponds to a stable restoration of the imposed pressure condition. A similar conclusion on the stability of (82) is achieved by considering a perturbation increase in f_N^p . The results in Section 8 confirm the accuracy and stability of this pressure boundary condition procedure.

6.3 Discrete Upstream-Bias Controller ψ^h

This section introduces a new upstream-bias controller ψ^h . This controller varies in the range $0 \leq \psi_{\min} \leq \psi^h \leq \psi_{\max} \leq 1$ and controls within (76) the amount of induced upstream-bias, hence artificial diffusion. By design, $\psi^h = 0$ corresponds to a classical centered discretization, hence no induced diffusion; $\psi^h = 1$, instead, corresponds to a fully upwind formulation, hence maximum diffusion.

Denote then with ψ_i the numerical value of the controller at the representative node “ i ”. By analogy with (73), the discrete controller $\psi^h(x, t)$ is cast as the following linear expansion

$$\psi^h(x, t) = \sum_{j=1}^N w_j(x) \psi(x_j, t) = \sum_{j=1}^N w_j(x) \psi_j \quad (83)$$

and the centroidal evaluation of this expression within each element then yields

$$\psi_{i+\frac{1}{2}} = \frac{\psi_i + \psi_{i+1}}{2} \quad (84)$$

In regions of smooth flow ψ^h approaches ψ_{\min} for a local reduction of upstream-bias diffusion; in region of discontinuous solution ψ^h approaches ψ_{\max} , for an essentially non-oscillatory resolution of local discontinuities. The controller will thus correlate with a local measure φ_i of slope discontinuity.

For a smooth variation, ψ_i is expressed as a function of the measure φ_i as the composite spline

$$\psi_i \equiv \begin{cases} \psi_{\min} & , \quad \varphi_i \leq \varphi_c \\ \psi_{\max} + \frac{\psi_{\max} - \psi_{\min}}{(\varphi_d - \varphi_c)^3} & \\ \left[-(\varphi_d - 3\varphi_c)\varphi_d^2 - 6\varphi_c\varphi_d\varphi_i + 3(\varphi_d + \varphi_c)\varphi_i^2 - 2\varphi_i^3 \right] & , \quad \varphi_c < \varphi_i < \varphi_d \\ \psi_{\max} & , \quad \varphi_d \leq \varphi_i \end{cases} \quad (85)$$

where $0 \leq \varphi_i \leq 1$ and the positive φ_c and φ_d respectively denote threshold continuity and discontinuity measures. Figure 5 shows the smooth variation of this type of spline controller.

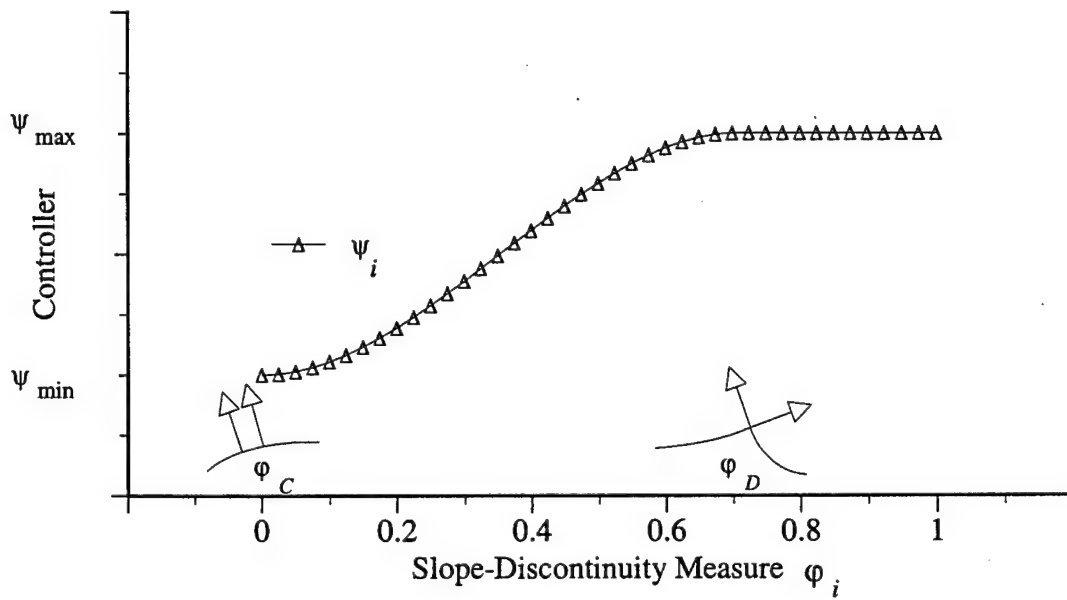


Figure 5: Variation of Controller ψ_i

The implementation of ψ^h thus requires a set of points within Ω^h where the slopes of the approximate solution are generally discontinuous. For the finite element approximation (73), this set of points is the set of finite-element side nodes shared by distinct finite elements in Ω^h , for the continuous expansion (73) changes approximating polynomial from element to element, which implies that solution slopes are generally discontinuous at element side nodes. This type of slope discontinuity is depicted in Figure 6 via the local normal unit vectors \mathbf{n}^L and \mathbf{n}^R respectively to the left and right of the slope-discontinuity point P , where there exist two distinct normal unit vectors, one for each of two elements sharing the node.

With reference to Figure 6, the magnitude $\|\mathbf{n}^R - \mathbf{n}^L\|$ of the vector difference $\mathbf{n}^R - \mathbf{n}^L$ becomes proportional to a bounded measure of local slope discontinuity. If the graph slope is continuous at P , then \mathbf{n}^L coincides with \mathbf{n}^R and $\|\mathbf{n}^R - \mathbf{n}^L\|$ vanishes. On the other hand, when a slope discontinuity exists at P , as shown in the figure, $\|\mathbf{n}^R - \mathbf{n}^L\|$ varies between 0 and 2 depending on the magnitude of the slope jump. A positive measure of slope discontinuity that vanishes for

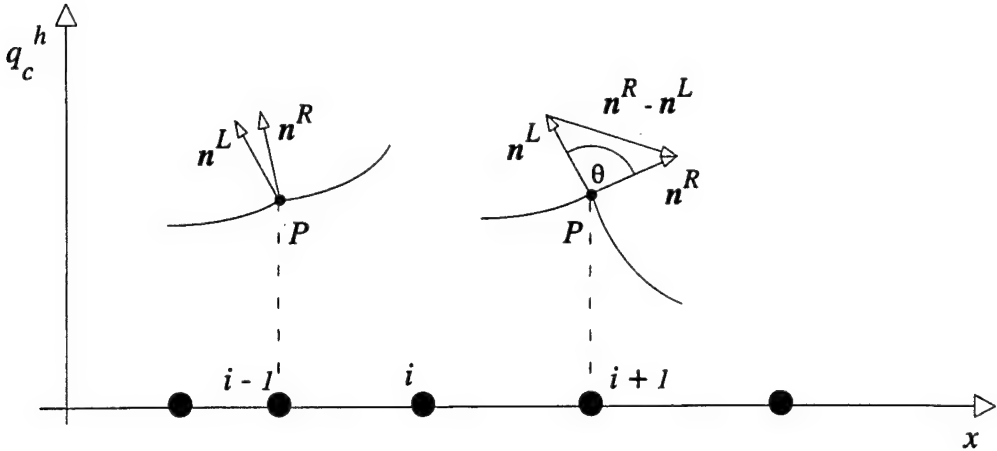


Figure 6: Slope Discontinuities and Local Unit Vectors

continuous slopes, remains bounded and strictly varies between 0 and 1 can thus be defined as

$$\varphi_i \equiv \frac{1}{2} \|\mathbf{n}^R - \mathbf{n}^L\|_{x=x_i} \quad (86)$$

By virtue of the law of cosines, the local measure φ_i also equals

$$\varphi_i = \left(\frac{1 - \cos \theta}{2} \right)_{x=x_i}^{\frac{1}{2}} \quad (87)$$

where θ denotes the angle between the unit vectors in Figure 6.

With reference to Figure 7 and (87), specific numerical values for φ_C , φ_D , ψ_{\min} and ψ_{\max} can be easily established. At a point of solution smoothness, like point $i - 1$ in the figure, \mathbf{n}^L will be parallel to \mathbf{n}^R , hence $\theta = 0^\circ$ which from (87) leads to $\varphi_C = 0$. At a shock, instead, θ can become greater than 90° , as shown in the figure for point i . The threshold $\theta = 90^\circ$ is thus selected for φ_D , which from (87) leads to $\varphi_D = 1/\sqrt{2}$. Numerous numerical experiments with the acoustics-convection algorithm have indicated that a minimal amount of “background” upstream bias is necessary for convergence; this finding is not surprising, since the formulation is essentially centered, hence devoid of any upstream-bias dissipation for $\psi^h = 0$. Hence, $\psi_{\min} > 0$, with typical numerical values in the range $\frac{1}{4} \leq \psi_{\min} \leq \frac{1}{2}$. Concerning ψ_{\max} , a relation with ψ_{\min} readily follows from the requirement that in the neighborhood of a shock the maximum upstream bias can at most correspond to a fully upwind algorithm, for an essentially non-oscillatory capturing of shock waves. Hence, from (84), $\psi_{i+\frac{1}{2}} \leq 1$ with $i + \frac{1}{2}$ denoting the centroid of a finite element (cell) that supports a shock. For a typical case of a shock captured within at least two cells, as shown in Figure 7, (85) leads to $\psi_i = \psi_{\max}$ and $\psi_{i+1} \simeq \psi_{\min}$. From (84), therefore

$$\frac{\psi_{\max} + \psi_{\min}}{2} \leq 1 \Rightarrow \psi_{\max} \leq 2 - \psi_{\min} \quad (88)$$

which linearly decreases as a function of increasing ψ_{\min} . The specific objective of letting ψ^h vary as the solution evolves is to minimize induced upstream-bias dissipation for maximum accuracy within the prescribed computational stencil. As its distinguishing design feature, the acoustics-convection upstream resolution algorithm nevertheless remains an authentic characteristics-bias formulation for any ψ^h with $\psi_{\min} \leq \psi^h \leq \psi_{\max}$.

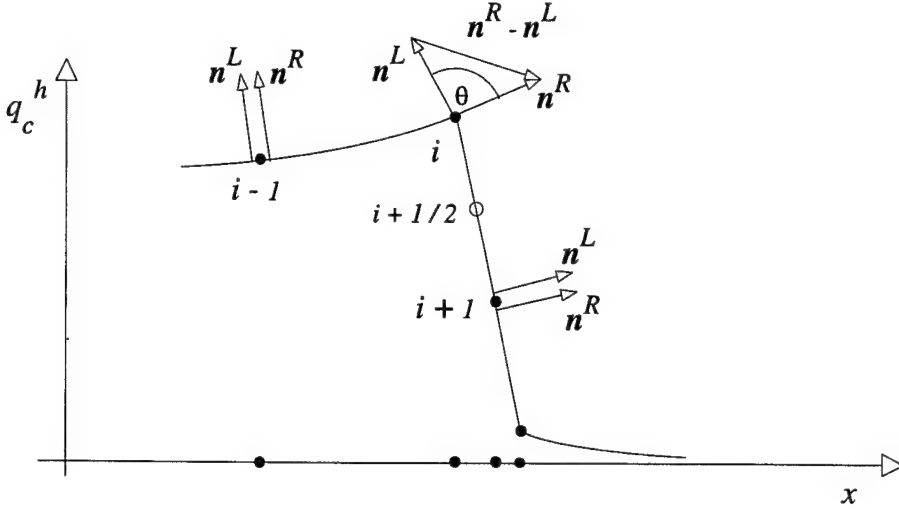


Figure 7: Local Unit Vectors at a Shock

The general expression of φ_i corresponding to a scalar component q_c^h of q^h directly derives from the finite element expansion (73), which can be expressed in synthetic implicit form as $F(q_c^h, x, t) \equiv q_c^h - q_c^h(x, t) = 0$. Hence, a normal unit vector \mathbf{n} can be cast at each time level t as $\mathbf{n} \equiv \text{grad } F(q_c^h, x, t) / \|\text{grad } F\|$, where the vector operator “grad” encompasses the dependent variable q_c^h . The expression for the corresponding φ_i at time level t and point x_i then becomes

$$\varphi_i \equiv \varphi^h(x_i, t) = \frac{1}{2} \left[\left(\frac{1}{\sqrt{1 + \left(\frac{\partial q_c^{hR}}{\partial x} \right)^2}} - \frac{1}{\sqrt{1 + \left(\frac{\partial q_c^{hL}}{\partial x} \right)^2}} \right)^2 + \left(\frac{\frac{\partial q_c^{hR}}{\partial x}}{\sqrt{1 + \left(\frac{\partial q_c^{hR}}{\partial x} \right)^2}} - \frac{\frac{\partial q_c^{hL}}{\partial x}}{\sqrt{1 + \left(\frac{\partial q_c^{hL}}{\partial x} \right)^2}} \right)^2 \right]_{x=x_i}^{\frac{1}{2}} \quad (89)$$

where the partial derivatives are determined through the finite element expansion (73), and where superscripts L and R indicate evaluation within the elements respectively to the left and right of $x = x_i$. The form of (89) at node i of a uniform grid is

$$\varphi_i = \frac{1}{2} \left[\left(\frac{\Delta x}{\sqrt{\Delta x^2 + (q_{c_{i+1}} - q_{c_i})^2}} - \frac{\Delta x}{\sqrt{\Delta x^2 + (q_{c_i} - q_{c_{i-1}})^2}} \right)^2 + \left(\frac{q_{c_{i+1}} - q_{c_i}}{\sqrt{\Delta x^2 + (q_{c_{i+1}} - q_{c_i})^2}} - \frac{q_{c_i} - q_{c_{i-1}}}{\sqrt{\Delta x^2 + (q_{c_i} - q_{c_{i-1}})^2}} \right)^2 \right]^{\frac{1}{2}} \quad (90)$$

where the denominator never vanishes. This expression, furthermore, remains bounded and differentiable for arbitrary nodal values of q_c^h . For the sole purpose of determining the order of this

expression with respect to Δx , for a smooth solution over any two contiguous elements, the discrete solution values q_{c_j} , $i-1 \leq j \leq i+1$, over these elements, can be considered as the nodal values of a single auxiliary continuous functions $q_c(x, t)$: a Lagrangian, trigonometric, or other interpolant of the q_{c_j} 's over both elements. With this consideration, the Taylor's series expansion of (90) yields

$$\varphi_i = \frac{\left|q_c''(x_i, t)\right|}{1 + (q_c'(x_i, t))^2} \frac{\Delta x}{2} + \mathcal{O}(\Delta x^2) = \mathcal{K} \left[1 + (q_c'(x_i, t))^2 \right]^{\frac{1}{2}} \frac{\Delta x}{2} + \mathcal{O}(\Delta x^2) \quad (91)$$

where superscript prime indicates differentiation with respect to x and \mathcal{K} denotes the local curvature. This expansion reveals that φ_i decreases for vanishing Δx . Even for large slopes, furthermore, φ_i remains of order Δx in regions of small curvature. Only when both curvature and slope drastically rise, e.g. at a shock, will φ_i increase, which precisely corresponds to the desired behavior.

7 Implicit Runge Kutta Time Integration

The finite element equations (76) along with appropriate boundary equations and conditions, delineated in Sections 6.2 and 8, can be abridged as the non-linear ODE system

$$\mathcal{M} \frac{dQ(t)}{dt} = F(t, Q(t)) \quad (92)$$

where $\mathcal{M} \frac{dQ(t)}{dt}$ corresponds to the coupling of time derivatives in (76), and $F(t, Q(t))$ represents the remaining terms in (76). The numerical time integration of (92) in this study takes place through a new class of two-stage diagonally implicit Runge-Kutta algorithms⁷ (IRK2) expressed as

$$\begin{aligned} Q_{n+1} - Q_n &= b_1 K_1 + b_2 K_2 \\ MK_1 &= \Delta t \cdot F(t_n + c_1 \Delta t, Q_n + a_{11} K_1) \\ MK_2 &= \Delta t \cdot F(t_n + c_2 \Delta t, Q_n + a_{21} K_1 + a_{22} K_2) \end{aligned} \quad (93)$$

where n now denotes a discrete time station and b_1 , b_2 , c_1 , c_2 , a_{11} , a_{21} , and a_{22} indicate constant Runge-Kutta coefficients, subject to the constraints $c_i = \sum_{j=1}^2 a_{ij}$ and $\sum_{i=1}^2 b_i = 1$. The coefficients for second order accuracy are listed in the Table 1. With these coefficients, in particular, algorithm

Table 1: Runge-Kutta Coefficients

	b_1	b_2	a_{11}	a_{21}	a_{22}
IRK2	$\frac{3 - \sqrt{3}}{4}$	$\frac{1 + \sqrt{3}}{4}$	$\frac{3 - \sqrt{3}}{6}$	$2 - \sqrt{3}$	$\frac{\sqrt{3} - 1}{2}$

(93) becomes absolutely stable for arbitrary stiff non-linear dissipative ODE systems.^{7,12}

This algorithm is implicit because the entries in the arrays K_1 and K_2 remain coupled and are then computed by solving algebraic systems. Diagonally implicit signifies that K_1 is determined independently of K_2 . Thus, given the solution Q_n at time t_n , K_1 is computed first, followed by K_2 . The solution Q_{n+1} is then determined by way of the first expression in (93).

The terminal numerical solution is then determined using Newton's method, which for the implicit fully-coupled computation of the IRK2 arrays K_i , $1 \leq i \leq 2$, is cast as

$$\left[\mathcal{M} - a_{ii} \Delta t \left(\frac{\partial F}{\partial Q} \right)_{Q_i^p}^p \right] (K_i^{p+1} - K_i^p) = \Delta t F(t_n + c_i \Delta t, Q_i^p) - \mathcal{M} K_i^p$$

$$Q_i^p \equiv Q_n + a_{i1}K_1^p + a_{i2}K_2^p \quad (94)$$

where $a_{ij} = 0$ for $j > i$, p is the iteration index, and $K_1^p \equiv K_1$ for $i = 2$; for linear finite elements, the jacobian

$$J_i(Q) \equiv \mathcal{M} - a_{ii}\Delta t \left(\frac{\partial F}{\partial Q} \right)_{Q_i^p}^p \quad (95)$$

then becomes a block tri-diagonal matrix. For all the results documented in the discussion section, the initial estimate K_i^0 is set equal to the zero array, while only one iteration is executed for (94) within each time interval. In this mode, Newton's iteration becomes akin to a classical direct linearized implicit solver.

8 Computational Results

The computational results have validated the accuracy and essential-monotonicity performance of the acoustics-convection upstream resolution algorithm for transient and steady smooth and shocked mixed subsonic / supersonic flows. The algorithm has generated essentially non-oscillatory results that automatically preserve a constant total enthalpy as well as smoothness of both enthalpy and linear momentum across steady normal shocks. These results reflect available exact solutions and numerical results independently generated¹³ using van Leer's and Roe's schemes. The benchmarks in this section cover a total of 5 different perfect-gas flows encompassing flows within: a shock tube, a convergent-divergent (DeLaval) nozzle and a steeply diverging nozzle. The corresponding spatial computational domain Ω for all the results presented is defined as: $\Omega \equiv [a, b] = [0, 1]$, uniformly discretized into 100 linear finite elements, hence $\Delta x = 0.01$. For each benchmark, the calculations proceeded with a prescribed constant maximum Courant number C_{\max} defined as

$$C_{\max} \equiv \max\{|u + c|, |u - c|, c\} \frac{\Delta t}{\Delta x} \quad (96)$$

Given Δx and C_{\max} for each benchmark, the corresponding Δt was thus determined as

$$\Delta t = \frac{C_{\max}\Delta x}{\max\{|u + c|, |u - c|, c\}} \quad (97)$$

As detailed in Section 6.3, the upstream-bias controller uses one scalar component of the dependent variable q . In this study, the algorithm has employed total energy E to calculate ψ .

All the solutions in these validations are presented in non dimensional form, with density ρ , pressure p , energy E and enthalpy H made dimensionless through their respective inlet stagnation (total) values. The non-dimensional speed is obtained by way of the stagnation speed of sound divided by $\sqrt{\gamma}$. The reference speed u_r thus becomes $u_r = \sqrt{\gamma p_{\text{tot,in}}/\rho_{\text{tot,in}}}/\sqrt{\gamma} = \sqrt{p_{\text{tot,in}}/\rho_{\text{tot,in}}}$. Linear momentum is then made dimensionless through total inlet density and reference speed.

8.1 Shock-Tube Flow

This benchmark consists in determining the gas flow that evolves from a rest state within a straight tube. The tube is initially divided into two chambers separated by an impermeable diaphragm placed at the midpoint on the tube axis. The non-dimensional initial conditions for the gas in each of the two chambers are

$$\begin{aligned} \rho &= 1.00 & m &= 0.00 & E &= 2.50 & 0.0 \leq x \leq 0.5 \\ \rho &= 0.125 & m &= 0.00 & E &= 0.25 & 0.5 < x \leq 1.0 \end{aligned} \quad (98)$$

The diaphragm ruptures at $t = 0$ and the solution corresponding to $t = 0.14152$ is sought. At this time station, the exact solution features a normal shock centered at $x = 0.75$, for each of the components of the dependent variables in q ; the distribution of density ρ also develops a contact discontinuity centered at $x = 0.62$. Figures 8 a)-c) present three density distributions as obtained with the acoustics-convection upstream resolution algorithm for $C_{\max} = 1.0$, but with a constant upstream-bias controller ψ .

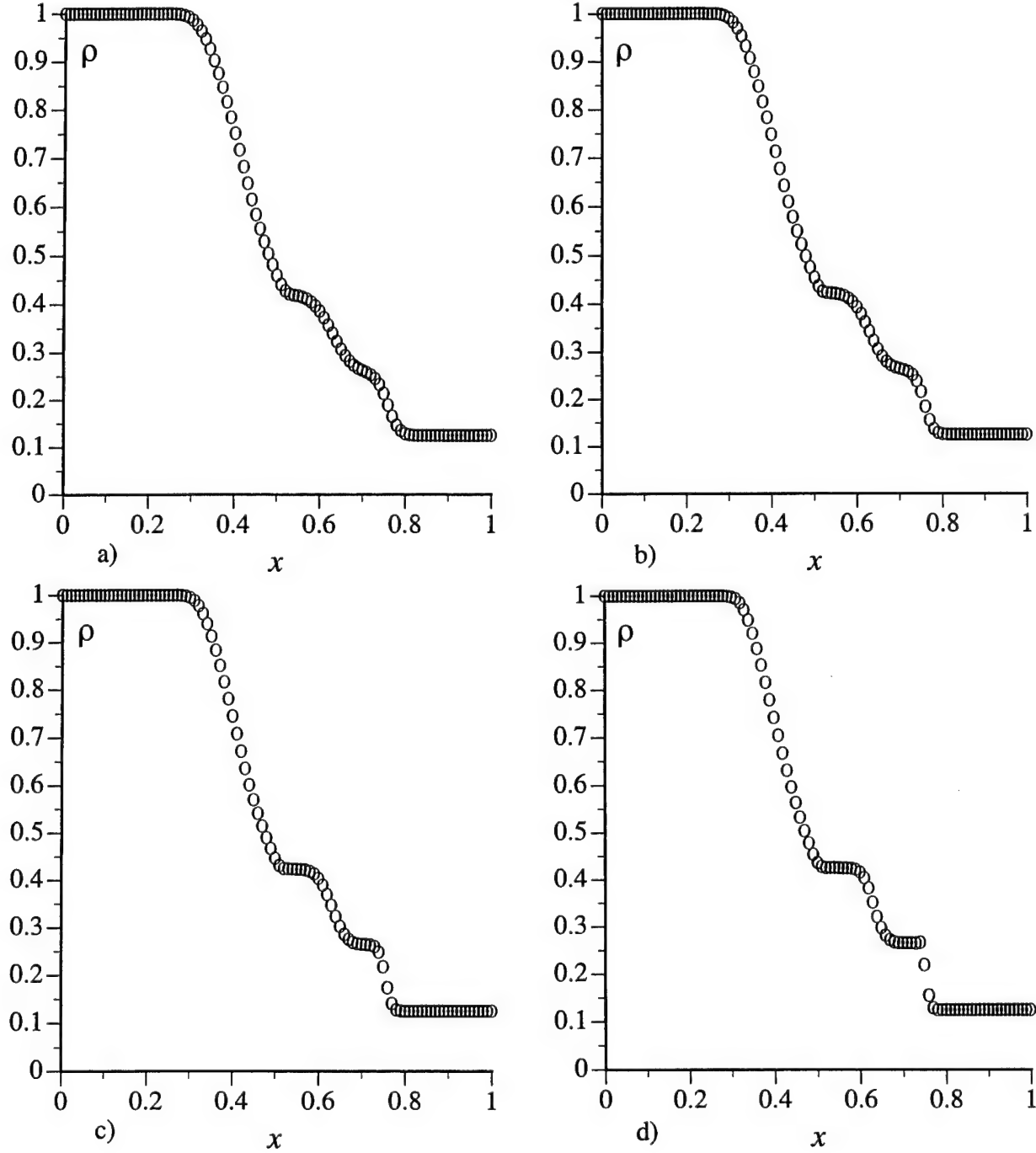


Figure 8: Density Upstream Bias: a) 100%, b) 75%, c) 50%, d) 25%-50% Controlled

The numerical values for ψ for these three solutions are $\psi = 1.0$, $\psi = 0.75$, $\psi = 0.5$, respectively corresponding to 100%, 75% and 50% upstream bias. The figures show that a decrease in upstream-

bias, hence associated artificial diffusion, corresponds to an expected increase in solution resolution. The solution in Figure 1 c), for $\psi = 0.5$, already displays correct solution features with contact discontinuity and normal shock centered at the exact locations, even though the sharp decrease in density modeling the contact discontinuity appears somewhat diffused. Note, however, that this solution remains essentially non-oscillatory without employing a fully-upwind discretization with MUSCL-type extrapolation of variables.

Figures 8 d)-9 b) present the solution generated with a variable controller ψ , with $0.25 \leq \psi < 0.62$ and $C_{\max} = 1.0$. This solution remains essentially non-oscillatory throughout the computational domain. The contact discontinuity in Figure 8 d) is now resolved over about five nodes, with increased overall solution sharpness. The normal shock is captured over two nodes and the two plateaus juxtaposed the contact discontinuity remain essentially flat. Figure 9 a) presents the corresponding distribution of total energy E , which reflects the features in the density solution.

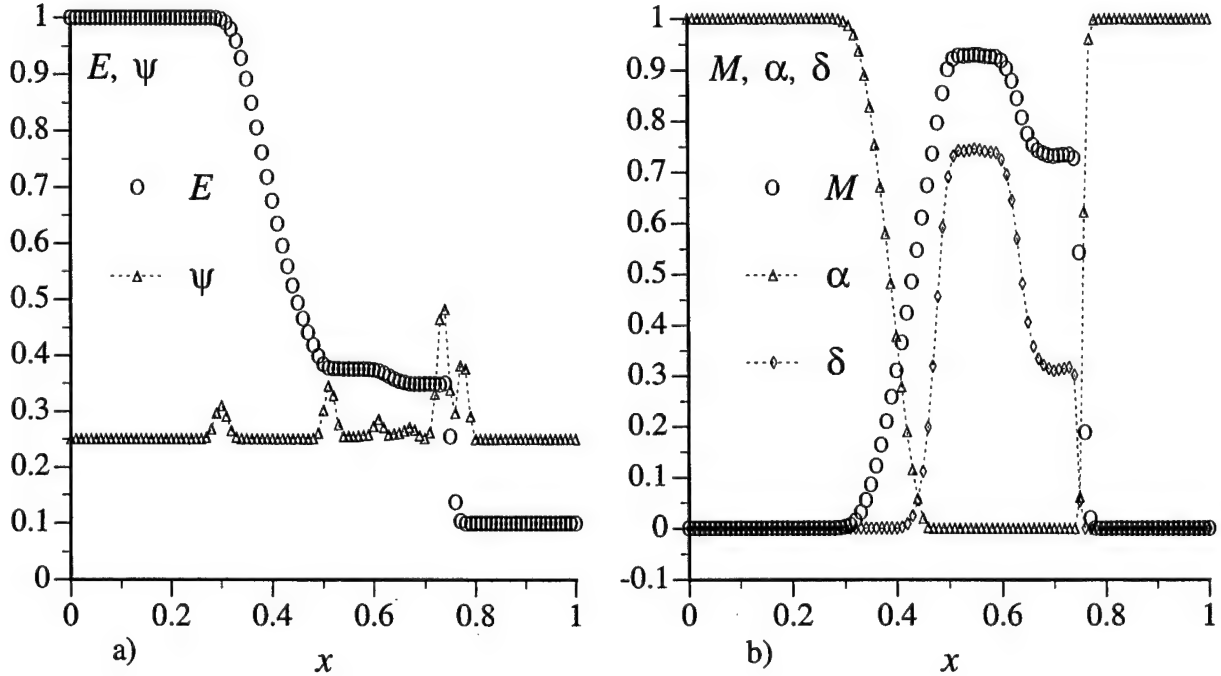


Figure 9: Controlled Upstream: a) Energy and Controller, b) Mach Number, α and δ

This figure also shows the associated variation of ψ , indicating that ψ remains close to its minimum over the smooth parts of the solution. Only at slope discontinuities does ψ increase, following its design features documented in Section 6.3. Therefore, ψ increases marginally, at the expansion extremities and contact discontinuity, and more markedly at the normal shock. At these locations the energy slopes abruptly change. In particular, the larger increases of ψ remain localized at the shock region, where it is precisely needed for an essentially non-oscillatory capturing of the shock. This shock is captured with ψ reaching 0.5, which corresponds to just 50% upstream bias. Away from the shock and other slope discontinuities, $\psi = 0.25$ which corresponds to a mere 25% upstream bias. This solution is therefore achieved with an essentially centered discretization, which leads to the conclusion that a uniformly fully upwind formulation is not strictly necessary within a characteristics-bias algorithm to generate an essentially sharp and non-oscillatory solution.

Figure 9 b) presents the distributions of Mach Number M and associated acoustics and convection upstream-bias functions α and δ . The solution for M correlates with that for ρ and E with essentially flat plateaus and sharp normal shock. The distribution of α indicates that the acoustics upstream-bias induced via the absolute acoustics matrix (55) remains significant, at a level greater than 30%, only for $M \leq 0.3$. Without this acoustics upstream bias, essential monotonicity is lost. For these Mach numbers, $\delta = 0$, which corresponds to a centered approximation of the pressure gradient, for any ψ . For $M > 0.3$, α decreases sharply, accompanied by a corresponding rise in δ . In particular, $\alpha = 0$ for the Mach numbers corresponding to the contact discontinuity, which indicates that the absolute acoustics-matrix upstream-bias term $\alpha c \partial q / \partial x$ plays no local role in the calculation of this discontinuity. With the calculated values of ψ , the characteristics-bias formulation for these Mach numbers is realized only through the convection and pressure gradient components intrinsic to the Euler flux divergence. The aesthetic appearance of the calculated contact discontinuity, therefore, is essentially due to the linear flux approximation employed, which only uses two nodes per cell without extrapolation of variables. As M increases towards its higher plateau, δ reaches its peak numerical value of about 0.75, which, with $\psi = 0.35$, corresponds to a mere 26.3% upstream-bias in the approximation of the pressure gradient. This level of upstream bias further decreases toward the shock, settling to a level of 15% with $\delta \simeq 0.3$ and $\psi \simeq 0.5$ at the shock.

Figures 10 a)-b) display the associated distributions for speed and static pressure. The plateaus in these distributions remain flat and unperturbed by the density contact discontinuity, with sharp shocks captured over about two nodes.

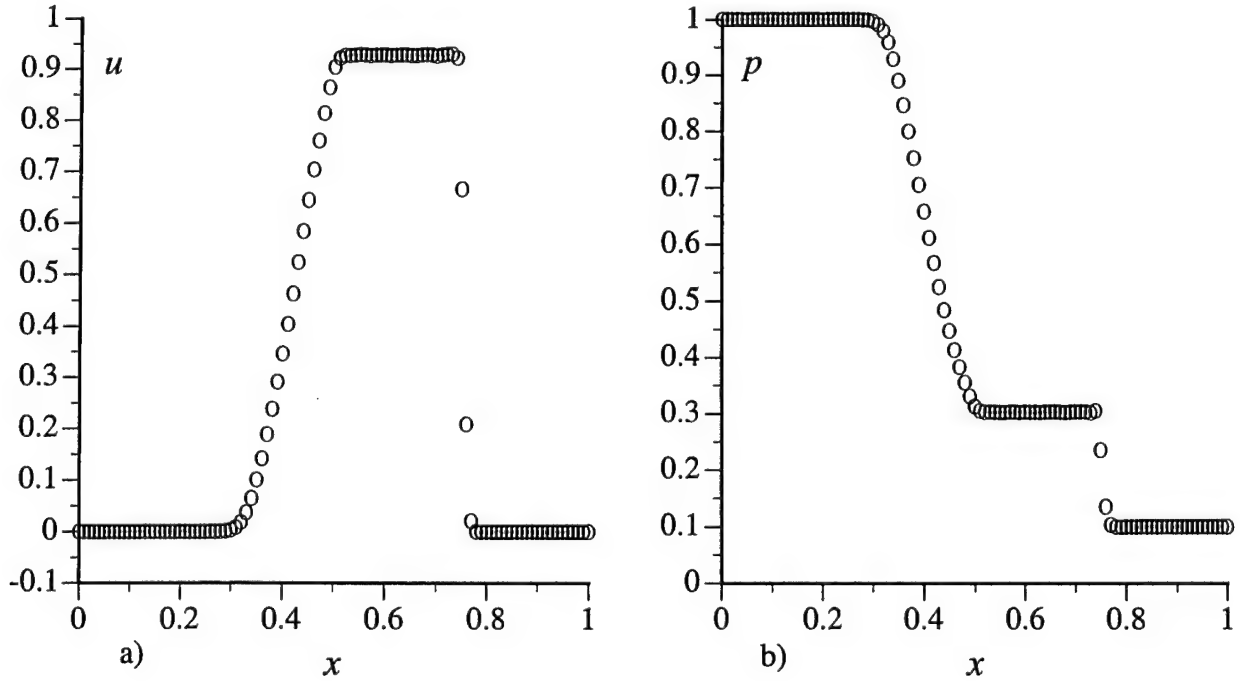


Figure 10: Controlled Upstream: a) Speed, b) Pressure

8.2 Flows in a Converging-Diverging Nozzle

These benchmarks test the capability of the algorithm to calculate steady isentropic and shocked flows than contain a low-Mach number subsonic region. The nozzle cross-section area distribution

remains continuous with continuous slopes, but contains a discontinuous throat curvature¹³, as shown in Figure 11. This feature will induce a nozzle-throat discontinuous curvature in the flow variables even for an isentropic flow, which makes this benchmark particularly useful to assess algorithm resolution.

The nozzle area ratio distribution for these benchmarks is

$$\frac{A(x)}{A_{*in}} = \begin{cases} 1.75 - 0.75 \cos(\pi(2x - 1)) , & 0 \leq x \leq \frac{1}{2} \\ 1.25 - 0.25 \cos(\pi(2x - 1)) , & \frac{1}{2} \leq x \leq 1 \end{cases} \quad (99)$$

with

$$\frac{A(0)}{A_{*in}} = 2.5 , \quad \frac{A(1)}{A_{*in}} = 1.5 \quad (100)$$

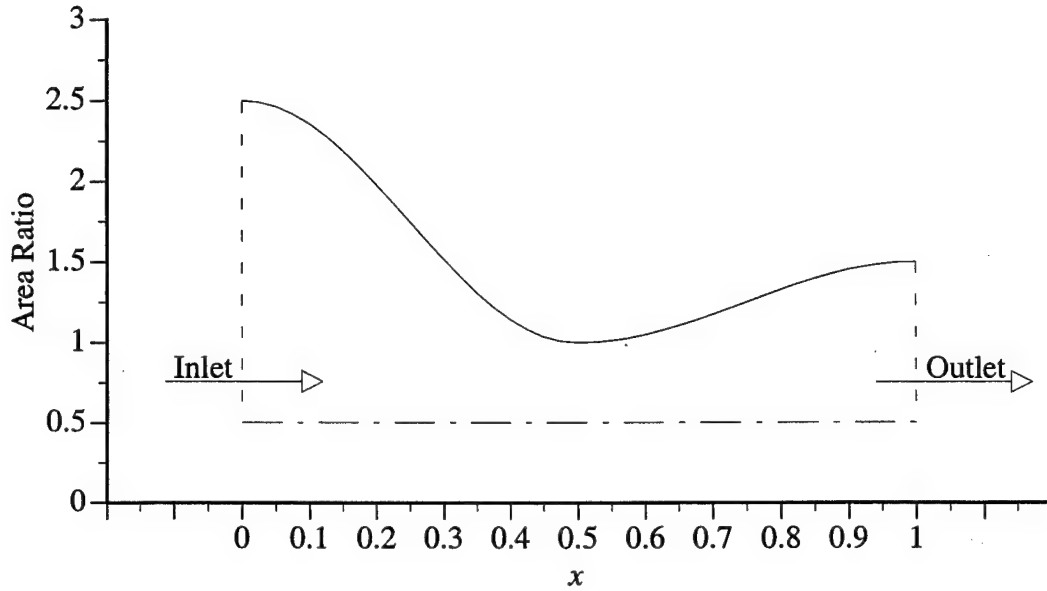


Figure 11: Variation of Area Ratio $A(x)/A_*$

The initial conditions for the gas correspond to an $M = 0.23954$ uniform state, leading to the following initial numerical values for ρ , m , and E throughout the nozzle

$$\rho = 0.97188 , \quad m = 0.27389 , \quad E = 2.44072 \quad (101)$$

The inlet remains subsonic and the physically admissible boundary conditions specified at the inlet are constant Dirichlet conditions on density ρ and total energy E , equal to the initial conditions. An outlet boundary condition is also imposed at a subsonic outlet, as discussed in Section 6.2.

8.2.1 Isentropic Supersonic Flow

For the given initial conditions, the outlet is temporarily subsonic and a pressure boundary condition is imposed. This corresponds to the jump decrease in static pressure: $p/p_{tot,in} = 0.16017$, pertinent to the terminal steady-state outlet supersonic Mach number $M = 1.85413$. The algorithm monitors the outlet Mach number during the calculations and when it exceeds one, the outlet

pressure boundary condition is released, allowing the calculations to proceed toward a steady state without any further outlet boundary condition.

Figures 12 a)-b) present the convergence rate and steady-state speed and Figures 13 a)-b) show the distributions of density, linear momentum, pressure and enthalpy.

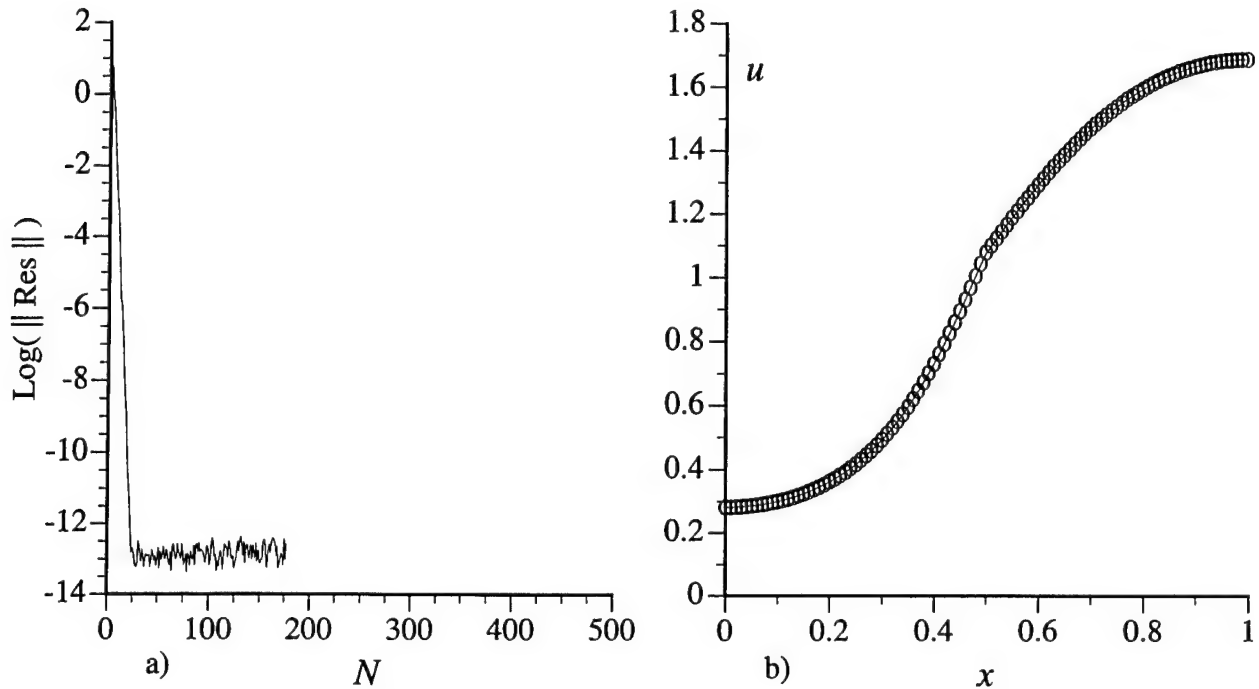


Figure 12: Isentropic Flow: a) Convergence Rate, b) Speed

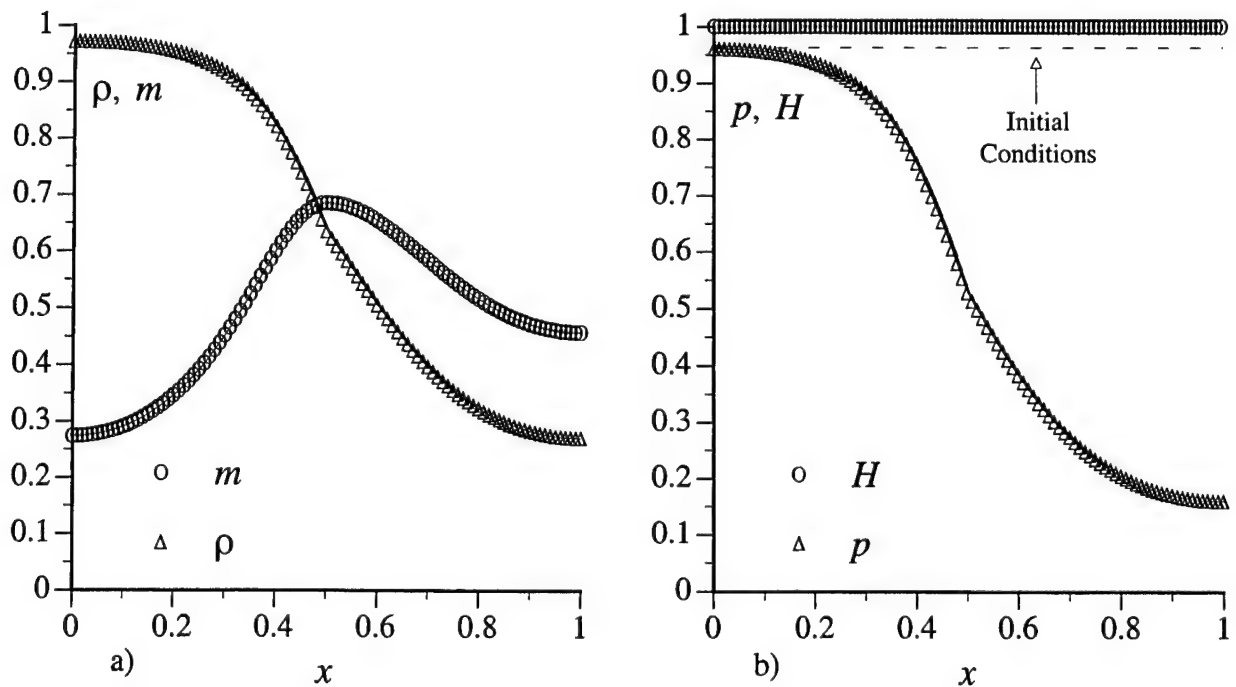


Figure 13: Isentropic Flow: a) Density and Momentum, b) Pressure and Enthalpy

The acoustics-convection upstream resolution algorithm generated a steady state with a reduction of the maximum residual by 13 orders of magnitude, down to machine zero in about 25 time steps with $C_{\max} = 400$. The calculated speed reflects the exact solution, indicated with a solid line. This distribution clearly shows the sonic-point curvature discontinuity, which remains devoid of any unphysical expansion shock and follows the exact solution.

The distributions of density, linear momentum, pressure and enthalpy in Figures 13 a)-b) also reflect the corresponding exact solutions with the curvature discontinuity clearly resolved. The algorithm has also correctly held constant the computed enthalpy, which satisfies the steady-adiabatic-flow constant-enthalpy condition. Figure 14 a) presents the distributions of total energy E , which visually coincides with the exact solution, and upstream bias controller ψ , with $0.25 \leq \psi < 1.0$. Since the solution does not contain any shock, ψ varies modestly, with $\psi \simeq 0.25$ for this steady state, which corresponds to a 25% upstream bias. The obvious location where ψ increases mildly, to $\psi = 0.275$, is at the curvature discontinuity, which correlates with the theoretical finding (91).

Figure 14 b) presents the distribution of Mach number M , which also reflects the exact solution, and the corresponding distributions of the acoustics and pressure-gradient upstream-bias functions α and δ . According to these distributions, the acoustics upstream-bias vanishes for $M \geq 0.7$ and is present with decreasing weight only in the subsonic region of the flow, for $M < 0.7$. For these Mach numbers, $\delta \simeq 0$, which corresponds to a centered approximation of the pressure gradient for any ψ . For increasing M beyond $M = 0.7$, δ briskly rises, which corresponds to a rapid upstream-bias growth in the approximation of the pressure gradient. For $M > 1$, $\delta = 1$, which makes the pressure-gradient upstream bias weight equal to that on the convection divergence.

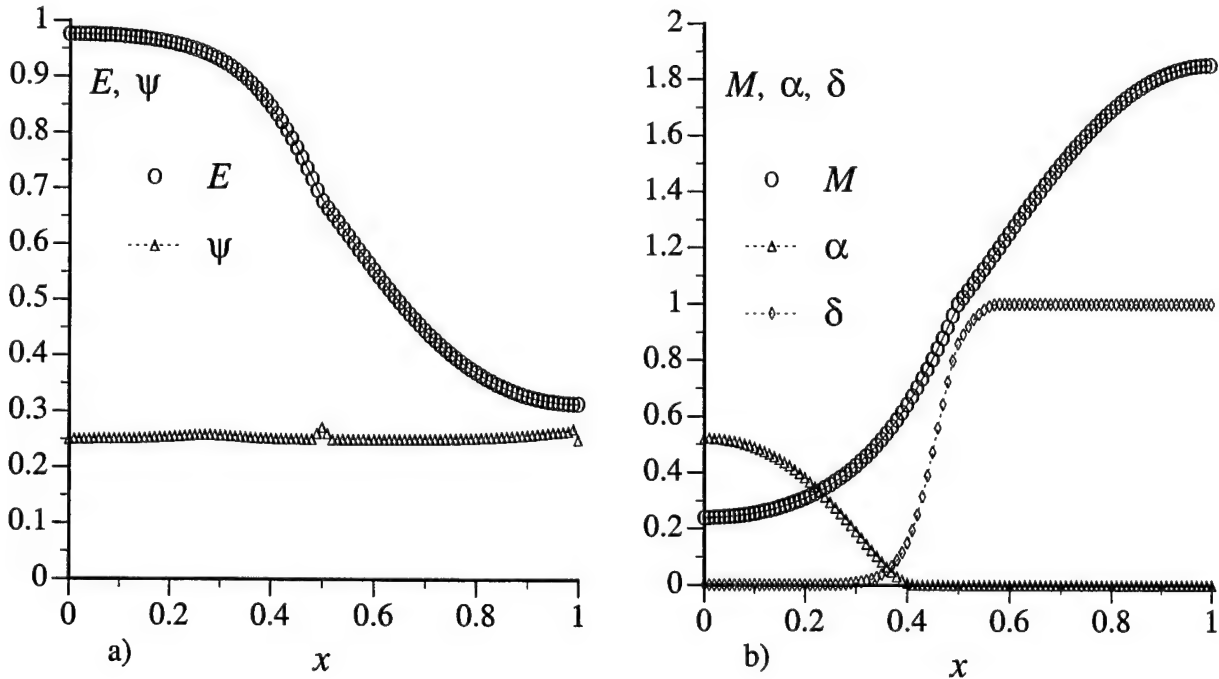


Figure 14: Isentropic Flow: a) Energy and Controller, b) Mach Number, α and δ

8.2.2 Flow with Embedded Normal Shock

A normal shock wave features in this steady flow as a result of the subsonic-outlet pressure boundary condition $p/p_{\text{tot,in}} = 0.84$, imposed as an impulsive step decrease from the initial conditions and for the entire flow evolution toward steady state. The theoretical solution places the normal shock

at the area ratio $A_s/A_{*in} = 1.09896$, which corresponds to the interior of the finite element with node coordinates $x = 0.64$ and $x = 0.65$, within the computational domain. The exact shock Mach numbers are $M_{sup} = 1.36989$ and $M_{sub} = 0.75274$, which lead to the stagnation pressure and critical-area ratios $p_{tot,out}/p_{tot,in} = A_{*in}/A_{*out} = 0.96537$. The associated outlet area ratio and Mach number are $A_{out}/A_{*in} = 1.5$, $M_{out} = 0.45025$.

Figures 15 a)-b) present the convergence rate and steady-state speed. The steady state was achieved in about 25 time steps, for a total of about 50 IRK cycles, with $C_{max} = 400$ and a reduction of the maximum residual by 13 orders of magnitude, down to machine zero. In comparison, Reference 13 reports that a steady state for the same problem was achieved with a minimum of 175 cycles. The calculated speed reflects the exact solution, indicated with a solid line. This distribution clearly shows the sonic-point curvature discontinuity, as well as the normal shock which is captured at the correct location, within about two elements with a mild shock-foot undershoot, similar to that in Reference 13.

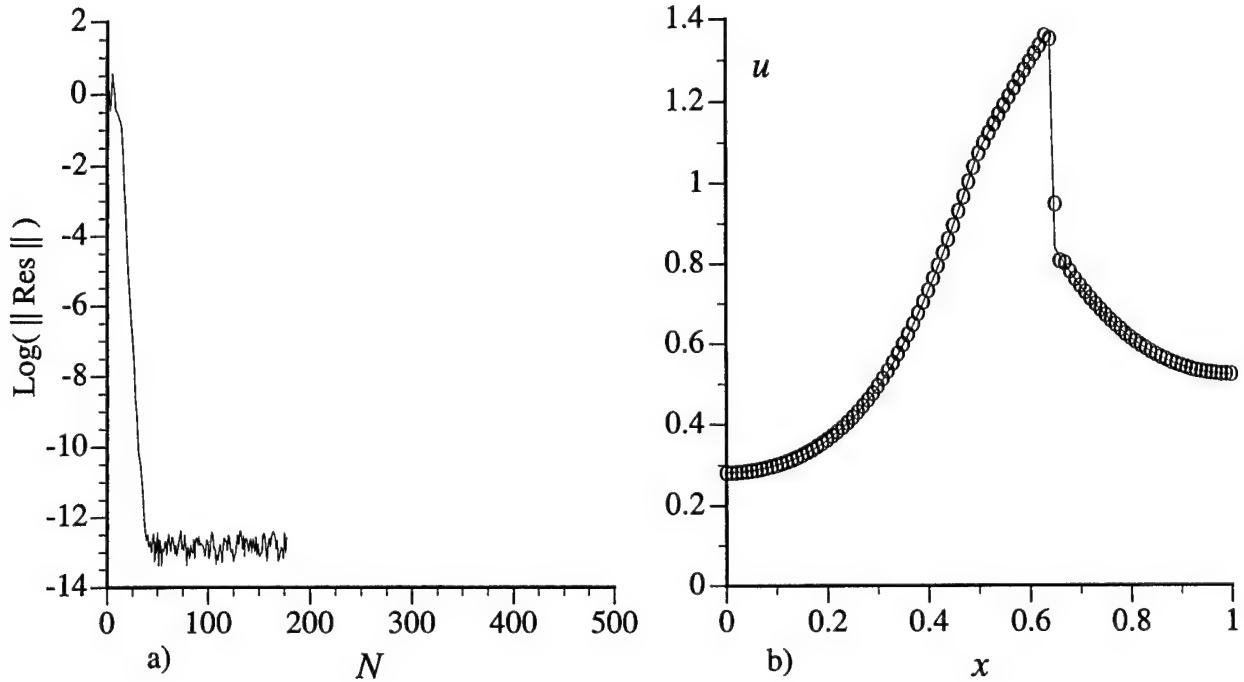


Figure 15: Shocked Flow: a) Convergence Rate, b) Speed

The distributions of static density and pressure in Figures 16 a)-b) also reflect the corresponding exact solutions with the curvature discontinuity clearly resolved and normal shock sharply captured over only one internal node with slight shock-foot overshoots. Significantly, the algorithm has correctly generated continuous distributions for both linear momentum m and enthalpy H across the normal shock, without any shock bump. Furthermore, the computed H remains accurately constant, as has to be the case for a steady adiabatic flow.

Figure 17 a) presents the distributions of total energy E , which visually coincides with the exact solution in solid line, and upstream bias controller ψ , with $0.5 \leq \psi < 1.0$. The controller remains essentially constant over smooth solution regions, with $\psi = 0.5$, which corresponds to a 50% upstream bias. At the shock, ψ rapidly rises, reaching a $\psi \simeq 0.9$ extremum, which induces a 90% upstream-bias. This increase in ψ appears sudden; presumably a slightly milder variation of ψ at the shock could obviate the modest overshoots in ρ , p and E . On the other hand, the algorithm succeeds in focusing an increased level of upstream-bias, hence artificial dissipation at the shock

region only, precisely where required for an essentially sharp and non-oscillatory solution.

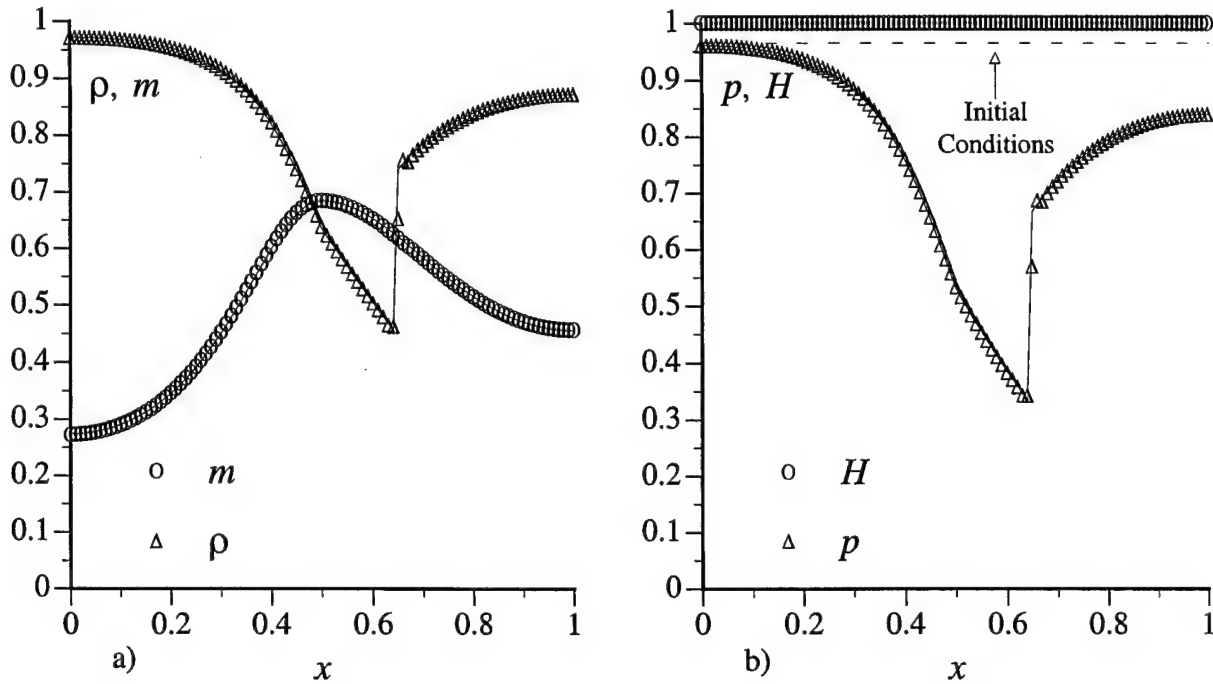


Figure 16: Shocked Flow: a) Density and Momentum, b) Pressure and Enthalpy

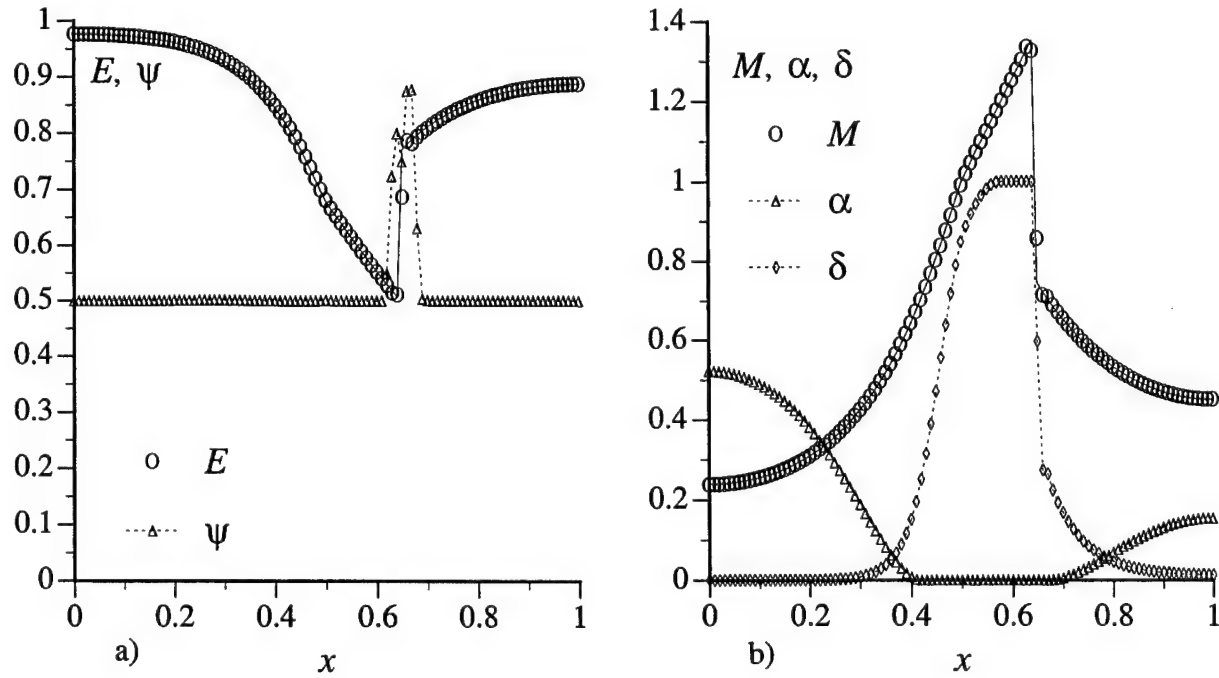


Figure 17: Shocked Flow: a) Energy and Controller, b) Mach Number, α and δ

Figure 17b) presents the distribution of Mach number M , which also reflects the exact solution, and the corresponding distributions of the acoustics and pressure-gradient upstream-bias functions

α and δ . According to these distributions, the acoustics upstream-bias is present, with decreasing weight, only within the inlet and outlet subsonic regions of the flow. This type of upstream-bias vanishes in the supersonic region, including the normal shock, hence it plays no local role in the computation of the shock. Shock resolution, therefore, is entirely due to the convection and pressure-gradient upstream biases, which occur with the same weight at the supersonic side of the shock, where $\delta = 1$. As M falls across the shock, so does δ , which indicates that the upstream bias in the approximation of the pressure gradient quickly decreases, leading to an essentially centered approximation of this gradient towards the outlet. For all the distributions computed for this benchmark, the outlet variations remain smooth and undistorted; in particular the calculated outlet pressure coincides with the imposed pressure boundary conditions, which reflects favorably on the surface-integral pressure enforcement strategy delineated in Section 6.2.

8.3 Flows in a Diverging Nozzle

These benchmarks examine the capability of the algorithm to calculate steady isentropic and shocked flows that involve a high-Mach number supersonic region. The nozzle cross-section area distribution features a steep increase in the diverging region¹³, as shown in Figure 18, which makes it challenging numerically to compute a non-oscillatory shock located in such a region.

The nozzle area ratio distribution for these benchmarks is

$$\frac{A(x)}{A_{\text{in}}} = a + b \tanh(8x - 4) \quad (102)$$

with

$$a = 1.39777, \quad b = 0.34760 \quad (103)$$

and

$$\frac{A(0)}{A_{\text{in}}} = 1.05041, \quad \frac{A(1)}{A_{\text{in}}} = 1.74514 \quad (104)$$

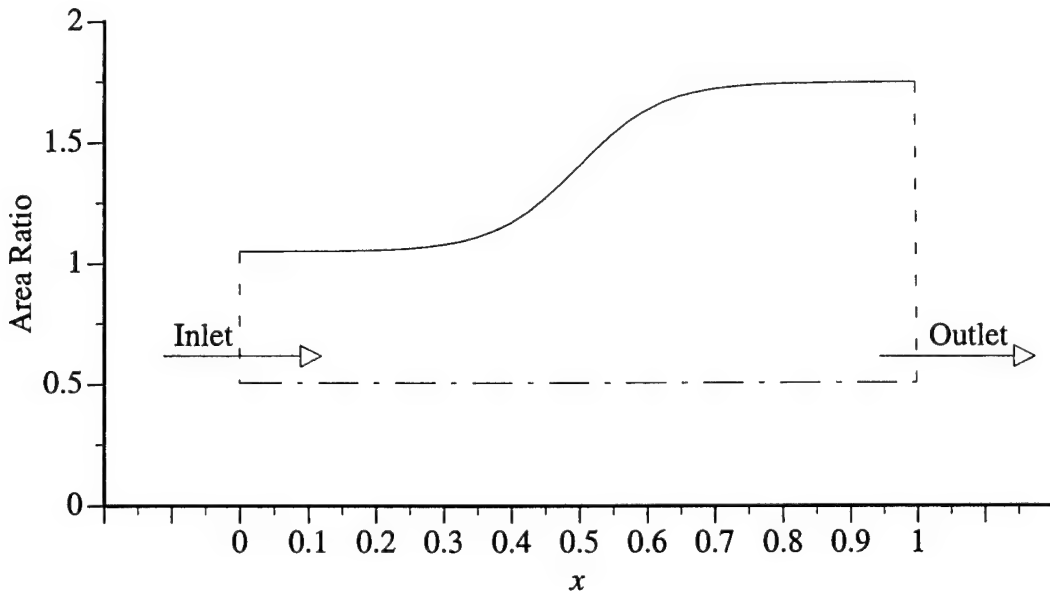


Figure 18: Variation of Area Ratio $A(x)/A_{\text{in}}$

The initial conditions for the gas correspond to an $M = 1.26$ uniform supersonic state, which leads to the following initial state throughout the nozzle

$$\rho = 0.50189, \quad m = 0.65187, \quad E = 1.37567 \quad (105)$$

The inlet flow is constrained supersonic at $M = 1.26$; Dirichlet boundary conditions are thus enforced on density ρ , linear momentum m and total energy E . An outlet pressure boundary condition is also imposed for the simulation of a shocked flow.

8.3.1 Isentropic Supersonic Flow

For the given initial conditions, the outlet is already supersonic, hence no boundary conditions are enforced at the outlet. The evolution of the flow from the initial conditions is thus entirely driven by the area source term in the governing Euler equations (1)-(2).

Figures 19 a)-b) present the convergence rate and steady-state speed. The acoustics-convection upstream resolution algorithm generated a steady-state with a reduction of the maximum residual by 14 orders of magnitude, down to machine zero in about 60 time steps with $C_{\max} = 800$. The calculated speed reflects the exact solution, indicated with a solid line. This distribution clearly shows the rapid increase that is triggered by the drastic nozzle enlargement.

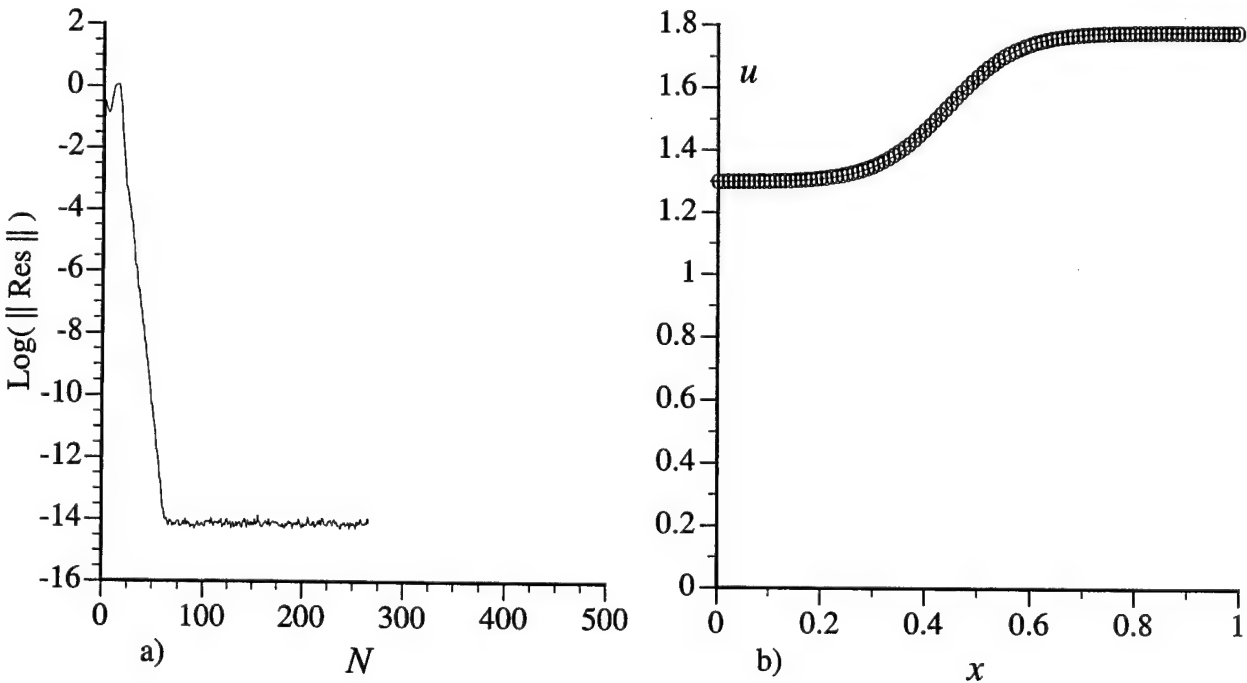


Figure 19: Isentropic Flow: a) Convergence Rate, b) Speed

The distributions of density, linear momentum, pressure and enthalpy in Figures 20 a)-b) also mirror the corresponding exact solutions, with swift expansions clearly resolved. The algorithm has also correctly held constant the computed enthalpy, which satisfies the steady-adiabatic-flow constant-enthalpy condition. Figure 21 a) presents the distributions of total energy E , which remains indistinguishable from the exact solution, and upstream bias controller ψ , with $0.25 \leq \psi < 1.0$. Since the solution is smooth, ψ stays virtually constant with $\psi \simeq 0.25$ for this steady state, which corresponds to a 25% upstream bias.

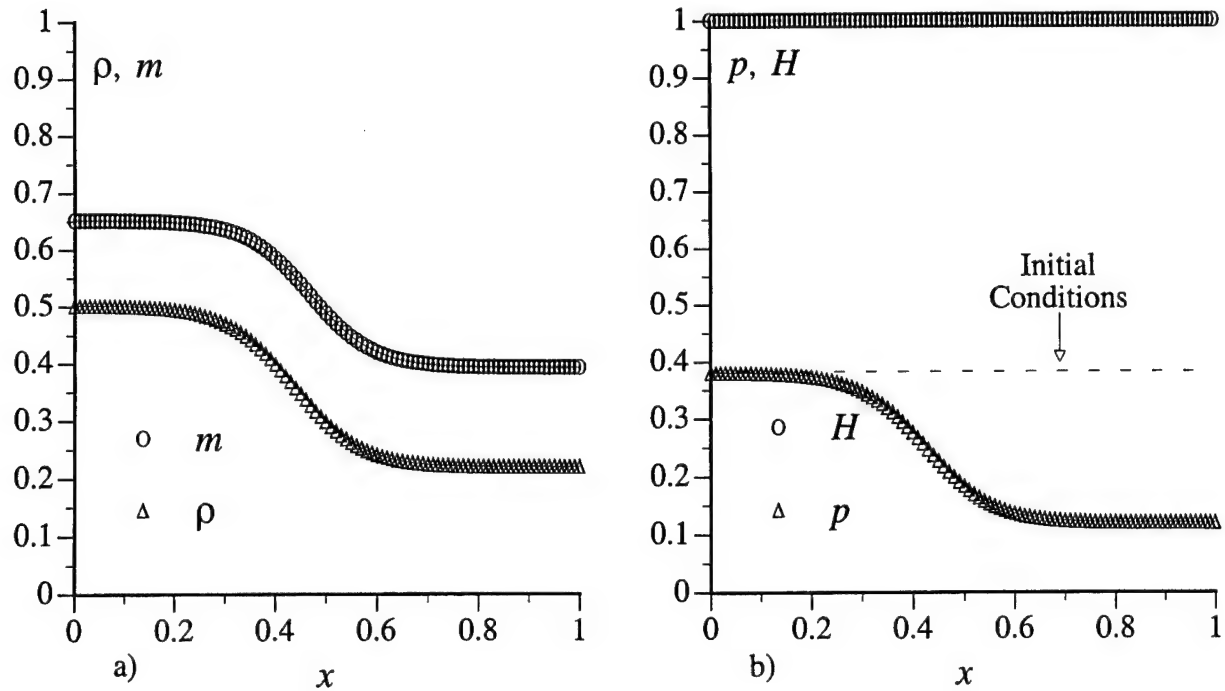


Figure 20: Isentropic Flow: a) Density and Momentum, b) Pressure and Enthalpy

Figure 21 b) presents the distribution of Mach number M , which also agrees with the exact solution, and the variations of acoustics and pressure-gradient upstream-bias functions α and δ .

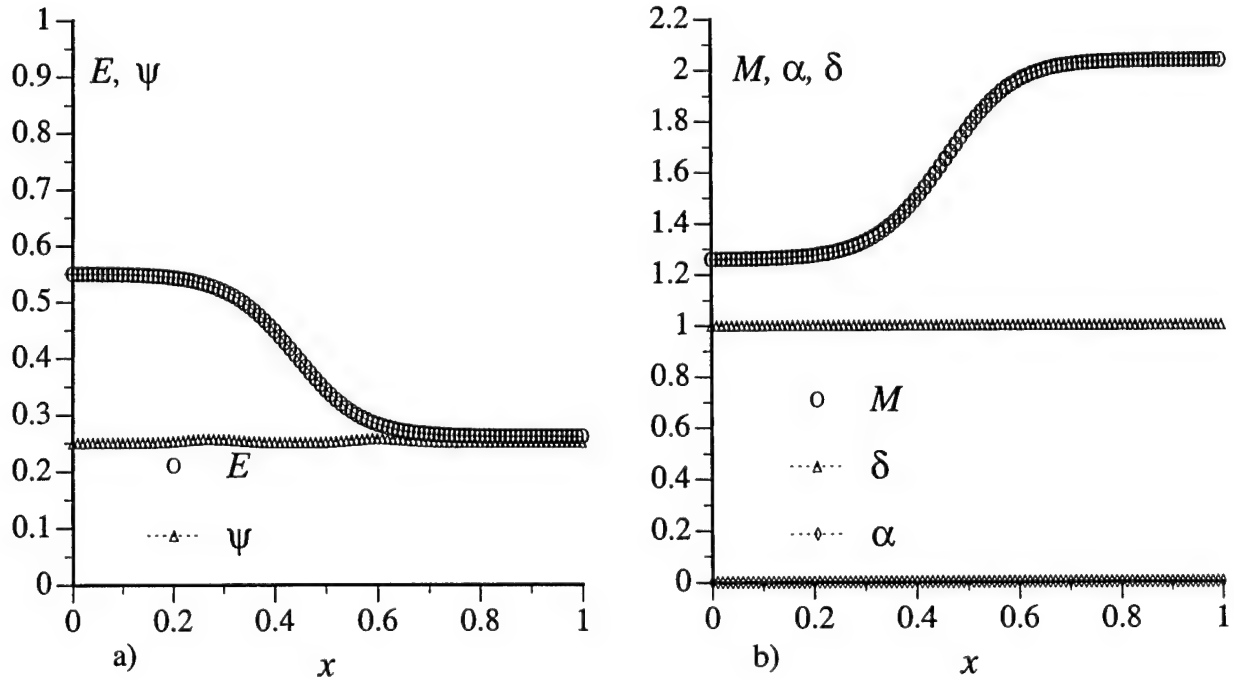


Figure 21: Isentropic Flow: a) Energy and Controller, b) Mach Number, α and δ

For a supersonic flow, $\alpha \equiv 0$ and $\delta \equiv 1$. No acoustics-matrix upstream-bias is thus present in this solution and the entire flux divergence receives a uniform upstream-bias approximation.

8.3.2 Flow with Embedded Normal Shock

A normal shock wave features in this steady flow as a result of the subsonic-outlet pressure boundary condition $p/p_{\text{tot,in}} = 0.746$, imposed as an impulsive step decrease from the initial conditions, for the entire flow evolution toward steady state. The theoretical solution places the normal shock at the area ratio $A_s/A_{*in} = 1.35016$, which corresponds to the interior of the finite element with node coordinates $x = 0.48$ and $x = 0.49$, within the computational domain. The exact shock Mach numbers are $M_{\text{sup}} = 1.71319$ and $M_{\text{sub}} = 0.63717$, which lead to the stagnation pressure and critical-area ratios $p_{\text{tot,out}}/p_{\text{tot,in}} = A_{*in}/A_{*out} = 0.85022$. The associated outlet area ratio and Mach number are $A_{\text{out}}/A_{*in} = 1.74514$, $M_{\text{out}} = 0.43629$.

Figures 22 a)-b) present the convergence rate and steady-state speed. The algorithm is certainly capable of driving the maximum residual down to machine zero, with a total residual reduction by 14 orders of magnitude, with $C_{\text{max}} = 12$; a residual reduction by 6 orders of magnitude occurs within about 250 time steps. Other initial conditions, closer to the steady state, would presumably lead to faster convergence. These results, however, compare favorably with those in Reference 13, which reports lack of convergence with Roe's algorithm for this benchmark and with a similar computational solution. This comparison rests on the observation that the acoustics-convection upstream resolution algorithm is not a purely flux-vector splitting algorithm, but it also uses, like Roe's algorithm, a Riemann solver, 'though applied to the acoustics equations. The calculated speed reflects the exact solution, indicated with a solid line, and clearly shows the expected rapid rise preceding the shock as well as an excellent calculated normal shock, captured over only one node.

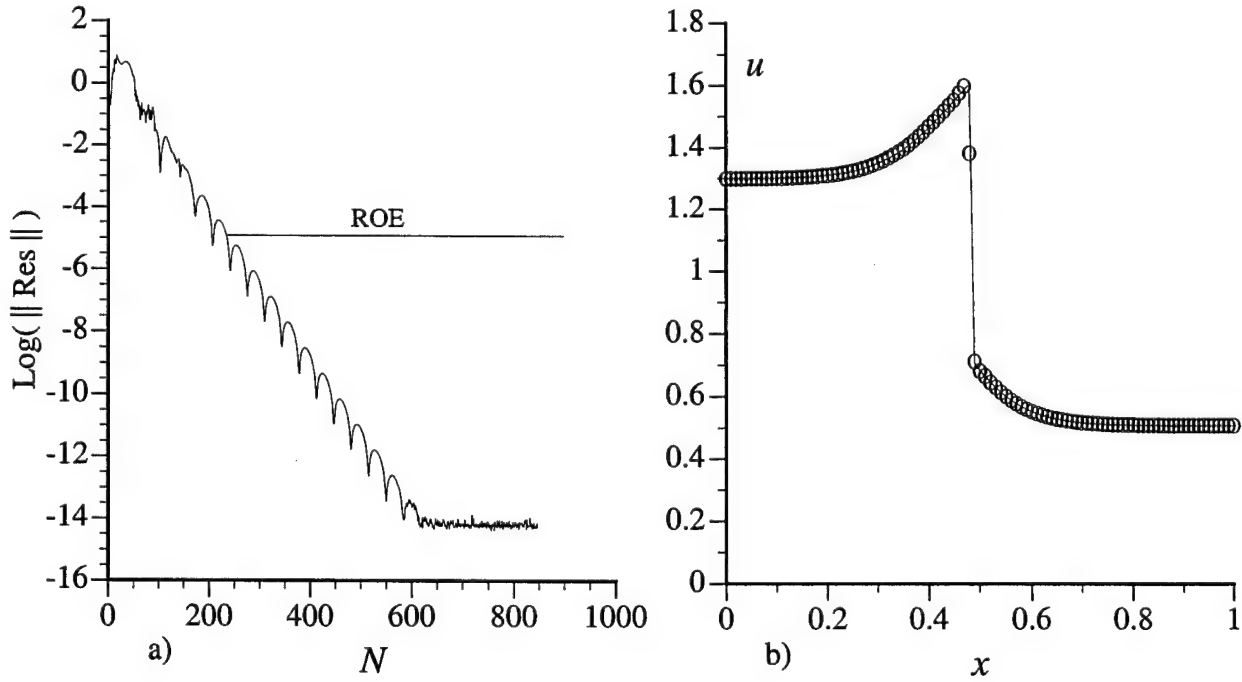


Figure 22: Shocked Flow: a) Convergence Rate, b) Speed

The distributions of static density and pressure in Figures 23 a)-b) also reflect the corresponding exact solutions, with rapid changes in these two variables clearly resolved and normal shock again sharply captured over one internal node. In harmony with the previous benchmark results, also for this problem has the algorithm correctly generated continuous distributions for both linear

momentum m and enthalpy H across the normal shock, without any shock bump. Furthermore, the computed H remains again constant, as has to be the case for a steady adiabatic flow.

Figure 24 a) presents the distributions of total energy E , which visually coincides with the

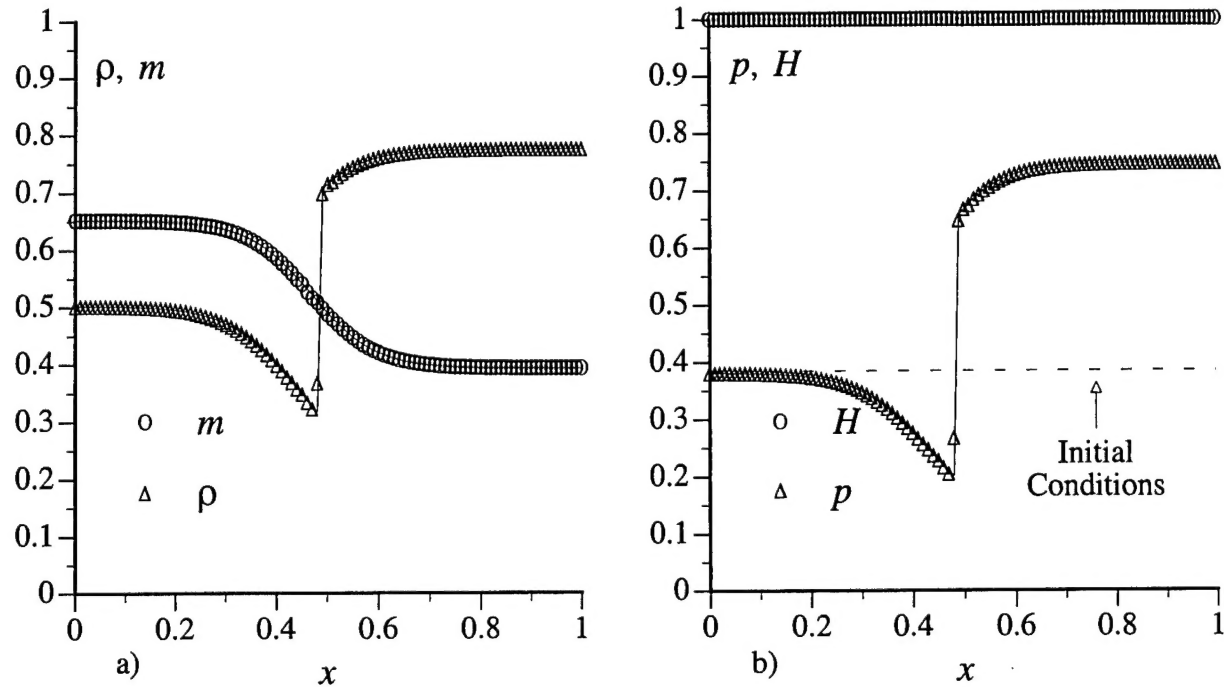


Figure 23: Shocked Flow: a) Density and Momentum, b) Pressure and Enthalpy

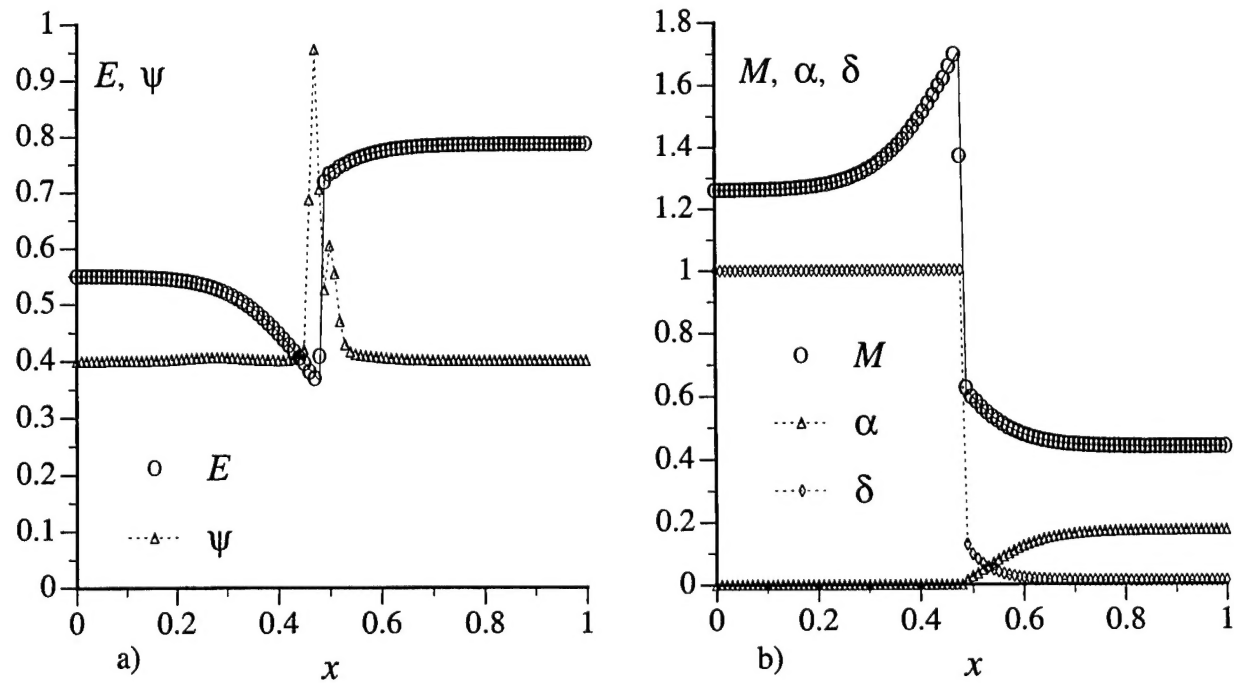


Figure 24: Shocked Flow: a) Energy and Controller, b) Mach Number, α and δ

exact solution in solid line, and upstream bias controller ψ , with $0.4 \leq \psi < 1.5$. The controller remains essentially constant over smooth solution regions, with $\psi = 0.4$, which corresponds to a 40% upstream bias. At the shock, ψ rapidly rises and reaches a $\psi \simeq 0.96$ extremum, which induces a 96% upstream-bias. This increase in ψ appears less sudden at its inception than that in Figure 17 a), which reinforces the conjecture that a relatively smooth increase of ψ at a normal shock can obviate modest shock overshoots. No overshoots are present in this solution, and as Figure 24 a) bears out the algorithm succeeds in focusing an increased level of upstream-bias, hence artificial dissipation, at the shock region only, precisely where required for an essentially sharp and non-oscillatory solution. Figure 24 b) presents the distribution of Mach number M , which also reflects the exact solution, and the corresponding distributions of the acoustics and pressure-gradient upstream-bias functions α and δ . According to these distributions, the acoustics upstream-bias is present only in the outlet subsonic regions of the flow. This type of upstream-bias vanishes in the supersonic region, including the normal shock, hence it plays no local role in the computation of the shock. Also in this case, therefore, is shock resolution entirely due to the convection and pressure-gradient upstream biases, which occur with the same weight at the supersonic side of the shock, where $\delta = 1$. As M falls across the shock, so does δ , which indicates that the upstream bias in the approximation of the pressure gradient quickly decreases, leading to an essentially centered approximation of this gradient towards the outlet. Also for all the distributions computed for this benchmark are the outlet variations smooth and undistorted; in particular the calculated outlet pressure coincides with the imposed pressure boundary conditions, which again reflects favorably on the surface-integral pressure enforcement strategy.

9 Concluding Remarks

The acoustics-convection upstream resolution algorithm rests on the physics and mathematics of acoustics and convection. It introduces a decomposition of the flux vector jacobian into acoustics and convection matrix components, for general equilibrium equations of state, and generates the upstream bias at the differential equation level before any discrete approximation. This formulation generates a characteristics-bias flux which generalizes in the continuum the traditional upwind-scheme numerical fluxes.

A natural finite element discretization of the characteristics-bias flux generates an essentially centered approximation of the Euler flux divergence, in the form of a non-linear combination of upstream diffusive and downstream anti-diffusive flux differences, with greater bias on the upstream diffusive flux difference. The algorithm induces this upstream bias and associated artificial diffusion mostly locally in regions of solution discontinuities, whereas it decreases the upstream-bias in regions of solution smoothness. This solution-driven variable upstream-bias thus minimizes artificial dissipation via an upstream-bias controller that depends on the jumps of solution slopes. The study in this paper has implemented the algorithm using a linear approximation of fluxes within two-noded cells, without any MUSCL-type local extrapolation of variables.

The computational results have validated accuracy and essential-monotonicity performance of the acoustics-convection upstream resolution algorithm for transient and steady smooth and shocked flows. The algorithm generates essentially non-oscillatory solutions and automatically preserves a constant enthalpy as well as smoothness of both enthalpy and mass flux across steady normal shocks. These results have also validated an intrinsically stable pressure boundary condition procedure at a subsonic outlet. This procedure directly enforces the outlet pressure within the surface integral that emerges in the momentum-equation weak statement. The computed solutions at nozzle outlets remain smooth and undistorted and mirror the exact reference solutions, which bears out the reliability of this pressure boundary condition.

According to the solution-driven numerical values of the upstream-bias controller, the computed smooth and shocked solutions resulted from a mostly centered discretization. This finding indicates that a uniformly fully upwind formulation is not strictly necessary within a characteristics-bias algorithm to generate essentially sharp and non-oscillatory solutions. The algorithm, therefore, succeeds in both reducing artificial dissipation in regions of smooth flow, for higher accuracy, and focusing an increased level of upstream-bias, hence artificial dissipation, at the shock regions only, precisely where required for stability and sharp shock capturing.

The computational results agree with the reference solutions, with curvature discontinuities exactly calculated and sharp normal shocks captured over one or two points. The finite element acoustics-convection upstream resolution algorithm, therefore, delivers solutions that are as sharp and non-oscillatory as those generated by local-extrapolation flux-vector and flux-difference splitting schemes¹³. This characteristics-bias algorithm, however, admits a straightforward implicit implementation, features a computational simplicity that parallels a traditional centered discretization, and rationally decreases superfluous artificial diffusion. Ongoing work is completing an intrinsically multi-dimensional and infinite-directional acoustics-convection algorithm, to be detailed in a future paper.

Acknowledgements

The research in this paper has been partly supported by the U.S. Army Research Office (ARO) under grant number DAAH04-96-1-0095. The author is especially grateful to Dr. Tom Doligalski, program manager, for this ARO support.

References

- [1] T. J. R. Hughes, "Recent Progress in the Development and Understanding of SUPG Methods with Special Reference to the Compressible Euler and Navier-Stokes Equations", *International Journal for Numerical Methods in Fluids*, 7, 11, (1987).
- [2] A. J. Baker and J. W. Kim, "A Taylor Weak Statement Algorithm for Hyperbolic Conservation Laws", *International Journal for Numerical Methods in Fluids*, 7, 489-520, (1987).
- [3] C. Hirsch, *Numerical Computation of Internal and External Flows*, Vol. 1, 2 John Wiley & Sons, New York, NY, (1991).
- [4] P.L. Roe, "Approximate Riemann Solvers, Parameter Vectors, and Difference Schemes", *Journal of Computational Physics*, 43, 357-372 (1981).
- [5] W. Coirier and B. van Leer, "Numerical Flux Formulas for the Euler and Navier-Stokes Equations: II. Progress in Flux-Vector Splitting", AIAA-91-1566, (1991).
- [6] M.-S. Liou and C.J. Steffen, "A New Flux Splitting Scheme", *Journal of Computational Physics*, 107, 23-29, (1993).
- [7] G. S. Iannelli, A. J. Baker, "An Intrinsically N-Dimensional Generalized Flux Vector Splitting Implicit Finite Element Euler Algorithm", AIAA 91-0123, 29th Aerospace Sciences Meeting, Reno, NV, (1991).
- [8] W. G. Vincenti and C. H. Kruger, Jr., *Introduction to Physical Gas Dynamics*, John Wiley and Sons, Inc., New York, London, Sydney, (1965).

- [9] G. S. Iannelli "A CFD Euler Solver from a Physical Acoustics-Convection Flux Divergence Decomposition", U.S. Army Technical Report, ARO DAAH04-96-1-0095, (1997).
- [10] R. A. Horn, C. R. Johnson, *Matrix Analysis*, Cambridge (1991).
- [11] R. Courant and D. Hilbert, *Methods of Mathematical Physics*, John Wiley & Sons, New York, NY, (1989).
- [12] K. Dekker and J.G. Verwer, *Stability of Runge-Kutta Methods for Stiff Non-Linear Differential Equations*, Elsevier Publishers, Amsterdam, (1984).
- [13] M-S Liou, B. van Leer "Choice of Implicit and Explicit Operators for The Upwind Differencing Method", AIAA 88-0624, 26th Aerospace Sciences Meeting, Reno, NV, (1988).